

**A three-dimensional *in vitro* tumor model representative of
the *in vivo* tumor microenvironment**

Christopher S. Szot

Dissertation submitted to the faculty of the Virginia Polytechnic Institute and
State University in partial fulfillment of the requirements for the degree of

Doctor of Philosophy
In
Biomedical Engineering

Marissa Nichole Rylander, Co-Chair
Joseph W. Freeman, Co-Chair
Yong Woo Lee
Padmavathy Rajagopalan
John L. Robertson

December 4, 2012
Blacksburg, VA

Keywords: tissue engineering, co-culture, collagen I hydrogel, cancer, angiogenesis

Copyright © 2012 Christopher S. Szot

A three-dimensional *in vitro* tumor model representative of the *in vivo* tumor microenvironment

Christopher S. Szot

Abstract

The inability to accurately reproduce the complexities of the *in vivo* tumor microenvironment with reductionist-based two-dimensional *in vitro* cell culture models has been a notable deterrent in identifying therapeutic agents that reliably translate to *in vivo* animal and human clinical trials. In an effort to address this, a growing number of three-dimensional (3D) *in vitro* tumor models capable of mimicking specific tumorigenic processes have emerged within the last decade. This concept stems from the understanding that cells cultured within 3D *in vitro* matrices have the ability to acquire phenotypes representative of the *in vivo* microenvironment. The objective of this project was to apply a tissue engineering approach towards developing a 3D *in vitro* tumor angiogenesis model. Initially, different scaffolds were investigated for supporting 3D tumor growth, including bacterial cellulose, electrospun polycaprolactone/collagen I, and highly porous electrospun poly(L-lactic acid). However, cancer cells cultured on these scaffolds demonstrated poor adhesion, sufficient adhesion with poor infiltration, and increased but still inadequate infiltration, respectively. Collagen I hydrogels were chosen as an appropriate scaffold for facilitating 3D *in vitro* tumor growth for two reasons – cell-mediated degradation and immediate 3D cell growth. It was hypothesized that cancer cells cultured within collagen I hydrogels could be encouraged to recapitulate key characteristics of *in vivo* tumor progression. MDA-MB-231 human breast cancer cells were shown to experience hypoxia and undergo necrosis in response to limitations in oxygen diffusion and competition for nutrients. Upregulation of hypoxia-inducible factor-1 α resulted in a significant increase in vascular endothelial growth factor gene expression. To capitalize on this endogenous angiogenic potential, microvascular endothelial cells were cultured on the surface of the designated “bioengineered tumors.” It was hypothesized that paracrine signaling between tumor and endothelial cells co-cultured within this system would be sufficient for inducing an angiogenic

response in the absence of exogenous pro-angiogenic growth factors. Endothelial cells in the co-culture group were shown to invasively sprout into the underlying collagen matrix, forming a capillary-like tubule network. This project culminated with the establishment of an improved *in vitro* tumor model that can be used as a tool for accurate evaluation and refinement of cancer therapies.

Acknowledgements

Graduate school has been a special period in my life where I have been challenged to become an independent researcher, gaining some knowledge and skills but mostly an appreciation and respect for the amount of time and effort required to accomplish research goals (especially those that initially seem simple and straightforward). None of this would have been possible without the opportunity I was given by my advisers Dr. Rylander and Dr. Freeman. When I first learned about this project during recruitment weekend I was immediately drawn to it and remember thinking that if I did not get an offer to come to Virginia Tech, I might not go to graduate school at all. Dr. Rylander and Dr. Freeman, thank you for believing in me, providing guidance, and allowing me to take ownership of this project.

I would like to thank Dr. Bob, Dr. Lee, and Dr. Rajagopalan for being members of my dissertation committee and for providing assistance when needed throughout this process. I would also like to thank the SBES staff of Tess, Pam, Kathy, and Jo, who are always cheerful, nice to talk to, and have been exceedingly helpful and patient with many administrative and purchasing issues.

I am very grateful to all of my fellow lab mates, past and present, who have provided an amazing work environment that has been a joy to come to everyday and will be wholly missed. In particular, Bryce, Samuel, and Eunna, your experience and advice have helped guide me through difficult experiments as well as simple lab problems. And Cara, this project would not have been possible without all of the struggles we had to endure and overcome together. Although it was unconventional to start graduate school working on the same project with someone else, I think we made it work well and are both better researchers because we had each other to rely on.

Graduate school would not have been as exciting and memorable if it wasn't for the great experiences I have had and the life-long friendships I have gained. From tailgating, to ski trips, to conferences, graduate school was full of fun times to help balance out all of the hard work. Of course, none of this would have been possible without my friends, especially Arena, Brad, Cara, Kate, Mike, Paulo, and Ashby.

Finally, I would like to thank my parents and sister for their love and support throughout my life.

Attribution

Chapter 2: Investigation of cancer cell behavior on nanofibrous scaffolds

Chapter 2 was published in Materials Science and Engineering C.

- Cara F. Buchanan, BS (Biomedical Engineering) is currently a PhD candidate at Virginia Tech. Ms. Buchanan was a co-author on this paper, contributed equally to data collection, and contributed editorial comments.
- Paul Gatenholm, PhD (Chemical and Biological Engineering) is currently a professor at Chalmers University of Technology and an adjuvant professor at Virginia Tech. Dr. Gatenholm was a co-author on this paper, provided bacterial cellulose for conducting experiments, and contributed editorial comments.
- Marissa Nichole Rylander, PhD (Biomedical Engineering) is currently an associate professor at Virginia Tech. Dr. Rylander was a co-author on this paper and contributed editorial comments.
- Joseph W. Freeman, PhD (Biomedical Engineering) is currently an associate professor at Rutgers University. Dr. Freeman was a co-author on this paper and contributed editorial comments.

Chapter 3: 3D *in vitro* bioengineered tumors based on collagen I hydrogels

Chapter 3 was published in Biomaterials.

- Cara F. Buchanan, BS (Biomedical Engineering) is currently a PhD candidate at Virginia Tech. Ms. Buchanan was a co-author on this paper, provided thoughtful discussion, and contributed editorial comments.
- Joseph W. Freeman, PhD (Biomedical Engineering) is currently an associate professor at Rutgers University. Dr. Freeman was a co-author on this paper and contributed editorial comments.
- Marissa Nichole Rylander, PhD (Biomedical Engineering) is currently an associate professor at Virginia Tech. Dr. Rylander was a co-author on this paper, principal

investigator for one of the grants supporting the research, and contributed editorial comments.

Chapter 4: *In vitro* angiogenesis induced by tumor-endothelial cell co-culture in bilayered, collagen I hydrogel bioengineered tumors

Chapter 4 was submitted to Tissue Engineering Part C.

- Cara F. Buchanan, BS (Biomedical Engineering) is currently a PhD candidate at Virginia Tech. Ms. Buchanan was a co-author on this paper, provided thoughtful discussion, and contributed editorial comments.
- Joseph W. Freeman, PhD (Biomedical Engineering) is currently an associate professor at Rutgers University. Dr. Freeman was a co-author on this paper and contributed editorial comments.
- Marissa Nichole Rylander, PhD (Biomedical Engineering) is currently an associate professor at Virginia Tech. Dr. Rylander was a co-author on this paper, principal investigator for both of the grants supporting the research, and contributed editorial comments.

Appendix B: A Three-Dimensional In Vitro Tumor Platform for Modeling Therapeutic Irreversible Electroporation

Appendix B was published in Biophysical Journal.

- Christopher B. Arena, BS (Biomedical Engineering) is currently a PhD candidate at Virginia Tech. Mr. Arena was a co-first author on this paper and contributed equally to data collection and writing.
- Paulo A. Garcia, PhD (Biomedical Engineering) is currently a post doctorate at Virginia Tech. Dr. Garcia was a co-author on this paper and contributed towards data collection, computational modeling, and editing.
- Marissa Nichole Rylander, PhD (Biomedical Engineering) is currently an associate professor at Virginia Tech. Dr. Rylander was a co-author on this paper, principal

investigator for one of the grants supporting the research, and contributed editorial comments.

- Rafael V. Davalos, PhD (Biomedical Engineering) is currently an associate professor at Virginia Tech. Dr. Davalos was a co-author on this paper, principal investigator for one of the grants supporting the research, and contributed editorial comments.

Table of Contents

Abstract.....	ii
Acknowledgements.....	iv
Attribution.....	v
Table of Contents.....	viii
List of Figures.....	xiii
List of Tables.....	xvii
List of Abbreviations.....	xix

Chapter 1: Introduction

1.1 Background.....	1
1.1.1 Clinical significance.....	1
1.1.2 Fundamental characteristics of the tumor microenvironment.....	3
1.1.2.1 Oxygen heterogeneity.....	3
1.1.2.2 Unregulated stroma.....	5
1.1.2.3 Aberrant microvasculature.....	7
1.1.3 Advantages of three-dimensional cell culture systems.....	8
1.2 Literature review.....	10
1.3 Objective.....	12
1.4 Specific aims.....	13

Chapter 2: Investigation of cancer cell behavior on nanofibrous scaffolds

Abstract.....	16
1. Introduction.....	16
2. Materials and methods.....	17
2.1 Bacterial cellulose.....	17
2.2 Electrospun scaffold preparation.....	17
2.3 Cell culture.....	17
2.4 Cell proliferation and cytotoxicity assessment.....	18
2.5 Electron microscopy.....	18
2.6 Confocal microscopy.....	18

2.7 Statistical analysis	18
3. Results and discussion	18
3.1 Cell viability and proliferation	18
3.2 Cell adhesion	20
3.3 Cell infiltration	20
3.4 Cell morphology	20
4. Conclusions	21
Acknowledgements	21
References	21

Chapter 3: 3D *in vitro* bioengineered tumors based on collagen I hydrogels

Abstract	22
1. Introduction	22
2. Materials and methods	25
2.1 Cell culture	25
2.2 Collagen I hydrogels	25
2.3 Immunofluorescence staining	25
2.3.1 3D morphological analysis	25
2.3.2 Cell proliferation and necrosis	25
2.3.3 Hypoxia	25
2.4 Gene expression analysis	25
2.5 Statistical analysis	26
3. Results	26
3.1 Cell morphology in 3D collagen I hydrogels	26
3.2 Cell proliferation and the progression towards cell death	26
3.3 Growing levels of hypoxia in the bioengineered tumors	27
3.4 Bioengineered tumor hypoxic and angiogenic gene expression profile	27
3.5 2D versus 3D cell culture: comparison of hypoxic and angiogenic gene expression	28
4. Discussion	28
5. Conclusion	29
Acknowledgements	29

References	29
Chapter 4: <i>In vitro</i> angiogenesis induced by tumor-endothelial cell co-culture in bilayered, collagen I hydrogel bioengineered tumors	
4.1 Abstract	30
4.2 Introduction	31
4.3 Materials and methods	33
4.3.1 Cell culture	33
4.3.2 Bilayered, collagen I hydrogel bioengineered tumors	33
4.3.3 Angiogenic growth factor expression	35
4.3.4 Analysis of angiogenic activity	36
4.3.4.1 Quantification of endothelial cell proliferation	36
4.3.4.2 Analysis of morphological changes	37
4.3.4.3 Characterization of angiogenic sprouting	37
4.3.5 Statistical analysis	37
4.4 Results	38
4.4.1 VEGF expression from the bioengineered tumors	38
4.4.2 Tumor-endothelial cell co-culture regulates endothelial cell proliferation	40
4.4.3 Tumor-endothelial cell co-culture elicits an elongated endothelial cell morphology	41
4.4.4 Tumor-endothelial cell co-culture induces invasive angiogenic sprouting	44
4.4.5 Acellular collagen matrix concentration governs angiogenic sprouting	45
4.4.6 Angiogenic growth factor composition and concentration influence angiogenic sprouting	47
4.4.7 Duration of co-culture determines induction but not extent of angiogenic sprouting	49
4.5 Discussion	50
4.6 Conclusion	54
4.7 Acknowledgements	54
4.8 References	55
Chapter 5: Future Work and Conclusions	
5.1 Immediate objective	59

5.1.1 Quantification of angiogenic sprouting.....	59
5.1.2 Fibroblast co-culture.....	61
5.1.2.1 Preliminary results.....	62
5.1.3 Screening of angiogenesis inhibitors.....	65
5.2 Long term objective.....	68
5.3 Conclusions.....	69
References.....	70
Appendix A: Highly porous PLLA electrospun scaffolds for increased cell infiltration	
A.1 Introduction.....	81
A.2 Materials and methods.....	81
A.2.1 Dual electrospun PLLA/PEO scaffolds.....	81
A.2.2 Scanning electron microscopy.....	82
A.2.3 Cell infiltration.....	83
A.2.4 Gene expression analysis.....	83
A.2.5 Statistical analysis.....	84
A.3 Results and discussion.....	84
A.4 Conclusion.....	86
A.5 Acknowledgements.....	86
A.6 References.....	86
Appendix B: A Three-Dimensional In Vitro Tumor Platform for Modeling Therapeutic Irreversible Electroporation	
Abstract.....	88
Introduction.....	88
Materials and methods.....	89
Cell culture.....	89
Collagen I hydrogel <i>in vitro</i> tumors.....	89
IRE pulse delivery for <i>in vitro</i> tumors.....	89
Viability analysis for <i>in vitro</i> tumors.....	90
Analysis of IRE on cell suspensions.....	90
Numerical modeling.....	90

Description of the model geometry and mesh	90
Determination of baseline electrical properties	90
Determination of transient current and temperature development	91
Determination of electric field threshold for cell death	91
Results	91
Physiological response to IRE pulse delivery within <i>in vitro</i> tumors	91
Determination of baseline electrical properties	92
Numerical model validation	93
Determination of transient current and temperature development	93
Determination of electric-field threshold for cell death of <i>in vitro</i> tumors	94
Determination of electric-field threshold for cell death in suspension	94
Discussion	95
Conclusion	96
References	96
Supplementary Materials	98

List of Figures

Chapter 1

Figure 1.1: The characteristics of a hypoxic tumor mass.....	4
Figure 1.2: Tumor-stroma interactions during mammary ductal carcinoma progression.....	5
Figure 1.3: Schematic comparison of normal tissue and solid tumor vasculature.....	7

Chapter 2

Figure 1: FESEM was used to show the scaffold morphology of (a) bacterial cellulose and (b) electrospun PCL/collagen I.....	17
Figure 2: An alamarBlue® cell viability reagent was used to analyze cell viability and proliferation over a 7 day period.....	18
Figure 3: Cell adhesion was characterized using FESEM.....	19
Figure 4: Cell infiltration was analyzed using FESEM.....	20
Figure 5: Cell morphology was analyzed using Oregon Green® 488 phalloidin, a high-affinity probe for F-actin, and DAPI to visualize nuclei.....	21

Chapter 3

Figure 1: (a) The pre-vascularized stages of <i>in vivo</i> solid tumor development can be characterized by identifiable criteria within the tumor microenvironment, including an uninhibited 3D proliferative capacity, regions of hypoxia surrounding a necrotic core, and activation of angiogenic growth factors, including VEGF-A. (b) Collagen I hydrogels cultured with MDA-MB-231 human breast cancer cells were bioengineered as a platform for <i>in vitro</i> solid tumor development.....	23
Figure 2: MDA-MB-231 cells were cultured in collagen I hydrogels for 1, 3, 5, and 7 days (a-d, respectively), exhibiting the typical cell-matrix and cell-cell interactions observed <i>in vivo</i>	24
Figure 3: (a) MDA-MB-231 cells were seeded at a density of 1 million cells/ml, and on day 1, the cells were evenly distributed throughout the entire hydrogel. (b) Noticeable proliferation was observed on day 5, with cell proliferation leading to the formation of cell clusters. (c) The initial cell seeding density was increased to 4 million cells/ml, and on day 1, the viable cells (green) were evenly distributed with only a few dead cells (red) present at non-specific degrees of depth.	

(d) On day 5, cells were viable through ~150-200 μm of depth below the surface, with limitations in oxygen and nutrients leading to cell death towards the core of the bioengineered tumors	24
Figure 4: Hypoxia was detected using immunofluorescence for HIF-1 α	25
Figure 5: Quantitative RT-PCR was used to analyze the progression of HIF-1 α and VEGF-A gene expression in the bioengineered tumors over a 7-day period, with expression on day 0 used as the control.....	26
Figure 6: HIF-1 α and VEGF-A gene expression were significantly upregulated when MDA-MB-231 cells were cultured in 3D collagen I hydrogels as compared to cells cultured in a monolayer on 2D tissue culture polystyrene.....	27

Chapter 4

Figure 4.1: Schematic illustration of the bilayered bioengineered tumor model cultured in a transwell insert.....	34
Figure 4.S1: TIME-mKate cells after 7 days of co-culture on MDA-MB-231 bioengineered tumors (a) when cultured in direct contact with the cancer cell-seeded surface and (b) when cultured on the acellular collagen hydrogel layered on top of the bioengineered tumors.....	35
Figure 4.S2: Tumor cell proliferation and cell-matrix interactions within the bioengineered tumors.....	38
Figure 4.2: VEGF protein secretion from bioengineered tumors seeded with MDA-MB-231 or MCF7 cells.....	39
Figure 4.S3: Immunofluorescence staining for intracellular VEGF expression.....	40
Figure 4.S4: TIME cells stained with DAPI cultured on the surface of the bioengineered tumors.....	41
Figure 4.3: TIME cell proliferation when cultured on the surface of the bioengineered tumors.....	42
Figure 4.4: TIME cell morphology when cultured on the surface of the bioengineered tumors.....	43
Figure 4.S5: TIME cells cultured on the MCF7 bioengineered tumors reached confluence on day 7 when supplemented with complete endothelial growth medium.....	43
Figure 4.5: Angiogenic sprouting of TIME cells cultured on MDA-MB-231 bioengineered tumors in the absence of exogenous VEGF and bFGF.....	44
Figure 4.6: Angiogenic sprouting of TIME cells in the control group.....	45

Figure 4.7: Influence of matrix concentration and supplemented bFGF on angiogenic sprouting of TIME cells cultured for 7 days on MDA-MB-231 bioengineered tumors.....	46
Figure 4.S6: (a) VEGF protein secretion from bioengineered tumors cultured with MDA-MB-231 cells at a density of 1×10^6 cells/ml. TIME cells cultured on the 1×10^6 cells/ml MDA-MB-231 bioengineered tumors (b) proliferated, (c) developed elongated and aligned morphologies (day 7), and (d) formed capillary-like tubules (day 7; 2 mg/ml acellular collagen) similar to when cultured on the 5×10^6 MDA-MB-231 bioengineered tumors.....	48
Figure 4.8: Influence of (a) TIME cell seeding density and (b) duration in co-culture on angiogenic sprouting.....	49

Chapter 5

Figure 5.1: Angiogenic sprouting beneath the surface endothelial monolayer when co-cultured on the MDA-MB-231 bioengineered tumors.....	59
Figure 5.2: a) Glass coverslip used to create a flat surface on the collagen hydrogel during polymerization. b) Collagen hydrogel within the transwell insert with a completely flat surface.....	60
Figure 5.3: Live/Dead stain on day 7 of NHDFs cultured within a collagen hydrogel a) without and b) with prior mitomycin-C treatment.....	62
Figure 5.4: The NHDF collagen hydrogels after 1 day of co-culture with TIME cells from the a) side and b) top view.....	63
Figure 5.5: The tumor-fibroblast-endothelial cell hydrogels after 7 days of co-culture gave no indication of volume reduction.....	64

Appendix A

Figure A.1: Schematic drawing of the PLLA/PEO dual electrospinning set up.....	82
Figure A.2: a) 12% (w/v) PLLA was electrospun alone and b) dual electrospun with 10% (w/v) PEO. c) The PEO fibers were leached out through aqueous dissolution, leaving large voids for cell infiltration.....	84
Figure A.3: Cross-section of a highly porous PLLA electrospun scaffold following 21 days of culture with the MDA-MB-231 cells.....	85

Figure A.4: Quantitative RT-PCR for determining intra-cellular levels of hypoxia and VEGF expression following cell infiltration within the highly porous PLLA electrospun scaffolds 85

Appendix B

Figure 1: (a) Experimental setup for IRE pulse delivery in collagen I hydrogel-based <i>in vitro</i> tumors, in which PDAC cells are embedded. (b) Geometry and mesh used in the finite element model for simulating the electrical and thermal response of the <i>in vitro</i> tumors to IRE.....	90
Figure 2: A Live/Dead assay for assessment of cell death following IRE pulse delivery of (a) 30 V, (b) 150 V, (c) 300 V, and (d) 450 V	92
Figure 3: (a) A sharp interface between live (green; left) and dead (red; right) cells at the threshold boundary for cell death with sub-millimeter resolution. (b) 3D reconstruction at this interface highlights the transition zone between live and dead cells and demonstrates that IRE-induced cell death was uniform throughout the <i>in vitro</i> tumors.....	92
Figure 4: (a-c) An H&E stain for further assessment of cell viability following IRE pulse delivery of 450V through <i>in vitro</i> tumors seeded with 50×10^6 cells/ml. An F-actin stain (red) was used to determine the effect of IRE-pulse delivery on the cytoskeleton of PPT-8182 cells cultured within the (d) IRE-treated and (e) un-treated regions of the <i>in vitro</i> tumors.....	93
Figure 5: Change in (a) current and (b) temperature delivered through the <i>in vitro</i> tumors during IRE performed at 150 V, 300 V, 450 V, and 600 V	93
Figure 6: Surface plots from the numerical model showing the (a) electric field distribution, (b) temperature distribution, and (c) conductivity distribution at the end of an 80 s IRE treatment at 300 V	94
Figure 7: Overlay of electric field contours predicted by the numerical model at the end of an 80 s IRE treatment at (a) 300 V and (b) 450 V with the corresponding live/dead tiled images from Fig 2.....	94
Figure S1: Percent viability (normalized to the sham group) following IRE of PPT-8182 cells in suspension at electric fields ranging from 0 V/cm to 1500 V/cm.....	98

List of Tables

Chapter 1

Table 1.1: Recent 3D <i>in vitro</i> tumor models	11
---	----

Chapter 2

Table 1: Scaffold characterization: fiber diameter	18
--	----

Appendix B

Table 1: Physical properties used in the numerical simulations	90
--	----

Table 2: Baseline electrical conductivity from prepulse measurements and EMT theory	91
---	----

Table 3: Treatment dimensions and electric field threshold for cell death	92
---	----

List of Abbreviations

2D	two-dimensional
3D	three-dimensional
ANG	angiopoietin
BC	bacterial cellulose
bFGF	basic fibroblast growth factor
CAF	cancer associated fibroblast
ECM	extracellular matrix
ELISA	enzyme-linked immunosorbent assay
EMT	effective medium theory
FBS	fetal bovine serum
FESEM	field emission scanning electron microscopy
H&E	hemotoxylin and eosin
HIF-1 α	hypoxia-inducible factors-1 α
IL-8	interleukin-8
IRE	irreversible electroporation
MCTS	multicellular tumor spheroid
MMP	matrix metalloproteinase
NHDF	normal human dermal fibroblast
PA	plasminogen activator
PBS	phosphate buffered saline
PCL	polycaprolactone
PDAC	pancreatic ductal adenocarcinoma
PDGF	platelet-derived growth factor
PEO	polyethylene oxide
PI	propidium iodide
PLLA	poly(L-lactic acid)
PPT	primary pancreatic tumor
qRT-PCR	quantitative reverse transcription polymerase chain reaction
RGD	Arg-Gly-Asp

SMA	smooth muscle actin
TIME	telomerase-immortalized human microvascular endothelial cells
TKI	tyrosine kinase inhibitor
VEGF	vascular endothelial growth factor

Chapter 1: Introduction

1.1 Background

1.1.1 Clinical significance

Cancer is a pervasive malady that encompasses a diverse group of over 100 diseases defined by the acquired capacity of abnormal cells to divide without control and invade distant organs throughout the body using the cardiovascular and lymphatic systems [3]. While microscopic neoplasms, i.e. tumors, can accumulate in many tissues and organs over a lifetime [5], most of these tumors linger in a dormant state and remain harmless to the host [6]. Whether a tumor escapes dormancy is dependent on the overall balance of angiogenic promoters and inhibitors within the evolving tumor microenvironment [7, 8]. Although successful remission has been achieved when cancer is diagnosed and treated during its early stages of development, a tumor that has established neovascularization and metastasized poses a significantly greater risk of mortality [9]. The National Cancer Institute estimated that there were more than 1.6 million new incidences of cancer and approximately 577,000 deaths from cancer in the United States in 2012 [10]. Current therapeutic approaches, many which were conceived over a half century ago, include surgery [11], chemotherapy [12], radiation therapy [13], hormone therapy [14], hyperthermia [15], immunotherapy [16], gene therapy [17], and angiogenesis inhibitors [18]. The main issue with these treatments is the persistence of recurrent tumors, which can occur through insufficient primary treatment, a developed resistance to therapy, or activation of dormant metastases. Other problems include non-specific targeting, damage to vital organs, aggravation of existing conditions, and infertility [10].

Over \$200 billion has been invested in cancer therapy research and development since President Nixon signed the National Cancer Act of 1971, which was perceived as the start of the “war on cancer” [19]. Unfortunately, a significant amount of this time and money has been spent on failed drug development, as 59% of the already limited number of anti-cancer agents that make it to Phase III clinical trials undergo attrition [20]. Overall, only 5% of new cancer drugs entering clinical trials are successful in obtaining FDA or European approval [20]. In a 2004 article published in FORTUNE magazine titled “Why We’re Losing the War on Cancer,” several high-profile cancer researchers from academia and industry discussed one of the central

limitations impeding the development of definitive cancer termination and prevention treatments – an over reliance on inadequate preclinical models, specifically *in vivo* mouse models [19]. While most of these researchers incorporate mouse models into their research, they understand that there are many basic physiological differences between humans and mice that can lead to inaccurate results and false hope. One example is that mice metabolize and react to drugs differently than humans [21-23]; specifically, certain drugs have been shown to fail in clinical trials because of liver toxicity that was not detectable in the *in vivo* model [24]. There are also considerable anatomical, cellular, and genetic differences between humans and mice, including telomerase regulation and incompatible cytokine signaling [21, 25, 26]. For example, mice do not produce interleukin (IL)-8 [27], which is an important pro-angiogenic factor expressed within the tumor microenvironment [28]. Furthermore, all *in vivo* cancer models, including mice, rats, hamsters, rabbits, opossums, and zebrafish, are intrinsically complex with unpredictable parameters, including host cells, an immune response, hemodynamics, and endogenous growth factors [29]. While this complexity is representative of the human body, these variables can complicate isolating the impact of specific stimuli, such as cellular, chemical, and mechanical cues, during therapeutic testing, which can lead to inaccurate drug evaluation. Regardless of these shortcomings, animal models still provide the closest representation of the complete *in vivo* human tumor microenvironment.

An emerging interface between cancer research and tissue engineering has compelled many researchers to reevaluate the potential of developing complex *in vitro* cell culture models for conducting basic cancer research in place of or prior to *in vivo* animal models. This notion stems from both the limitations of *in vivo* animal models, as discussed above, and the recognition that cells cultured in a three-dimensional (3D) *in vitro* environment have the ability to develop phenotypes and respond to stimuli similar to *in vivo* biological systems [30, 31]. While the advantages of 3D cell culture over two-dimensional (2D) cell culture have been reported in the literature for several decades [32], the concept of constructing 3D *in vitro* tumor models has recently garnered considerable attention, highlighted by several prominent review articles [26, 31, 33]. This hybrid field, referred to as tumor engineering, has attracted researchers from many diverse disciplines and is defined as the development of complex 3D *in vitro* tumor models that reproduce the phenotypes and physiological responses of the *in vivo* tumor microenvironment [34]. Although it is unlikely that these systems will reach a level of complexity that will allow

them to completely replace *in vivo* models, they can serve as powerful tools for the accurate evaluation and refinement of therapies before investing significant time and money in conducting *in vivo* animal trials.

1.1.2 Fundamental characteristics of the tumor microenvironment

Tumorigenesis is a consequence of multiple genetic mutations, typically acquired over a lifetime, which lead to the over expression of oncogenes and the down regulation of tumor-suppressor genes. These transformed cells exhibit developed traits distinct to cancer cells, including self-sufficiency in the absence of growth factors, insensitivity to growth-inhibitory signals, limitless replicative potential, and evasion of apoptosis despite severe DNA damage [3]. Due to these genetic changes, tumor cells have the ability to proliferate and differentiate into complex heterogeneous masses identifiable through specific fundamental characteristics, including severely low oxygen levels, regions of necrosis, increased stromal stiffness, extracellular matrix (ECM) buildup, increased interstitial pressure, and a malformed vasculature.

1.1.2.1 Oxygen heterogeneity

Initial tumor growth occurs in the absence of neovascularization, i.e. angiogenesis, leading to an avascular environment that has insufficient oxygen and nutrients for sustaining limitless growth [1, 6]. Under these restrictions, tumor cells only have the ability to proliferate into microscopic masses no larger than 1-2 mm³ in size. This state of limited oxygen availability, known as hypoxia, is a consequence of consumption outweighing supply [1, 35]. Chronic hypoxia develops in tumors as a result of diffusion limitations through the growing mass of tumor and stromal cells, with hypoxia observed at distances of 100-200 μm from the nearest blood vessel [1, 35, 36]. In general, oxygen distribution throughout tumors is vastly heterogeneous with many areas of exceedingly low oxygen levels ($pO_2 \leq 5$ mmHg) [35, 37].

The role of hypoxia in tumor development is characterized as a “Janus face,” encouraging both pro-death and pro-survival mechanisms. Cells that have been deprived of oxygen and nutrients demonstrate a reduction in total protein synthesis, resulting in decreased proliferation and eventual cell death through either apoptosis or necrosis [35, 36, 38]. Apoptosis occurs following hypoxia-induced upregulation of the pro-apoptotic transcription factor p53 [35, 38]. Sustained levels of severe hypoxia, which are often accompanied by significant glucose

deficiencies, leads to necrosis. Histological analysis of excised tumors has demonstrated that regions of necrotic cells are present at the center of growing tumor masses surrounded by hypoxic cells (Fig. 1.1) [1]. Select tumor cells are able to acclimate to this oxygen and nutrient deprived environment through upregulating the expression of glucose transporters and glucose metabolizing enzymes, which act to increase anaerobic glycolysis [38]. These cells typically undergo proteome and genome alterations that result in a more aggressive phenotype, leading to limitless proliferation, invasiveness, and metastasis [39, 40]. Specifically, hypoxia-inducible factor (HIF)-1 α , a transcription factor that is only stable under hypoxic oxygen levels, acts directly upon a specific set of genes which control cell survival and cell death, metabolism, pH regulation, cell adhesion and migration, ECM remodeling, angiogenesis, and metastasis [1].

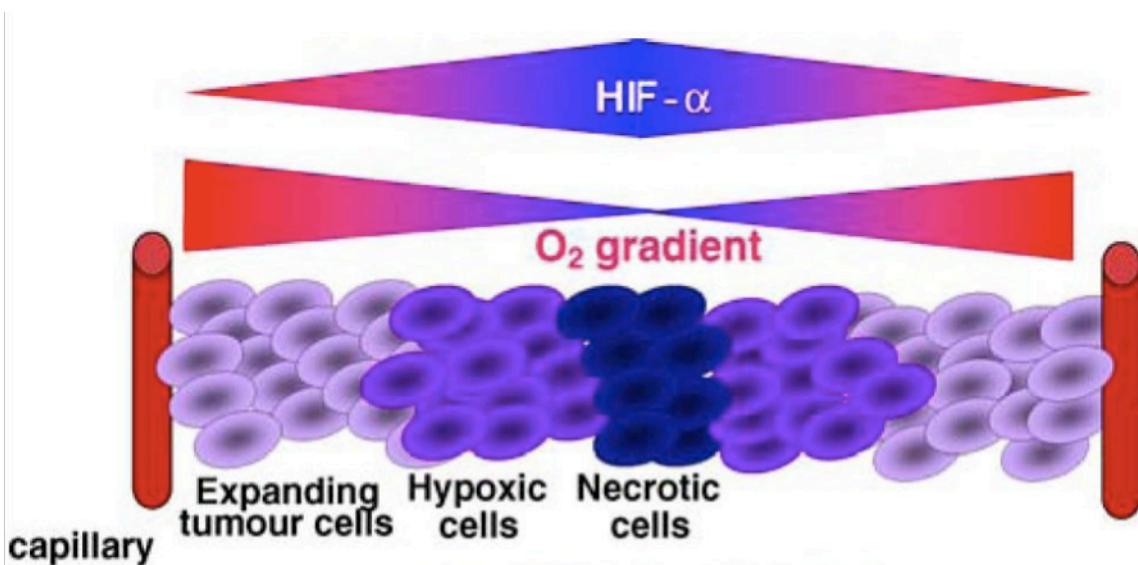


Figure 1.1. The characteristics of a hypoxic tumor mass. Blood capillaries carry oxygen to tissues, but since oxygen has a diffusion limit, its concentration decreases as the distance from capillaries increases. Macroscopic examination of solid tumors reveals the presence of expanding tumor cells in proximity to capillaries and a central region of necrotic cells. This gradient of cell viability parallels that of a decreasing gradient of oxygen, which is accompanied by an increase in HIF-1 α levels [1]. Springer and the Journal of Molecular Medicine, volume 85, 2007, pages 1301-1307, Hypoxia and Cancer, M. Christiane Brahimi-Horn, Johanna Chiche, Jacques Pouyssegur, Figure 1, with kind permission from Springer Science and Business Media.

1.1.2.2 Unregulated stroma

Tumor aggressiveness is driven by a dynamic relationship between tumor cells and their surrounding microenvironment, i.e. the stroma [41]. The tumor stroma is comprised of deposited ECM proteins, specifically collagen I and fibronectin, and several types of cells, including fibroblasts, myofibroblasts, endothelial cells, smooth muscle cells, pericytes, and infiltrating immune cells [41]. In many solid tumors, such as breast, stomach, pancreatic, and colon, the stroma can compose >90% of the total tumor mass [42, 43]. While physiological stroma, which contains a normal ECM, regulated vasculature, and fewer fibroblasts and immune cells, acts to hinder tumor maturation, the tumor stroma is oncogenic and promotes an aggressive phenotype

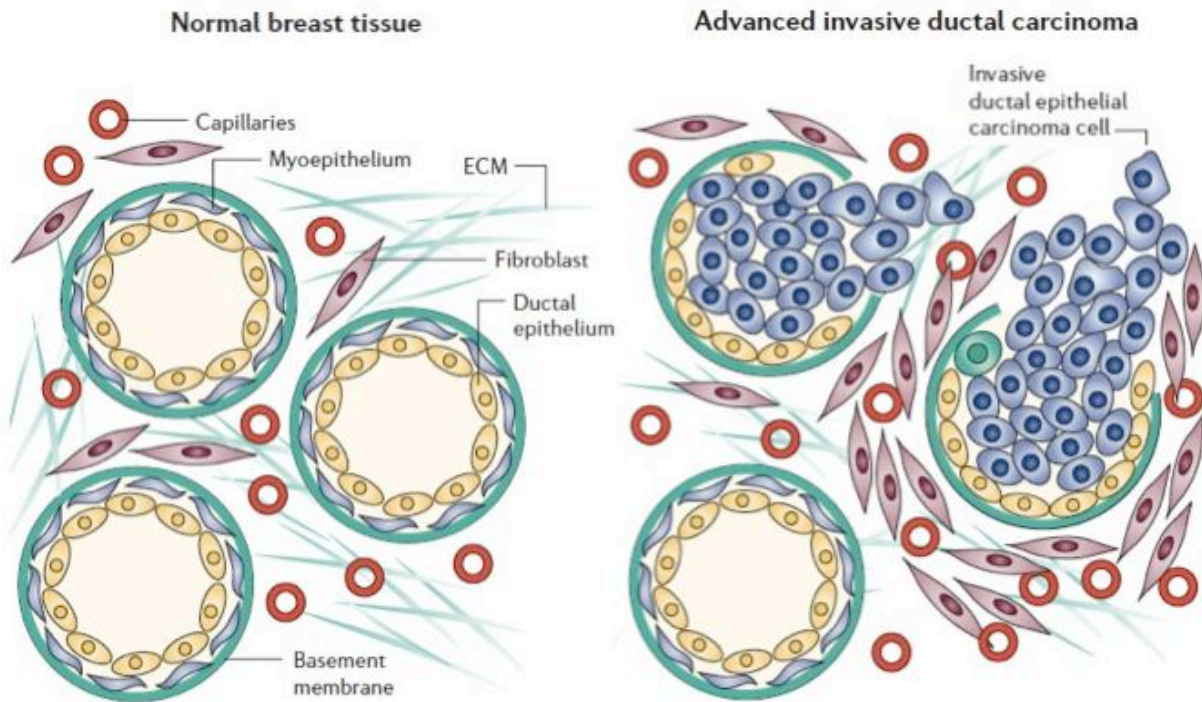


Figure 1.2. Tumor-stroma interactions during mammary ductal carcinoma progression. In normal breast tissue, the epithelial layers are separated from the surrounding stroma by an intact basement membrane. During invasive ductal carcinoma, cancer cells (transformed epithelia) proliferate without control, leading to a ruptured basement membrane and the formation of irregular duct-like areas without a defined basement membrane. In addition, the surrounding stroma becomes fibrotic from the deposition of fibrillar ECM and densely populated with infiltrating myofibroblasts, immune cells, and newly formed capillaries. Reprinted by permission from Macmillan Publishers Ltd: [Nature Reviews Cancer] [4], © 2006.

(Fig. 1.2) [44].

Fibroblasts are the most prevalent cell type within the stroma of several cancers [45]. During tumor development, ~80% of stromal fibroblasts undergo 'activation' to myofibroblasts (also referred to as cancer associated fibroblasts, CAFs), in which their phenotypes are altered to promote increased proliferation and expression of different ECM proteins and tumor-specific growth factors [4, 46]. Myofibroblasts originate primarily from normal fibroblasts in response to paracrine signaling from surrounding tumor cells [45], as well as from interstitial fibroblasts, perivascular fibroblasts, and venous smooth muscle cells [47]. Myofibroblasts play a major role in cancer progression through mediating the inflammatory response, remodeling the ECM, stimulating cancer cell proliferation, enhancing neovascularization, and providing potentially oncogenic signals [4, 48]. Immune cells within the tumor stroma can have both a positive and a negative effect on tumor development depending on the type of cancer and the immune cells involved. Macrophages infiltrate tumors in response to hypoxia, provoking tumor aggressiveness through secreting pro-angiogenic growth factors [49]. Similarly, mast cells infiltrate tumors in response to secreted chemokines and have been implicated in contributing towards angiogenesis in pancreatic islet tumors [50]. Alternatively, when monitoring invasive breast cancer, mast cells within the stroma represent a positive marker, indicating a good prognosis [51].

Desmoplasia, defined as the synthesis and deposition of ECM proteins, specifically fibrillar collagens, fibronectin, glycosaminoglycans, and proteoglycans, is a primary mechanism through which the stroma augments aggressive behavior during tumor development. This process is enforced by myofibroblasts and leads to the development of a dense, hard stroma [42, 43, 45, 52]. To highlight the magnitude of the desmoplastic response, it has been reported that the elastic moduli of conventional transgenic mice tumor models is 24-fold greater than normal mouse mammary gland [53]. The freshly deposited desmoplastic ECM is quickly neovascularized by newly formed capillaries and populated by invasive stromal and tumor cells [43]. In order to facilitate tumor invasiveness and vascular remodeling, tumor and stromal cells, in particular myofibroblasts [54], secrete matrix metalloproteinases (MMPs), which are ECM-degrading proteases [55, 56]. MMPs also enhance angiogenesis through regulating the release of angiogenic factors that have attached to the ECM [43, 57]. This continuous progression of matrix deposition, matrix remodeling, cell infiltration, and angiogenesis fosters a highly malignant microenvironment that drives tumor aggressiveness.

1.1.2.3 Aberrant microvasculature

Microscopic tumors remain in a dormant state for as long as there is balance between endogenous angiogenic promoters and inhibitors within the budding tumor microenvironment [7, 8]. Several well-known endogenous inhibitors of angiogenesis are normal components and/or internal fragments of ECM and fibrinolytic proteins [58]. For example, thrombospondin-1 is a large, modular ECM protein [59], angiostatin is a fragment of plasminogen [60], and endostatin is a fragment of type XVIII collagen [61]. These protein inhibitors, among many others, govern initial tumor growth through maintaining an avascular microenvironment. However, severe changes in the microenvironment, such as chronic hypoxia [1], can shift this balance to an angiogenic phenotype through upregulating the expression of angiogenic promoters, including vascular endothelial growth factor (VEGF), basic fibroblast growth factor (bFGF), IL-8, and platelet-derived growth factor (PDGF), among many others [6-8]. These pro-angiogenic factors interact with surrounding microvascular endothelial cells, initiating a sequence of events that culminates with new vessel formation. The general mechanism of angiogenesis follows six steps: (1) endothelial cell secretion of proteases and plasminogen activators, leading to degradation of the basement membrane, (2) invasion into the interstitial ECM, (3) proliferation, (4) lumen

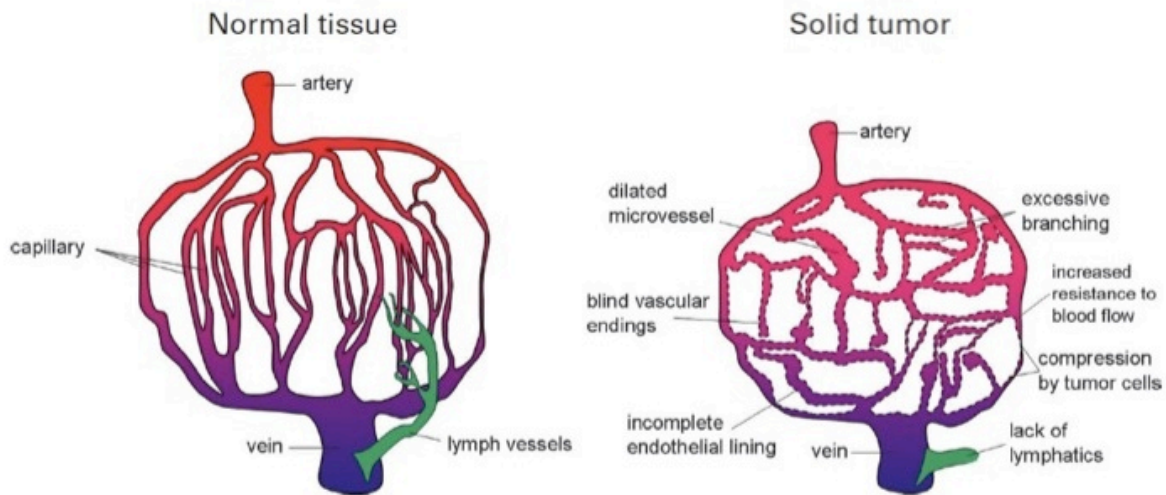


Figure 1.3. Schematic comparison of normal tissue and solid tumor vasculature. The tumor vasculature is dysregulated and tortuous leading to inefficient oxygen and nutrient exchange [2]. Olivier Trédan, Carlos M. Galmarini, Krupa Patel, Ian F. Tannock. Drug resistance and the solid tumor microenvironment. *J Natl Cancer Inst.* 2007; 99(19): pages 1441-54, by permission of Oxford University Press.

formation, (5) deposition of a new basement membrane, and (6) secretion of chemokines to attract pericytes for vessel stabilization [62, 63].

As a result of unregulated angiogenic growth factor expression and a dynamic stroma, the tumor vasculature is highly heterogeneous and tortuous with aberrant blood flow, chaotic branching, uneven vessel lumens, blunt-ended vessels, vascular shunts, areas of necrosis, and increased vascular density (Fig. 1.3) [2, 64, 65]. The pericytes and basement membrane, which provide stability to physiological vasculature, are also abnormal, leading to augmented vessel permeability and subsequent increased interstitial fluid pressure [65]. In addition, tumor vessels display inadequate musculature and innervation, which inhibits physiological feedback to the metabolic demands of the growing tumor [66]. Therefore, this irregular vasculature is exceedingly inefficient at conducting oxygen and nutrient exchange resulting in sustained regions of hypoxia and incessant tumor growth [67, 68].

1.1.3 Advantages of three-dimensional cell culture systems

As the dysregulated nature of the tumor microenvironment continues to be unraveled, *in vitro* cell culture systems must progress to accurately model these dynamic tumor-stroma interactions. For several decades, *in vitro* cancer research has primarily been conducted by culturing cells in 2D monolayers on Petri dishes, well plates, and glass slides [33]. While these systems are sufficient for analyzing epithelial cells when coated with specific ECM proteins and provided appropriate growth medium [69], 2D studies involving cancer cells, which transform *in vivo* to escape a monolayer architecture, may generate misleading results. Cancer cells, like most cells, exist *in vivo* within a 3D microenvironment where cues from the surrounding ECM dictate cell-cell interactions, cell migration, phenotype differentiation, and oxygen, nutrient, and waste transport [33, 70]. 2D cell culture systems are unable to reproduce these microenvironmental cues and responses in their entirety. To be more specific, cells cultured as a monolayer immediately experience differences in gene expression and metabolism as a result of changes in morphology, ECM interactions, and gas exchange. Attachment to a hard, flat surface (e.g. polystyrene and glass) leads to loss of differentiation markers and altered cell surface receptor clustering and orientation. This results in unnatural polarization of integrin binding sites, which directly influences intra-cellular, autocrine, and paracrine signaling. Cell migration is also

impacted as cells are restricted to 2D movement and are no longer challenged by a surrounding ECM [26, 33, 44, 70].

3D cell culture systems recapitulate many of the microenvironmental cues important for acquiring an *in vivo* phenotype, specifically cell-cell interactions, cell-ECM interactions, mechanical stimulation, and growth factor exchange [31]. Culturing cells within 3D matrices encourages the formation of growth factor gradients, which develop as a result of soluble growth factor attachment to matrix proteins. These gradients promote proper cell migration, proliferation, and differentiation [26, 31, 33, 71]. Additionally, mechanical stimulation and cell adhesion within the 3D matrix directly affect cell contractility and intra-cellular signaling [31]. As opposed to the cellular homogeneity characteristic of cell culture monolayers, 3D cell culture systems allow for cellular heterogeneity, including hypoxic, necrotic, proliferating, and non-proliferating cells [44]. This heterogeneity has been shown to promote increased expression of angiogenic-specific genes in 3D *in vitro* tumor models, such as IL-8, HIF-1 α , and VEGF [72-74].

In addition, cancer cells cultured within 3D matrices have been shown to respond to therapeutic stimuli, such as chemotherapy and radiation treatment, similar to *in vivo* biological systems [75, 76]. Specifically, 3D *in vitro* tumor models have demonstrated a developed resistance to anticancer agents [75, 77, 78], which is a distinct characteristic of malignant tumors. It is believed that this resistance may be a result of many different factors associated with 3D cell culture, including: (1) decreased drug availability within the growing tumor mass as compared to cell culture monolayers [75], (2) deposition of ECM proteins, which helps obstruct drug infiltration [78, 79], and (3) enhanced cell-cell and cell-matrix interactions [80, 81]. E-cadherin, an adhesion protein expressed during cell-cell interactions, has been shown to increase apoptosis resistance through arresting the cells in the G1 phase, which helps avoid cell cycle-dependent chemotherapy effectiveness [76]. Integrin binding to ECM components, such as collagen IV, fibronectin, and tenascin, has also been shown to reduce chemotherapy-induced apoptosis [82].

Although a majority of *in vitro* cancer research is still conducted using 2D monolayers, for the reasons discussed above, a growing number of investigators are beginning to incorporate 3D cell culture models into their research.

1.2 Literature review

The first 3D cell culture models used for studying tumor biology and drug responsiveness *in vitro* were multicellular tumor spheroids (MCTS) [83]. MCTS are tightly bound aggregates of tumor cells that form under non-adherent conditions using several techniques, including gyratory and spinner flasks [84], rotary cell culture systems [85], and liquid overlay cultures [86]. These compact spheroids range in diameter from 20 μm to 1 mm and resemble the structure and function of avascular, microscopic tumors. The 3D architecture of the MCTS encourages cell-cell and cell-matrix interactions that promote an *in vivo*-like phenotype [44, 83, 87]. As opposed to 2D monolayers, MCTS contain cellular heterogeneity with proliferating and non-proliferating phenotypes, hypoxic and necrotic oxygen availability, and surface vs. buried cell exposure [33]. In addition, tumor and stromal cells can be co-cultured to create more physiologically accurate spheroids [44].

With the advent of tumor engineering, *in vitro* tumor models have progressed to include a matrix component that supports more complex 3D cell growth. These systems utilize a variety of natural and synthetic polymeric scaffolds, as highlighted in Table 1.1. While natural scaffolds tend to provide more favorable cell adhesion and cell-mediated matrix degradation, synthetic scaffolds are mechanically stronger and allow for a greater degree of customization. Many of these systems have successfully recapitulated important aspects of the *in vivo* tumor microenvironment and/or have demonstrated drug responses similar to *in vivo* situations. Table 1.1 gives an overview of recent 3D *in vitro* tumor models. For a thorough review of *in vitro* tumor angiogenesis models, refer to **Chapter 4**.

Table 1.1 Recent 3D *in vitro* tumor models

Type of scaffold	Cell line	Observations
<i>Natural</i>		
Porous chitosan	MCF7	Increased resistance to tamoxifen as compared to 2D monolayers [88]
Porous chitosan-gelatin	NCI-H460	Tumor spheroids form within scaffold, demonstrating upregulation of fibronectin and N-cadherin; Increased resistance to topotecan, paclitaxel, and oxaliplatin [89]
Porous collagen scaffolds	MCF7	Upregulation of pro-angiogenic GFs, MMPs, and EMT markers; Cells cultured within the 3D scaffolds generated larger tumors when implanted <i>in vivo</i> as compared to cells cultured in 2D monolayers [90]
Hyaluronic acid hydrogel	C4-2B	Cell clustering and spheroid formation within the hydrogel led to a gradient in drug response with cells on the periphery of the tumor mass killed first [91]
	LNCaP	Large spheroids formed in response to EGF signaling, demonstrating cell-cell contacts with E-cadherin expression and upregulation of VEGF and IL-8 [92]
Silk fibroin protein matrix	MDA-MB-231	Presence of RGD sequence promoted proliferation and migration through the scaffold; Upregulation of MMP-9 [93]
Alginate hydrogel	OSCC-3, U87	VEGF secretion highest under hypoxic conditions and IL-8 secretion highest under ambient conditions; RGD-modification caused increased IL-8 secretion [74]
Collagen hydrogel	MDA-MB-231	Hypoxia and necrosis developed as a result of oxygen and nutrient limitations leading to upregulation of VEGF [94]
	MDA-MB-231	Minitumor spheroids (tumor cells, fibroblasts, and endothelial cells) embedded in hydrogel; Angiogenic sprouting and response to anti-angiogenic inhibitors similar to <i>in vivo</i> [95]
<i>Synthetic</i>		
Porous poly(lactic acid) microparticles modified with poly(vinyl alcohol)	MCF7	Formation of tissue-like structures; Increased resistance to doxorubicin, paclitaxel, and tamoxifen due to decreased drug uptake compared to 2D monolayers [78, 96]
Porous poly(lactic-co-glycolic acid)	OSCC-3	Development of hypoxic and necrotic regions; Angiogenic GF (VEGF, bFGF, IL-8) secretion similar to <i>in vivo</i> ; Increased drug resistance compared to 2D monolayers [77]
Polyethylene glycol (PEG) hydrogel	LNCaP	PEG was modified with RGD and MMP cleavage sites; tumor-like structures formed with hypoxic and apoptotic regions [97]

1.3 Objective

This project originated as a collaboration amongst a group of professors from Virginia Tech and the Wake Forest Institute for Regenerative Medicine with the goal being to develop a three-dimensional tumor model for studying tumor angiogenesis. The idea was to grow a solid tumor around a tissue engineered vessel within a bioreactor system that conducts physiological flow rates. Initial vessel-based scaffold options were selected based on the expertise of the original collaborators, including a composite polycaprolactone (PCL)/collagen I electrospun scaffold [98], bacterial cellulose [99], and decellularized porcine arteries [100]. Tumors were to be grown by either seeding cancer cells directly onto the scaffold or through wrapping excised tumor tissue around the vessel. Through gaining a better understanding of tumor development from hands-on experience in the lab as well as the literature, the focus of the project was adjusted to study the pre-vascularized stages of tumor development before attempting an *in vitro* tumor angiogenesis model. In addition, the incorporation of flow was abandoned to further reduce the initial complexity of the model. Still, the primary objective has remained constant – develop a three-dimensional *in vitro* tumor angiogenesis model that reproduces the phenotypes and physiological responses of the *in vivo* tumor microenvironment without the aid of exogenous stimuli. The detailed process followed to achieve this goal is outlined in sub-section **1.4 Specific Aims**.

1.4 Specific aims

Aim 1: Identify an appropriate scaffold for supporting three-dimensional in vitro tumor growth

It has been well established in the literature that cells cultured within a three-dimensional (3D) *in vitro* environment have the ability to acquire phenotypes and respond to stimuli analogous to *in vivo* biological systems [30, 31]. Despite this, a majority of cancer research is still conducted using 2D cell culture monolayers. Several different types of scaffolds, which are typically used in tissue engineering applications, were investigated for their potential to support 3D *in vitro* tumor growth. **Chapter 2** (published as “Investigation of cancer cell behavior on nanofibrous scaffolds” in *Materials Science and Engineering C*) and **Appendix B** (unpublished results) present a few of our unsuccessful attempts at achieving sufficient 3D cell growth using bacterial cellulose, a composite polycaprolactone (PCL)/collagen I electrospun scaffold, and a highly porous poly(L-lactic acid) (PLLA) electrospun scaffold. From these studies we came to three conclusions: 1) without significant surface modification, bacterial cellulose does not encourage cell adhesion and proliferation, 2) PCL/collagen I electrospun scaffolds promote excellent cell adhesion and proliferation, but the architecture of the scaffolds do not encourage cell infiltration, and 3) highly porous PLLA electrospun scaffolds allow for noticeable cell infiltration that is still inadequate for generating 3D tumor growth.

In addition, embedding cancer cells within sodium alginate hydrogels was briefly evaluated (no substantial data gathered). While sodium alginate is biocompatible and the gentle polymerization process allows for the inclusion of cells and an immediate 3D culturing environment, it is biologically inert. Modification with the tripeptide RGD (Arg-Gly-Asp), a short amino acid sequence that preferentially binds to receptors on cell surfaces [101], has been shown to promote cell adhesion to sodium alginate, but degradation through cellular interactions is not possible [102, 103]. Therefore, collagen I hydrogels were ultimately identified as the most appropriate scaffold for facilitating 3D *in vitro* tumor growth. Characterization of cancer cell growth within the collagen I hydrogels is the focus of Aim 2.

Aim 2: Characterize cancer cell growth within collagen I hydrogels

Collagen I is highly prevalent in many carcinomas, constituting a major portion of the stromal ECM [52, 104]. A myofibroblast-mediated build-up of collagen I, i.e. desmoplasia,

occurs during tumor progression and is responsible for elevated tumor stroma stiffness [41, 52]. Furthermore, remodeling of collagen I during *in vivo* tumor progression has been reported to stimulate endothelial cell migration and angiogenesis through releasing matrix-bound pro-angiogenic growth factors [105, 106]. For these reasons, collagen I hydrogels were chosen as an appropriate scaffold for developing the *in vitro* tumor model. In addition, cells can remodel and degrade the collagen matrix during proliferation and invasion [107], and the gentle polymerization process allows for the immediate culture of cells within a 3D environment.

Our hypothesis was that collagen I hydrogels could facilitate adequate 3D cell culture growth for developing an *in vitro* tumor model that mimics key characteristics of *in vivo* tumor progression. This simple model was composed of MDA-MB-231 human breast cancer cells cultured within dense collagen I hydrogels. Limitations in oxygen diffusion were enforced through altering the hydrogel thickness and competition for nutrients was enforced through altering the seeding density. Manipulating these culturing conditions encouraged the development of *in vivo*-characteristic regions of necrosis and hypoxia and a subsequent upregulation of VEGF gene expression. This study demonstrated that achieving an appropriate phenotypic response is highly dependent on the culturing conditions, and this response can be established independent of exogenous stimuli (hypoxic chamber). **Chapter 3** presents these results, which were published as “3D *in vitro* bioengineered tumors based on collagen I hydrogels” in *Biomaterials*.

Aim 3: Induce angiogenic sprouting through co-culturing endothelial cells with the pro-angiogenic in vitro tumors

In vitro tumor angiogenesis models are important tools for accurate evaluation and refinement of anti-angiogenesis therapies. However, many current systems rely on exogenous stimuli and incorrect culturing conditions to induce an angiogenic response. This presents a problem since determining the therapeutic impact of potential angiogenic inhibitors is highly dependent on the pro-angiogenic stimulus. If the stimulus is incorrect (composition and/or concentration of exogenous growth factors) or the system is physiologically-inaccurate (incorrect spatial relationships or endothelial polarity), any conclusions obtained using those models may be unreliable in an *in vivo* setting.

Our hypothesis was that paracrine signaling between tumor and endothelial cells co-cultured in a spatially-relevant manner would be sufficient for inducing an angiogenic response in the absence of exogenous pro-angiogenic growth factors. The co-culture model was composed of microvascular endothelial cells cultured as an endothelium on the surface of an acellular collagen I hydrogel under which MDA-MB-231 cells were cultured in a separate collagen I hydrogel. These bilayered bioengineered tumors were cultured in transwell inserts to provide two individual medium compartments for the different cell types. This co-culture experimental setup maintained the appropriate spatial relationship between the tumor and endothelial cells as well as correct endothelial cell polarity. In response to paracrine signaling from the MDA-MB-231 cells (and in the absence of exogenous pro-angiogenic growth factors), the endothelial cells demonstrated a significant increase in proliferation, rapidly developed an elongated morphology, and assembled into a capillary-like tubule network beneath the surface of the confluent monolayer. The co-culture induced *in vitro* angiogenesis was shown to be dependent on matrix concentration, growth factor involvement, and duration of co-culture. **Chapter 4** presents these results, which have been submitted as “*In vitro* angiogenesis induced by tumor-endothelial cell co-culture in bilayered, collagen I hydrogel bioengineered tumors” to *Tissue Engineering Part C*.



Investigation of cancer cell behavior on nanofibrous scaffolds

Christopher S. Szot^a, Cara F. Buchanan^a, Paul Gatenholm^{a,b},
Marissa Nichole Rylander^a, Joseph W. Freeman^{a,*}

^a School of Biomedical Engineering and Sciences, Virginia Polytechnic Institute and State University, Blacksburg, Virginia 24061, USA

^b Department of Chemical and Biological Engineering, Chalmers University of Technology, SE-412 96 Göteborg, Sweden

ARTICLE INFO

Article history:

Received 29 September 2009

Received in revised form 20 November 2009

Accepted 1 December 2009

Available online 11 December 2009

Keywords:

Nanofibrous scaffold

Electrospinning

Polycaprolactone

Collagen I

Bacterial cellulose

Cancer

ABSTRACT

Tissue engineering and the use of nanofibrous biomaterial scaffolds offer a unique perspective for studying cancer development *in vitro*. Current *in vitro* models of tumorigenesis are limited by the use of static, two-dimensional (2D) cell culture monolayers that lack the structural architecture necessary for cell-cell interaction and three-dimensional (3D) scaffolds that are too simplistic for studying basic pathological mechanisms. In this study, two nanofibrous biomaterials that mimic the structure of the extracellular matrix, bacterial cellulose and electrospun polycaprolactone (PCL)/collagen I, were investigated as potential 3D scaffolds for an *in vitro* cancer model. Multiple cancer cell lines were cultured on each scaffold material and monitored for cell viability, proliferation, adhesion, infiltration, and morphology. Both bacterial cellulose and electrospun PCL/collagen I, which have nano-scale structures on the order of 100–500 nm, have been used in many diverse tissue engineering applications. Cancer cell adhesion and growth were limited on bacterial cellulose, while all cellular processes were enhanced on the electrospun scaffolds. This initial analysis has demonstrated the potential of electrospun PCL/collagen I scaffolds toward the development of an improved 3D *in vitro* cancer model.

© 2009 Elsevier B.V. All rights reserved.

1. Introduction

In vitro tumor models are invaluable systems for studying the dynamic and progressive behavior of cancer under controlled conditions. They allow systematic investigation of specific therapeutic treatments without the complexity of *in vivo* models. Currently, the progression of cancer research is limited by the available experimental systems for studying this complex disease; as such current *in vitro* models are too simplistic to replicate an accurate *in vivo* response. 2D cell monolayers cultured on tissue culture plastic have long been used for studying cancer development and determining drug efficacy. However, recent advances in tissue engineering have shown that cells cultured on scaffolds that mimic the extracellular matrix and/or in a 3D environment develop a phenotype more representative of cells cultured *in vivo* [1,2]. Cells cultured in 3D scaffolds differ from cells cultured in 2D monolayers in terms of cell density [3], extracellular matrix synthesis [4], cell surface receptor expression [5], cell contraction [6], intracellular signaling [7], and metabolic functions [8]. Recently, *in vitro* 3D models utilizing cancer cell encapsulation in alginate-based microcapsules [9] and porous polymer microparticles [2] have demonstrated more accurate physiological tumor structures. Although these models have provided significant insight into cancer cell interactions in 3D they do not mimic the fibrous nature of

biological tissues. Therefore, there remains a limited understanding of the pathological processes of tumorigenesis.

Tissue engineering is a field of biomedical research focused on constructing functional 3D tissues using a specifically coordinated combination of cells, growth factors, scaffold materials, and culturing conditions. This experimental approach can also be applied to developing *in vitro* pathological systems for scientific research [1,2]. A key aspect in tissue engineering different types of tissues is the composition and structure of the scaffold material. Cell adhesion and migration are dependent on the composition of the scaffold, and the cells' ability to remodel the material depends on the scaffold's sensitivity to proteolytic enzymes [1]. Scaffolds with nano-scale structures have been shown to enhance cell adhesion, proliferation, and extracellular matrix synthesis [10], as opposed to micro-scale scaffolds. Scaffolds on the nano-scale have a much larger surface area that allows for increased protein adsorption and binding sites for cell surface receptors [11]. In this study, two biomaterials with nano-scale structures similar to the extracellular matrix, bacterial cellulose and electrospun polycaprolactone (PCL)/collagen I (Fig. 1), were analyzed for their effect on cell viability, proliferation, adhesion, infiltration, and morphology.

Bacterial cellulose (BC) is a polysaccharide synthesized and secreted extracellularly into a nanofibril network structure by the *Acetobacter xylinum* bacteria. BC is currently being investigated as a scaffolding material in cartilage and blood vessel tissue engineering studies, with data demonstrating viability, proliferation, and adhesion of cells on the surface of the material [12–14]. These scaffolds can be

* Corresponding author. Tel.: +1 540 231 5686; fax: +1 540 231 9738.

E-mail address: jwfreeman@vt.edu (J.W. Freeman).

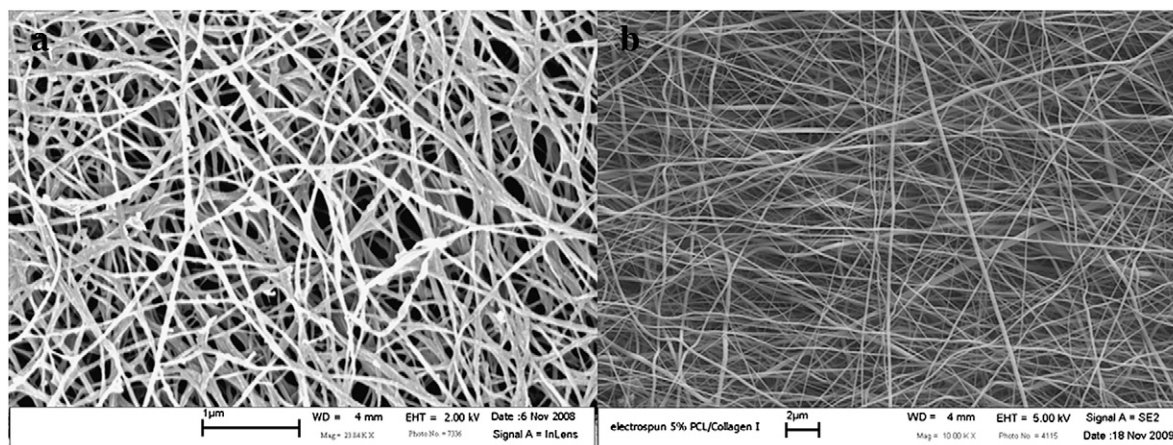


Fig. 1. FESEM was used to show the scaffold morphology of (a) bacterial cellulose and (b) electrospun PCL/collagen I. Both scaffolds are a collection of non-woven, unorganized nanofibers. The fiber diameter of the bacterial cellulose is considerably smaller than the 5% (w/v) electrospun 1:1 PCL/collagen I.

designed with varying porosity, using an assortment of leaching techniques, to promote infiltration of cells and 3D growth. At the microscopic level, BC nanofibers are similar to collagen fibers [15,16]. Previous studies demonstrating favorable cell–scaffold interactions, the potential for incorporating a porous network, and the natural nanofibrous structure of BC makes it an attractive scaffold for developing an *in vitro* cancer model.

Electrospinning is a scaffold fabrication technique used in many diverse tissue engineering applications, including bone [17], cartilage [18], muscle [19], and blood vessel [20] studies. This process uses a high voltage electric field to produce non-woven nanofibers with micro-scale interconnected pores, resembling the extracellular matrix [17]. Electrospinning is a promising approach to developing tissues *in vitro*, because the structure of the electrospun scaffolds allows for cells to infiltrate the material and proliferate in 3D. Polymer blends and concentrations can be varied to obtain specific fiber diameters, mechanical properties, porosity, degradation, and cellular responses [21].

Electrospun nanofibers of PCL have been extensively studied for many tissue engineering applications [22–24]. PCL is non-toxic, inexpensive, and exhibits a slow hydrolytic degradation [25] that is commensurate with the rate of neo-tissue formation and remodeling [22]. Other tissue engineering studies have investigated electrospinning natural materials, such as collagen, in order to more accurately mimic the natural extracellular matrix [26,27]. Collagen I contains cell adhesion RGD (arginine–glycine–aspartic acid) sequences that promote cell attachment and proliferation [28]. However, the high degradation rates of natural polymers such as collagen often result in their use in composites [29]. The material and structural properties of PCL combined with the natural biocompatibility and biodegradability of collagen I in an electrospun nanofiber scaffold is expected to engender quality mechanical properties while still providing the biocompatibility and controlled degradation rates sufficient for neo-tissue formation.

Cancer cell behavior was investigated on BC and electrospun PCL/collagen I scaffolds using a variety of techniques to analyze cell viability, proliferation, adhesion, infiltration, and morphology. Three separate cancer cell lines were cultured to determine if the selected nanofibrous biomaterials are suitable scaffolds for an *in vitro* cancer model. An endothelial cell line was also cultured on the nanofibrous scaffolds as a preliminary investigation for the feasibility of a co-culture system.

2. Materials and methods

2.1. Bacterial cellulose

Bacterial cellulose (BC) was fabricated using methods described previously [15,16]. Briefly, BC was synthesized by *A. xylinum* subsp.

sucrofermentas BPR2001. Pellicles were statically grown in corn steep liquid media using Roux flasks, purified by treatment with 0.1 M NaOH, rinsed with DI water, and steam sterilized. Prior to all cell culture experiments, BC scaffolds were pre-treated in 0.05% fibronectin (Sigma Aldrich, St. Louis, MO, USA) for 2 h to enhance cell attachment.

2.2. Electrospun scaffold preparation

Electrospun scaffolds were fabricated using a 1:1 weight ratio polymer blend of collagen type I from calf skin (Elastin Products Co., Owensville, MO, USA) and poly(ϵ -caprolactone) (PCL, inherent viscosity = 1.0–1.3 dL/g, Lactel Absorbable Polymers, Pelham, AL, USA). The two polymers were mixed in 1,1,1,3,3,3-hexafluoro-2-propanol (99+%) (HFIP, Sigma Aldrich) to achieve total solution concentrations (w/v) of 5, 8, 10, and 15%. Using a syringe pump (KDS120, KD Scientific Inc., Holliston, MA, USA), a total solution volume of 5 ml was delivered out of an 18 gauge blunt tip syringe needle at a constant rate of 3 ml/h. The needle was kept at a distance of 10 cm from a spinning mandrel with a rotation rate of 1500 rpm. Using a higher power voltage supply (Gamma High Voltage Research, Inc., Ormond Beach, FL, USA), a positive voltage of +12 kV was applied to the polymer solution and a negative voltage of –8 kV was applied behind the spinning mandrel to attract the fibers.

2.3. Cell culture

Multiple cancer cell lines were used in this study to permit characterization of their potentially unique response to varying scaffold materials. A human androgen-independent prostate cancer cell line (PC-3), a murine renal cancer cell line (RENCA), and a human breast cancer cell line (MDA-MD-231) were purchased from American Type Culture Collection (Manassas, VA, USA). Additionally, a human microvascular endothelial cell line (HMEC-1) was provided by Dr. Edwin Ades and Mr. Francisco J. Candal of Center for Disease Control and Prevention (Atlanta, GA, USA) and Dr. Thomas Lawley of Emory University (Atlanta, GA, USA).

The PC-3 cell line was cultured in GIBCO® RPMI Medium 1640 (Invitrogen, Carlsbad, CA, USA) and supplemented with 10% fetal bovine serum (FBS, Sigma Aldrich) and 1% Penicillin Streptomycin (Invitrogen). The RENCA cell line was cultured in GIBCO® RPMI Medium 1640 (Invitrogen, Carlsbad, CA, USA) and supplemented with 10% FBS (Sigma Aldrich), 1% Penicillin Streptomycin (Invitrogen), and 1% sodium pyruvate (Cellgro Mediatech, Manassas, VA, USA). The MDA-MB-231 cell line was cultured in GIBCO® DMEM/F12 (1:1) + L-Glutamine, + 15 mM HEPES (Invitrogen) and supplemented with 10% FBS (Sigma Aldrich) and 1% Penicillin Streptomycin (Invitrogen). The

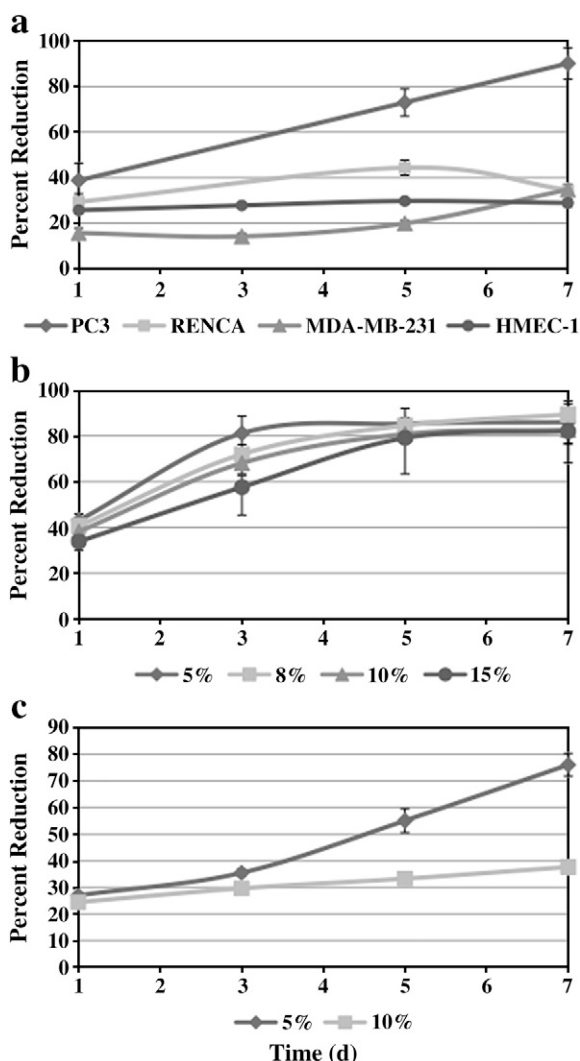


Fig. 2. An alamarBlue® cell viability reagent was used to analyze cell viability and proliferation over a 7 day period for (a) all three cancer cell lines and the HMEC-1 cell line on bacterial cellulose pre-treated with 0.05% fibronectin as well as (b) RENCA and (c) HMEC-1 cells on different w/v concentrations of electrospun 1:1 PCL/collagen I. Similar trends were observed for PC-3 and MDA-MB-231 cells cultured on the electrospun scaffolds and therefore the data is not shown.

HMEC-1 cell line was cultured in MCDB 131 (Cellgro Mediatech) and supplemented with antibiotic/antimycotic (Cellgro Mediatech), 10 mM L-glutamine (Fischer Scientific, Pittsburgh, PA, USA), hydrocortisone (Sigma Aldrich), epidermal growth factor (Sigma Aldrich), and 10% FBS (Sigma Aldrich).

All cell cultures were incubated in a humidified atmosphere of 95% air and 5% CO₂ at a constant temperature of 37 °C. The duration of each cell study was 1 week and culture medium was replaced twice a week.

2.4. Cell proliferation and cytotoxicity assessment

An alamarBlue® cell viability reagent (Invitrogen) was used to analyze cell proliferation and cytotoxicity of the scaffolds. BC and

Table 1
Scaffold characterization: fiber diameter.

	Electrospun 1:1 PCL/collagen I polymer concentration (w/v)				Bacterial cellulose
	5%	8%	10%	15%	
Fiber diameter	424 nm ± 60	1156 nm ± 184	1613 nm ± 213	2236 nm ± 282	<100 nm

Mean fiber diameter and standard deviation were measured using ImageJ. Bacterial cellulose and the 5% (w/v) electrospun 1:1 PCL/collagen I scaffold are composed of nanofibers. Increasing the w/v concentration of the electrospun scaffolds resulted in an increase in fiber diameter to the micro-scale.

electrospun scaffolds were cut into samples with a diameter of 1.5 cm and placed in 24 well ultra low attachment polystyrene plates (Corning, Corning, NY, USA). Scaffold samples were sterilized using ethanol and washed repeatedly in phosphate buffered saline (PBS). Cells were seeded at a density of 20,000 cells/well. On days 1, 3, 5, and 7 all culture medium was replaced with medium containing 10% alamarBlue® reagent, and samples were allowed to incubate for 4 h. The absorbance of alamarBlue® was measured using a microplate reader (SpectraMax M2^e, Molecular Devices, Sunnyvale, CA, USA) at 570 nm with 600 nm as a reference wavelength. The same samples were used for each time point, and fresh culture medium was added following each reading.

2.5. Electron microscopy

Cell adhesion and fiber diameter were determined using field emission scanning electron microscopy (FESEM; Leo Zeiss 1550, Carl Zeiss, Thornwood, NY, USA). Scaffold samples were fixed using 1% and 3% glutaraldehyde followed by successive methanol washes of increasing concentration. Samples were then quenched in liquid nitrogen, freeze dried, and sputter coated in gold. Images were obtained at an accelerating voltage of 5 kV with a 7–8 cm working distance. Fiber diameter size was determined using ImageJ (Freeware provided by the NIH, Bethesda, MA, USA). Sixty randomly selected fibers from each scaffold (fifteen fibers from four different images) were measured to calculate the mean fiber diameter and standard deviation.

2.6. Confocal microscopy

Cell morphology was analyzed using a high-affinity probe for F-actin and DAPI to visualize nuclei. Scaffolds were prepared for 24 well plates as described. Cells were seeded onto the scaffolds at a density of 20,000 cells/well and allowed to proliferate for 4–7 days depending on the doubling time. Cells were then fixed with 3.7% paraformaldehyde and permeabilized using 0.5% Triton X-100 diluted in PBS. 1% BSA diluted in PBS was used as a blocking buffer. Samples were stained with Oregon Green® 488 phalloidin (Invitrogen) to detect F-actin and mounted with VECTASHIELD® mounting medium with DAPI (Vector Laboratories, Burlingame, CA, USA). Cell morphology was visualized using a laser scanning confocal microscope (Zeiss LSM 510, Carl Zeiss).

2.7. Statistical analysis

Cell viability data was analyzed for significance using a Student's *t*-test and ANOVA, where appropriate. *P* < 0.05 was considered significant.

3. Results and discussion

3.1. Cell viability and proliferation

Cell viability was determined based on the percent reduction of the alamarBlue® reagent, with an increase in percent reduction indicative of cell proliferation. Although all cell lines were viable when cultured on BC pre-treated with 0.05% fibronectin, only the PC-3 cells demonstrated any considerable proliferation (Fig. 2a). Pre-treating BC

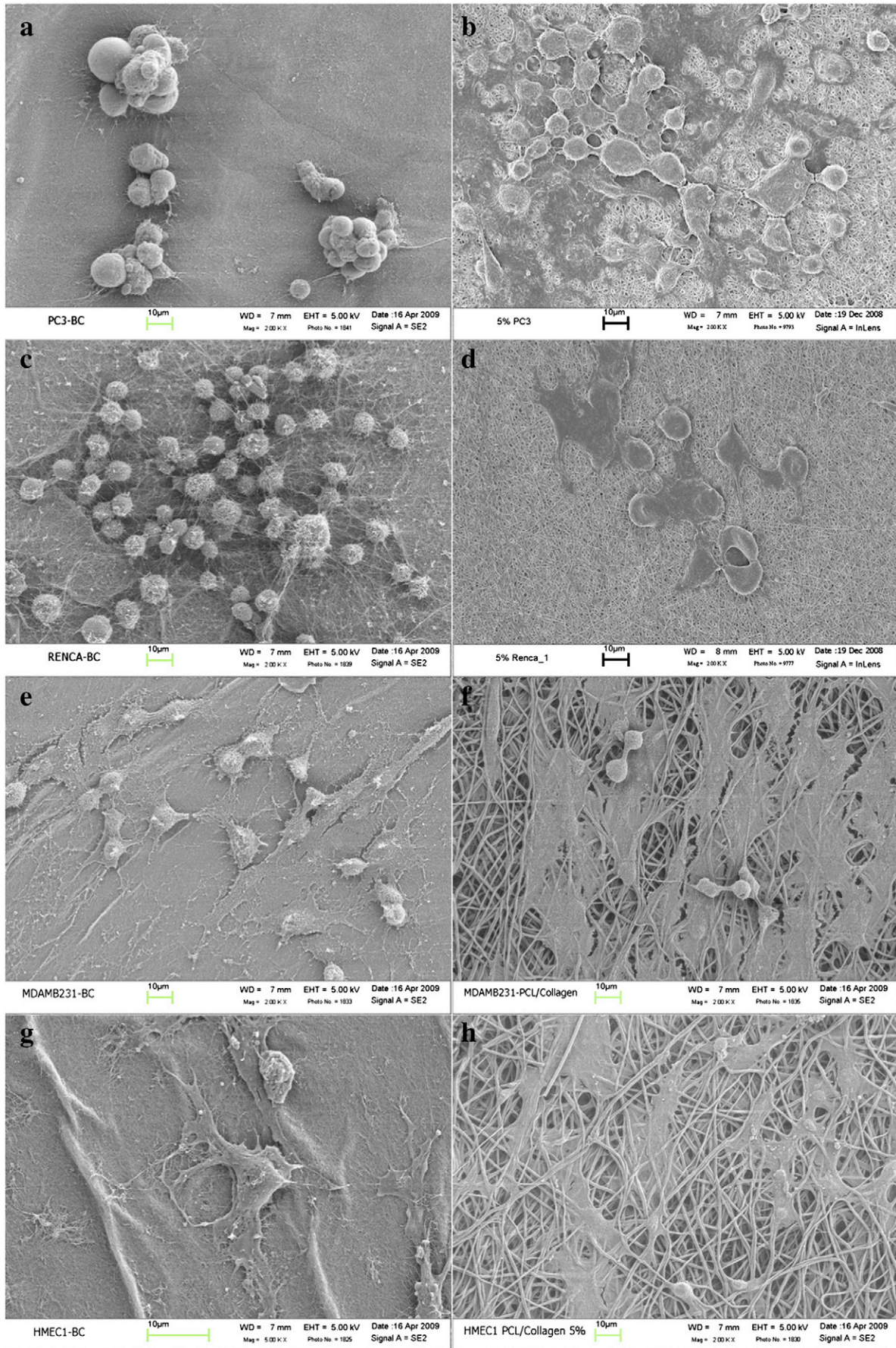


Fig. 3. Cell adhesion was characterized using FESEM. (a, b) PC-3, (c, d) RENCA, (e, f) MDA-MB-231, and (g, h) HMEC-1 cells were cultured on bacterial cellulose pre-treated with 0.05% fibronectin and 5% (w/v) electrospun 1:1 PCL/collagen I, respectively.

with fibronectin increased cell viability by 37.5% (data not shown), when compared to non-treated BC. The disparity in cell viability 24 h following seeding suggests that adhesion to BC varied among the cell lines. Lower adhesion correlated with reduced viability and proliferation. BC has a nano-scale structure (fiber diameter <100 nm; Table 1) ideal for harboring cell growth [10], however, viability and proliferation were limited. This suggests that without further surface modification, BC may not be compatible with the cell surface integrins expressed by the cancer and endothelial cells cultured during these experiments.

Both cell viability and proliferation were greater on the electrospun PCL/collagen I scaffolds as compared to BC. The PC-3, RENCA (Fig. 2b), and MDA-MB-231 cancer cell lines demonstrated steady proliferation over the first 3–5 days. The alamarBlue® reagent percent reduction data shows that proliferation slowed but viability remained constant towards the end of the study. Cancer cells lack cell–cell contact inhibition and will consequently proliferate into multilayered stacks with a sufficient nutrient source. It is probable that proliferation did not cease, but rather, due to limited space and nutrients, the growing cancer cells entered a dormant state, in which the cells were simultaneously proliferating and undergoing apoptosis at the same rate. A tumor will remain dormant until angiogenesis is initiated, supplying the tumor with the necessary oxygen and nutrients to continue 3D growth [30].

For the electrospun PCL/collagen I scaffolds there was a statistically significant correlation between fiber diameter, which is dependent on polymer concentration (Table 1), and cell viability. The alamarBlue® assay demonstrated that 24 h following cell seeding, cell viability was greatest on the 5% (w/v) electrospun scaffolds with viability decreasing as a function of increasing polymer concentration (Fig. 2b). This trend remained the same throughout the assay for all cancer cell lines studied. Only the RENCA viability data set is shown to avoid repetition. Cancer cell viability on the 5% electrospun scaffolds was significantly different than the other three polymer concentrations during proliferation (day 3) and both the 8% and 10% scaffolds were significantly different than the 15% scaffold. Once population capacity was reached we hypothesize that apoptosis began to counteract proliferation (day 5–7) allowing cell viability on all electrospun scaffolds to reach the same level. Therefore, cell viability among the varying polymer concentrations was no longer significantly different.

Differences in cell viability and proliferation were more evident with the HMEC-1 cells (Fig. 2c). HMEC-1 cells cultured on the 5% electrospun scaffolds proliferated at a much quicker pace than when cultured on the 10% electrospun scaffolds. HMEC-1 cell viability on the 5% electrospun scaffolds was significantly different than on the 10% electrospun scaffolds on days 3, 5, and 7. These differences were attributed to the variation in fiber size of the electrospun scaffolds. During electrospinning, polymer concentration is directly related to fiber diameter. Lower polymer concentrations produce scaffolds with smaller fiber diameters. The 5% electrospun scaffolds had a mean fiber diameter of 424 nm (Table 1), the only polymer concentration accurately classified as having a nano-scale structure. While cancer cells are less sensitive to the substrates and environments in which they grow, the HMEC-1 cells were clearly affected by the micro-scale structure of the greater polymer concentration electrospun scaffolds.

3.2. Cell adhesion

Cell adhesion on the scaffolds was characterized by SEM analysis. The electrospun PCL/collagen I scaffolds appeared to be more advantageous for cell adhesion as compared to BC pre-treated with fibronectin (Fig. 3). Cells cultured on BC were not spread out across the surface but spherical in shape. Despite steady proliferation, the PC-3 cells also did not appear to have completely adhered to

the surface. Treatment with fibronectin alone was not sufficient for allowing BC to be compatible with the cell surface integrins expressed by the cancer and endothelial cells. Further modification may be required for BC to sustain cell growth in an *in vitro* cancer model. Bodin et al. has shown that adhesion of human EC cells has been significantly improved when BC has been coated with xyloglucan-RGD bioconjugates. The hydrophilic nature of BC prevents protein adsorption and consequently cell adhesion [31].

Using collagen I in the electrospun scaffolds promoted cell adhesion, demonstrated by the favorable attachment of all cell lines to the four electrospun polymer concentrations, regardless of the fiber diameter (SEM images for 8, 10, and 15% electrospun scaffolds are not shown). Even though the 8, 10, and 15% electrospun mats have micro-scale structures, the RGD sequences present on collagen I ensured propitious attachment.

3.3. Cell infiltration

There was no observed infiltration of cells cultured on BC after 7 days and only limited signs of infiltration of the cells cultured on the electrospun scaffolds. The dense, nanofibrous structure of BC hinders cell infiltration in the absence of manufactured porosity. Similarly, cells cultured on the 5, 8, and 10% electrospun scaffolds did not exhibit cell infiltration because of the dense nature of their structures. However, when cultured on the 15% electrospun scaffolds, the RENCA cells began to migrate below the electrospun fibers (Fig. 4). With an average fiber diameter of 2.2 μm, there is increased spacing/porosity between adjacent fibers for cells to penetrate. These initial signs of cell infiltration into electrospun scaffolds have been seen elsewhere in the literature [32]. Increased infiltration is necessary for obtaining a 3D structure *in vitro*. Porosity can be magnified in the electrospun scaffolds through further modification of the electrospinning parameters or by salt leaching [33].

3.4. Cell morphology

Confocal microscopy revealed drastically different morphologies between cells cultured on the electrospun PCL/collagen I scaffolds and BC (Fig. 5). Similar to the SEM images, all three cancer cell lines cultured on BC were spherical in shape with no observable protrusions indicating surface adhesion. On the contrary, cells cultured on the electrospun PCL/collagen I scaffolds had distinct actin cytoskeletal

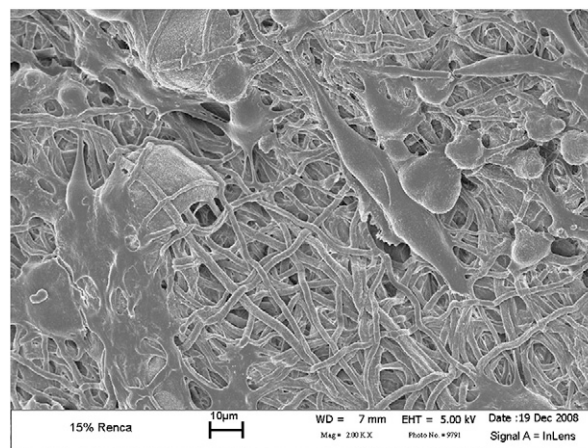


Fig. 4. Cell infiltration was analyzed using FESEM. Limited cell infiltration was observed when the cancer cells were cultured on the 15% (w/v) electrospun 1:1 PCL/collagen I. After 7 days of culturing, the RENCA cells began to migrate below the electrospun fibers.

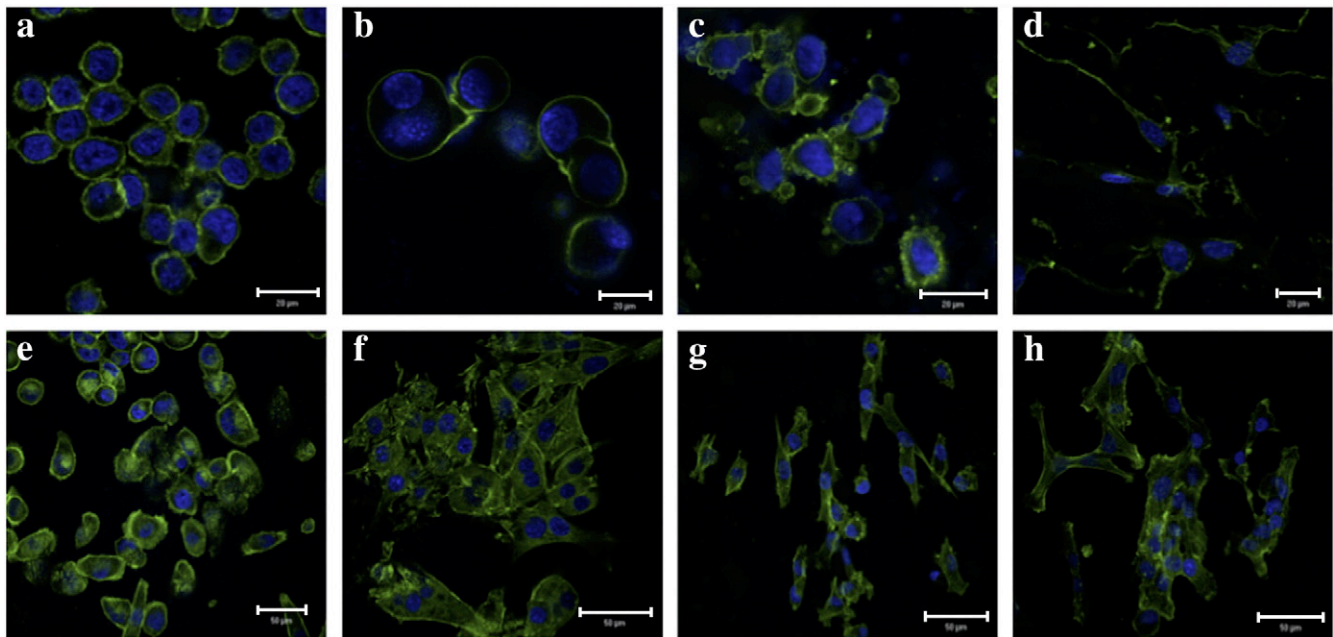


Fig. 5. Cell morphology was analyzed using Oregon Green® 488 phalloidin, a high-affinity probe for F-actin, and DAPI to visualize nuclei. (a, e) PC-3, (b, f) RENCA, (c, g) MDA-MB-231, and (d, h) HMEC-1 cells were cultured on bacterial cellulose pre-treated with 0.05% fibronectin and 5% (w/v) electrospun 1:1 PCL/collagen I, respectively.

structures. There were also initial signs of endothelial tubule formation (Fig. 5h), indicating endothelial migration across the surface.

4. Conclusions

The electrospun PCL/collagen I scaffolds were more conducive to cancer cell growth, as all cell lines cultured on these scaffolds demonstrated steady proliferation, adhesion, and a normal morphology. In contrast, BC sustained only limited cell adhesion, which led to decreased proliferation, viability, and an abnormal morphology. Partial cell infiltration was seen on the 15% electrospun PCL/collagen I scaffolds, however, in order for the electrospun scaffolds to successfully preserve 3D cancer growth *in vitro*, increased porosity must be engineered into the nanofibrous network. Endothelial cells were cultured on the nanofibrous scaffolds to demonstrate the feasibility of their inclusion in the *in vitro* cancer model for their potential use in forming vasculature within the tumor model. Similar to the cancer cell lines, proliferation of the endothelial cells was enhanced on the electrospun PCL/collagen I scaffolds. Additional studies must focus on measuring surface roughness, surface contact angle, and mechanical properties in order to explain the difference in cellular behavior between BC and the electrospun PCL/collagen I scaffolds.

Tumors remain in a dormant state in the absence of angiogenesis, which provides the cancer with oxygen and nutrients. At the onset of angiogenesis, tumors will rapidly grow to a clinically relevant size. It is anticipated that the co-culture of endothelial cells with cancer cells on a scaffold that permits 3D growth will enhance tumor formation by stimulating angiogenesis. A co-culture system will facilitate the development of a 3D *in vitro* cancer that can more accurately mimic the pathological process of tumorigenesis. Further investigation and modification of the electrospun PCL/collagen I scaffolds will allow us to determine if these scaffolds are suitable for obtaining this goal.

Acknowledgements

We would like to thank Dr. Sang Jin Lee for his assistance with electrospinning the PCL/collagen scaffolds and Dr. Aase Bodin for her contribution of bacterial cellulose. This work was funded by the Institute for Critical Technology and Applied Sciences at Virginia Tech.

References

- [1] L.G. Griffith, M.A. Swartz, *Nat. Rev., Mol. Cell Biol.* 7 (2006) 211 f.
- [2] J.L. Horning, S.K. Sahoo, S. Vijayaraghavalu, S. Dimitrijevic, J.K. Vasir, T.K. Jain, A.K. Panda, V. Labhasetwar, *Mol. Pharmacol.* 5 (2008) 849.
- [3] K.W. Ng, D.T. Leong, D.W. Huttmacher, *Tissue Eng.* 11 (2005) 182.
- [4] K.A. Beningo, M. Dembo, Y.L. Wang, *Proc. Natl. Acad. Sci. U. S. A.* 101 (2004) 18024.
- [5] F. Wang, V.M. Weaver, O.W. Petersen, C.A. Larabell, S. Dedhar, P. Briand, R. Lupu, M.J. Bissell, *Proc. Natl. Acad. Sci. U. S. A.* 95 (1998) 14821.
- [6] B. Knight, C. Laukaitis, N. Akhtar, N.A. Hotchin, M. Edlund, A.R. Horwitz, *Curr. Biol.* 10 (2000) 576.
- [7] C.D. Roskelley, P.Y. Desprez, M.J. Bissell, *Proc. Natl. Acad. Sci. U. S. A.* 91 (1994) 12378.
- [8] N.P. Rhodes, J.K. Srivastava, R.F. Smith, C. Longinotti, *J. Mater. Sci., Mater. Med.* 15 (2004) 391.
- [9] X. Zhang, W. Wang, W. Yu, Y. Xie, Y. Zhang, X. Ma, *Biotechnol. Prog.* 21 (2005) 1289.
- [10] M.A. Pattison, S. Wurster, T.J. Webster, K.M. Haberstroh, *Biomaterials* 26 (2005) 2491.
- [11] M.M. Stevens, J.H. George, *Science* 310 (2005) 1135.
- [12] M. Esguerra, H. Fink, M.W. Laschke, A. Jeppsson, D. Delbro, P. Gatenholm, M.D. Menger, B. Risberg, *J. Biomed. Mater. Res., A* (2009).
- [13] G. Helenius, H. Backdahl, A. Bodin, U. Nannmark, P. Gatenholm, B. Risberg, *J. Biomed. Mater. Res., A* 76 (2006) 431.
- [14] A. Svensson, E. Nicklasson, T. Hara, B. Panilaitis, D.L. Kaplan, M. Brittberg, P. Gatenholm, *Biomaterials* 26 (2005) 419.
- [15] H. Backdahl, G. Helenius, A. Bodin, U. Nannmark, B.R. Johansson, B. Risberg, P. Gatenholm, *Biomaterials* 27 (2006) 2141.
- [16] H. Backdahl, M. Esguerra, D. Delbro, B. Risberg, P. Gatenholm, *J. Tissue Eng. Regen. Med.* 2 (2008) 320.
- [17] C. Li, C. Vepari, H.J. Jin, H.J. Kim, D.L. Kaplan, *Biomaterials* 27 (2006) 3115.
- [18] A. Subramanian, D. Vu, G.F. Larsen, H.Y. Lin, *J. Biomater. Sci., Polym. Ed.* 16 (2005) 861.
- [19] S.A. Riboldi, M. Sampaioles, P. Neuenschwander, G. Cossu, S. Mantero, *Biomaterials* 26 (2005) 4606.
- [20] S.J. Lee, J. Liu, S.H. Oh, S. Soker, A. Atala, J.J. Yoo, *Biomaterials* 29 (2008) 2891.
- [21] M. Sokolsky-Papkov, K. Agashi, A. Olaye, K. Shakesheff, A.J. Domb, *Adv. Drug Deliv. Rev.* 59 (2007) 187.
- [22] H. Yoshimoto, Y.M. Shin, H. Terai, J.P. Vacanti, *Biomaterials* 24 (2003) 2077.
- [23] W.J. Li, R. Tuli, X. Huang, P. Laquerriere, R.S. Tuan, *Biomaterials* 26 (2005) 5158.
- [24] M. Shin, H. Yoshimoto, J.P. Vacanti, *Tissue Eng.* 10 (2004) 33.
- [25] S. Li, P. Dobrzynski, J. Kasperczyk, M. Bero, C. Braud, M. Vert, *Biomacromolecules* 6 (2005) 489.
- [26] S. Zhong, W.E. Teo, X. Zhu, R.W. Beuerman, S. Ramakrishna, L.Y. Yung, *J. Biomed. Mater. Res., A* 79 (2006) 456.
- [27] J.A. Matthews, G.E. Wnek, D.G. Simpson, G.L. Bowlin, *Biomacromolecules* 3 (2002) 232.
- [28] R.D. Sumanasinghe, S.H. Bernacki, E.G. Lobo, *Tissue Eng.* 12 (2006) 3459.
- [29] V. Karageorgiou, D. Kaplan, *Biomaterials* 26 (2005) 5474.
- [30] G.N. Naumov, L.A. Akslen, J. Folkman, *Cell Cycle* 5 (2006) 1779.
- [31] A. Bodin, L. Ahrenstedt, H. Fink, H. Brumer, B. Risberg, P. Gatenholm, *Biomacromolecules* 8 (2007) 3697.
- [32] Y. Zhang, H. Ouyang, C.T. Lim, S. Ramakrishna, Z.M. Huang, *J. Biomed. Mater. Res., B. Appl. Biomater.* 72 (2005) 156.
- [33] J. Nam, Y. Huang, S. Agarwal, J. Lannutti, *Tissue Eng.* 13 (2007) 2249.



3D *in vitro* bioengineered tumors based on collagen I hydrogels

Christopher S. Szot*, Cara F. Buchanan, Joseph W. Freeman, Marissa N. Rylander

School of Biomedical Engineering and Sciences, Virginia Tech-Wake Forest University, Blacksburg, VA 24061, USA

ARTICLE INFO

Article history:

Received 3 June 2011

Accepted 1 July 2011

Available online 22 July 2011

Keywords:

Collagen I

Hydrogel

Three-dimensional

Tumor microenvironment

Hypoxia

ABSTRACT

Cells cultured within a three-dimensional (3D) *in vitro* environment have the ability to acquire phenotypes and respond to stimuli analogous to *in vivo* biological systems. This approach has been utilized in tissue engineering and can also be applied to the development of a physiologically relevant *in vitro* tumor model. In this study, collagen I hydrogels cultured with MDA-MB-231 human breast cancer cells were bioengineered as a platform for *in vitro* solid tumor development. The cell–cell and cell–matrix interactions present during *in vivo* tissue progression were encouraged within the 3D hydrogel architecture, and the biocompatibility of collagen I supported unconfined cellular proliferation. The development of necrosis beyond a depth of ~150–200 μm and the expression of hypoxia-inducible factor (HIF)-1 α were demonstrated in the *in vitro* bioengineered tumors. Oxygen and nutrient diffusion limitations through the collagen I matrix as well as competition for available nutrients resulted in growing levels of intracellular hypoxia, quantified by a statistically significant ($p < 0.01$) upregulation of HIF-1 α gene expression. The bioengineered tumors also demonstrated promising angiogenic potential with a statistically significant ($p < 0.001$) upregulation of vascular endothelial growth factor (VEGF)-A gene expression. In addition, comparable gene expression analysis demonstrated a statistically significant increase of HIF-1 α ($p < 0.05$) and VEGF-A ($p < 0.001$) by MDA-MB-231 cells cultured in the 3D collagen I hydrogels compared to cells cultured in a monolayer on two-dimensional tissue culture polystyrene. The results presented in this study demonstrate the capacity of collagen I hydrogels to facilitate the development of 3D *in vitro* bioengineered tumors that are representative of the pre-vascularized stages of *in vivo* solid tumor progression.

© 2011 Elsevier Ltd. All rights reserved.

1. Introduction

Cancer biologists, biomedical researchers, and oncologists have long relied on two-dimensional (2D) Petri dish studies and small animal models to study the complex tumorigenic mechanisms of angiogenesis, invasion, and metastasis. However, these models of tumor development have thus far been inadequate for cultivating the discovery of definitive cancer termination and prevention treatments. 2D cell culture models lack the structural architecture necessary for proper cell–cell and cell–matrix interactions and are therefore incapable of replicating an *in vivo* phenotype [1–5]. Small animal models are the current gold standard for conducting cancer research, even though there are considerable differences between cancer progression in humans and animals [3,6]. Additionally, animals intrinsically contain many uncontrollable factors, including host cells, an immune response, hemodynamics, and endogenous growth factors. These variables complicate isolating the impact of

specific stimuli, such as cellular, chemical, and mechanical cues, during therapeutic testing [7]. Recently, some promising three-dimensional (3D) cell culture models have been developed for studying tumor progression *in vitro*. Results in the literature show that these models are beginning to restore the cellular morphologies and phenotypes seen during *in vivo* tumor development [8–13].

Ghajar and Bissell recently defined Tumor Engineering as “the construction of complex culture models that recapitulate aspects of the *in vivo* tumor microenvironment to study the dynamics of tumor development, progression, and therapy on multiple scales [14].” This burgeoning field of research is rapidly evolving the study of cancer progression *in vitro* [5,15]. Fischbach and colleagues have engineered an array of 3D *in vitro* tumor models using both synthetic and natural polymeric scaffolds to demonstrate angiogenic factor secretion and drug responsiveness [8], the effects of tumor oxygen tension and 3D cell–extracellular matrix (ECM) interactions on angiogenic potential [12], and endothelial cell remodeling of dense collagen I matrices in response to potential secretion of angiogenic factors from underlying cancer cells [9]. Nelson and Bissell have highlighted the importance of developing

* Corresponding author. Tel.: +1 540 231 0636; fax: +1 540 231 9738.
E-mail address: szotc@vt.edu (C.S. Szot).

functional 3D *in vitro* models of mammary gland acini for advancing breast cancer research [10] and have fabricated 3D epithelial culture models using lithography [11]. Our group has reported previously on the potential use of nanofibrous scaffolds, such as bacterial cellulose and electrospun polymer composites, for tissue engineering *in vitro* tumor models [16].

The pre-vascularized stages of solid tumor growth can be characterized by identifiable criteria within the tumor microenvironment, including an uninhibited 3D proliferative capacity [17], regions of hypoxia surrounding a necrotic core [18,19], and activation of genetic factors that lead to the recruitment of local endothelial cells for self-sustaining angiogenesis (Fig. 1a) [17,20]. Uninhibited 3D proliferative capacity is a trait that cancer cells achieve during *in vivo* tumor development following a series of mutations that cause growth signal autonomy, insensitivity to antigrowth signals, and resistance to apoptosis [17]. Cancer cell lines *in vitro* maintain this phenotype, demonstrating limitless proliferation within the confines of their environment. Culturing cancer cells in 3D scaffolds has been shown to foster this proliferative potential, allowing for growth of clinically relevant tumor masses [8]. However, within an *in vivo* tumor microenvironment, there are restrictions on tumor growth enforced by oxygen and nutrient diffusion limitations through tissue. Hypoxia, a state of limited oxygen availability, occurs within 100–200 μm of the closest vasculature. Cancer cells that cannot adjust to the oxygen and nutrient deficiencies at the core of a growing tumor mass cede to cell death through either apoptosis or necrosis. A key marker for identifying hypoxia is hypoxia-inducible factor (HIF)-1 α , a heterodimeric transcription factor protected from degradation when the surrounding oxygen tension is at a hypoxic level [18,19]. Solid tumors evolve from an avascular to a vascular state by responding

to this microenvironmental hypoxic stress and initiating an angiogenic response from the host vasculature. This process is instigated by the cancer cells, which secrete growth factors and cytokines that interact with local endothelial cells, promoting vascular sprouting and neovascularization [21]. Vascular endothelial growth factor A (VEGF-A), a heparin-binding homodimeric glycoprotein, plays a major role in initiating this process through stimulating vascular permeability and endothelial growth [22]. Activation of VEGF-A gene transcription occurs in direct response to the development of hypoxia and HIF-1 α expression [23].

The biocompatibility and 3D architecture of collagen I hydrogels are suitable properties for reproducing the microenvironmental conditions of a solid tumor. Collagen I is a frequently used substrate for cell culture and tissue engineering applications, because it contains the tripeptide RGD (Arg-Gly-Asp), a short amino acid sequence that preferentially binds to receptors on cell surfaces [24]. Cell-mediated degradation of collagen I through the secretion of cleaving enzymes allows for remodeling of the matrix during proliferation, migration, and infiltration [25]. Furthermore, hydrogel concentration, scaffold thickness, and cell seeding density can be tailored to stimulate specific cellular responses within the engineered microenvironment. We hypothesize that collagen I hydrogels can be used as 3D cell culture scaffolds for bioengineering tumors that mimic key characteristics of *in vivo* tumor progression.

While the influence of hypoxic oxygen levels and cell-matrix interactions on the angiogenic potential of cancer cells cultured *in vitro* has been documented [12], a 3D *in vitro* tumor microenvironment that inherently promotes a phenotype typical of the pre-vascularized stages of *in vivo* solid tumor progression has not been established. In this study, MDA-MB-231 human breast cancer cells

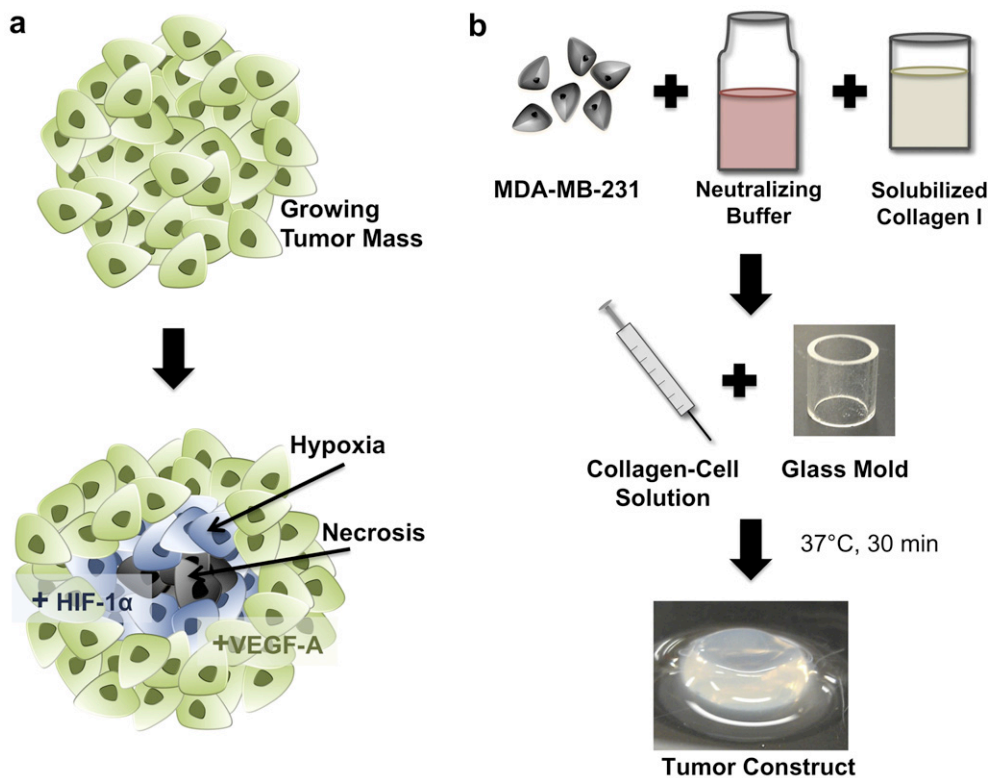


Fig. 1. (a) The pre-vascularized stages of *in vivo* solid tumor development can be characterized by identifiable criteria within the tumor microenvironment, including an uninhibited 3D proliferative capacity, regions of hypoxia surrounding a necrotic core, and activation of angiogenic growth factors, including VEGF-A. (b) Collagen I hydrogels cultured with MDA-MB-231 human breast cancer cells were bioengineered as a platform for *in vitro* solid tumor development.

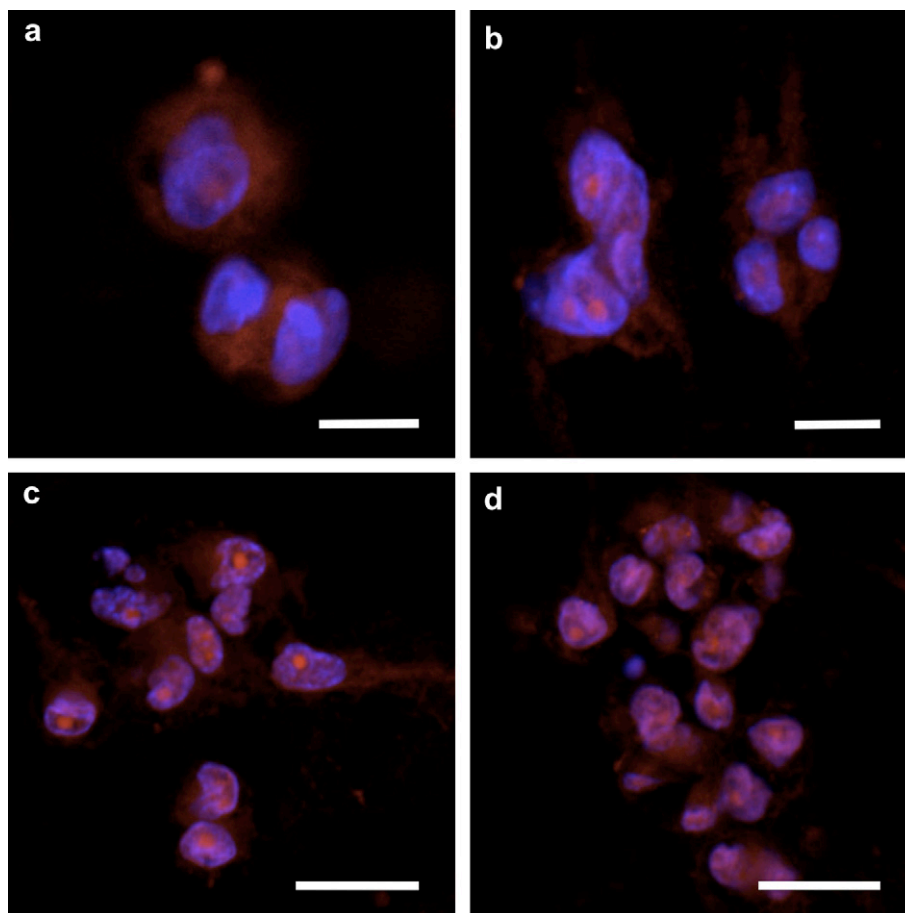


Fig. 2. MDA-MB-231 cells were cultured in collagen I hydrogels for 1, 3, 5, and 7 days (a–d, respectively), exhibiting the typical cell–matrix and cell–cell interactions observed *in vivo*. Cells developed an elongated morphology over 7 days with visible processes, demonstrating cell–matrix interactions. As the cells began to proliferate, they aggregated into 3D clusters, demonstrating cell–cell interactions. Scale bars are (a, b) 10 μm and (c, d) 20 μm .

were cultured in collagen I hydrogel scaffolds, and the cell–cell and cell–matrix interactions present during *in vivo* development were demonstrated. Culturing conditions, including cell seeding density and scaffold thickness, were varied to control oxygen and nutrient availability and diffusion limitations for the purpose of encouraging the development of necrosis and hypoxia. These phenotypical changes were confirmed through real-time fluorescent imaging,

immunofluorescence staining, and gene expression analysis. The bioengineered tumors exhibited considerable angiogenic potential, with a statistically significant upregulation of VEGF-A gene expression in response to the growing levels of intra-cellular hypoxia. The results from this study support the development of 3D *in vitro* bioengineered tumors that are representative of *in vivo* tumor progression.

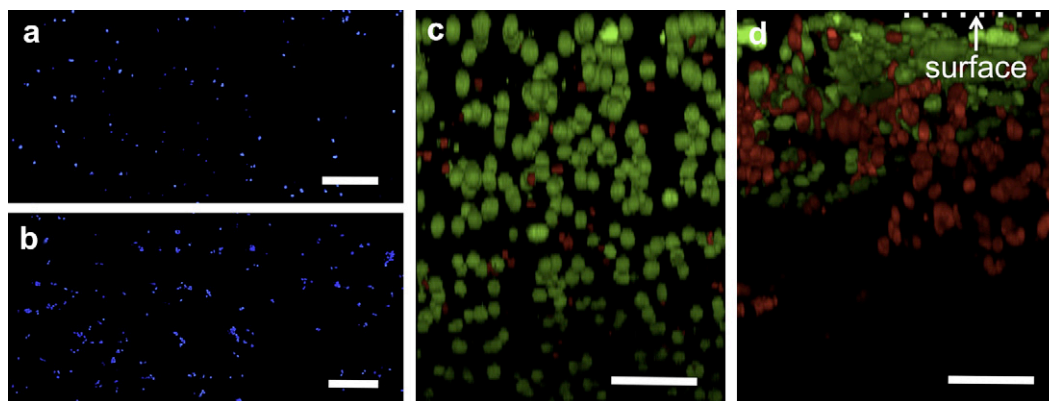


Fig. 3. (a) MDA-MB-231 cells were seeded at a density of 1 million cells/ml, and on day 1, the cells were evenly distributed throughout the entire hydrogel. (b) Noticeable proliferation was observed on day 5, with cell proliferation leading to the formation of cell clusters. (c) The initial cell seeding density was increased to 4 million cells/ml, and on day 1, the viable cells (green) were evenly distributed with only a few dead cells (red) present at non-specific degrees of depth. (d) On day 5, cells were viable through ~ 150 – 200 μm of depth below the surface, with limitations in oxygen and nutrients leading to cell death towards the core of the bioengineered tumors. Scale bars are (a, b) 250 μm and (c, d) 100 μm . (For interpretation of the references to colour in this figure legend, the reader is referred to the web version of this article.)

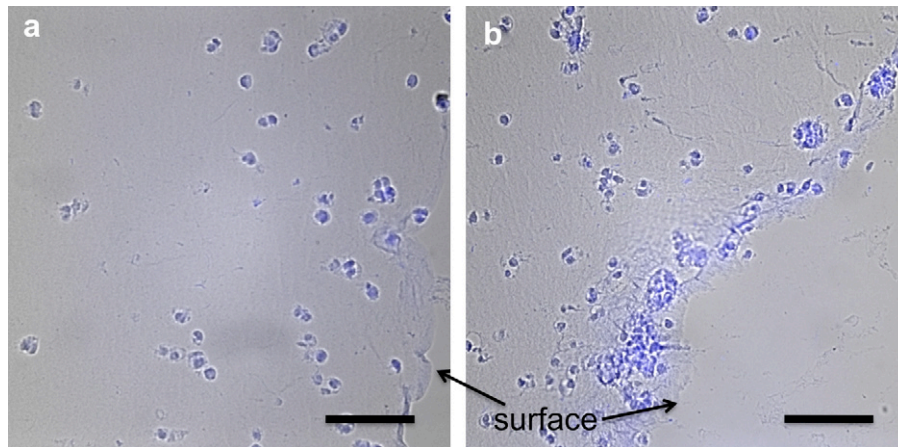


Fig. 4. Hypoxia was detected using immunofluorescence for HIF-1 α . (a) MDA-MB-231 cells were seeded at a density of 4 million cells/ml, and on day 1, the blue fluorescence indicated intra-cellular levels of hypoxia. (b) On day 5, the fluorescence intensity increased, in particular within the large cell clusters, signifying an increase in hypoxic oxygen levels. Scale bar is 100 μ m. (For interpretation of the references to colour in this figure legend, the reader is referred to the web version of this article.)

2. Materials and methods

2.1. Cell culture

The MDA-MB-231 human breast cancer cell line was used in all experiments (American Type Culture Collection, Manassas, VA, USA). MDA-MB-231 cells were cultured in GIBCO[®] DMEM/F12 (1:1) +L-Glutamine, +15 mM HEPES (Invitrogen, Carlsbad, CA, USA) and supplemented with 10% fetal bovine serum (Sigma Aldrich, St. Louis, MO, USA) and 1% Penicillin/Streptomycin (Invitrogen). Cell cultures were incubated in a humidified atmosphere of 95% air and 5% CO₂ at a constant temperature of 37 °C. Cell passages of 10–18 were used for all experiments.

2.2. Collagen I Hydrogels

Collagen I was removed from rat tail tendons and prepared as a solid hydrogel to facilitate 3D cell culture. Tendons were excised from the tails of Sprague Dawley rats and allowed to dissolve in 40 ml of 10 mM HCl per gram of tendon under agitation overnight at room temperature. The resulting suspension was centrifuged at 30,000 g for 30 min at 4 °C. The supernatant, containing the collagen I, was decanted and the pellet was discarded. The concentration of collagen I was obtained by evaporating out the solvent from 0.25, 0.5, and 1.0 ml samples in a 110 °C oven for 2 h, measuring the dry weights, and averaging the concentration values. In order to sterilize the collagen I for cell culture, chloroform (10% of the volume of collagen) was layered beneath the collagen I solution and allowed to rest for 24 h at 4 °C (Sigma Aldrich protocol).

The volume of collagen I necessary for obtaining a target final concentration of 8 mg/ml was neutralized with a buffer containing 10 \times concentrated DMEM (supplemented with 4.5 g/L glucose, L-glutamine, sodium pyruvate, and sodium bicarbonate; Mediatech, Inc., Manassas, VA, USA), 1N NaOH, and dH₂O. In order to initiate collagen I gelation, the ratio of components in the neutralizing buffer was calculated using the following equations: (1) 10 \times DMEM = Final Volume \times 0.1, (2) 1N NaOH = Volume of Collagen I \times 0.02, and (3) dH₂O = Final Volume – Volume of Collagen I – 10 \times DMEM – 1N NaOH. MDA-MB-231 cells were first suspended in the neutralizing buffer and then mixed with the collagen I solution at the desired final seeding density (Fig. 1b). The collagen-cell suspension was pipetted into 8 mm diameter cylindrical glass molds and allowed to gel in an incubator at 37 °C for 30 min. The volume of the collagen-cell suspension (75 and 150 μ l) was varied to fabricate specific levels of hydrogel thickness (1.5 and 3 mm, respectively). The cancer cell seeded hydrogels were removed from the molds and cultured in cell culture media, as described above, for 0, 1, 3, 5, and 7 days.

2.3. Immunofluorescence staining

The bioengineered tumors were fixed in 10% formalin for 24 h at room temperature and then stored in 70% ethanol (EtOH) for no longer than 7 days at 4 °C. Next, the tumors were dehydrated through a series of EtOH incubations (70, 80, 90, 95, 95, 100, 100%) at 37 °C and then moved to xylene for 1 h at room temperature. A series of two 1 h melted paraffin wax (Tissue Prep, Fischer Scientific, Pittsburgh, PA, USA) incubations at 60 °C were used to embed the bioengineered tumors, and the wax blocks were allowed to solidify overnight at 4 °C. A Microm HM 355S microtome (Thermo Scientific, Kalamazoo, MI, USA) was used to obtain 15 μ m thick sections. Paraffin was removed from the slides using a pair of xylene washes followed by a series of EtOH washes (100, 100, 95, 95, 80%) to re-hydrate the tumor sections. All images shown are representative of the entire bioengineered tumor.

2.3.1. 3D Morphological Analysis

Cell morphology was analyzed as described previously [16]. Briefly, bioengineered tumor sections were permeabilized using 0.5% Triton X-100 (Sigma Aldrich), and 1% BSA (Santa Cruz Biotechnology Inc., Santa Cruz, CA, USA) was used as a blocking buffer for 30 min at 37 °C. Cells were stained for 20 min at room temperature with rhodamine phalloidin (Invitrogen), a high-affinity probe for F-actin, and sections were mounted with VECTASHIELD[®] mounting medium with DAPI (Vector Laboratories, Burlingame, CA, USA), to visualize nuclei. Imaging was performed using a Zeiss LSM 510 laser scanning confocal microscope (Carl Zeiss, Thornwood, NY, USA).

2.3.2. Cell proliferation and necrosis

Cell proliferation was qualitatively observed using a DAPI stain for nuclei, as described above. A Leica DMI 6000 fluorescent microscope (Leica Microsystems Inc., Buffalo Grove, IL, USA) was used to tile a set of images and reconstruct entire cross sections of the bioengineered tumors. Representative \sim 2 mm² regions of interest are shown. The development of necrosis and the depth at which this occurred was analyzed using a laser scanning confocal microscope (Zeiss LSM 510) to perform a Z-stack through a “live” bioengineered tumor in real-time. Image slices were taken at intervals of 5–10 μ m to a depth of \sim 400 μ m. Prior to imaging, the bioengineered tumors were incubated for 45 min in cell culture media containing 4 μ M calcein AM (λ_{em} = 515 nm, Invitrogen) to stain viable cells. 1.5 mM propidium iodide (λ_{em} = 617 nm, Invitrogen) was added to the cell culture media for the last 5 min of the calcein AM incubation to stain dead cells. The bioengineered tumors were washed with PBS before imaging.

2.3.3. Hypoxia

The presence of hypoxia was visualized using a rabbit monoclonal [EP1215Y] to HIF-1 α primary antibody (Abcam Inc., Cambridge, MA, USA) in conjunction with an Alexa Fluor[®] 350 goat anti-rabbit IgG (H + L) secondary antibody (Invitrogen). Bioengineered tumor sections were permeabilized with 0.5% Triton X-100 (Sigma Aldrich) and blocked with 5% goat serum (Santa Cruz Biotechnology Inc.) overnight at 4 °C. Sections were incubated at 37 °C for 2.5 h with the HIF-1 α primary antibody and then for 1 h with the Alexa Fluor[®] 350 secondary antibody, separated by a series of PBS washes. VECTASHIELD[®] mounting medium was used to preserve fluorescence. Sections were imaged with a Leica DMI 6000 fluorescent microscope. The fluorescent images were overlaid on the bright field images.

2.4. Gene expression analysis

The gene expression levels of HIF-1 α and VEGF-A were measured using quantitative reverse transcription polymerase chain reaction (qRT-PCR). Total RNA was first isolated on days 0, 1, 3, 5, and 7 using TRI Reagent[®] Solution (Applied Biosystems/Ambion, Austin, TX, USA). For the 3D cell culture groups, the cells were allowed to remain in culture for 4 h on day 0 before RNA isolation was performed. For the 2D cell culture group, the cells were allowed to remain in culture for 8 h to ensure complete cell attachment before RNA isolation was performed. Next, 1 μ g of total RNA was reverse-transcribed to cDNA using a Reverse Transcription System (Promega, Madison, WI, USA). Lastly, an ABI 7300 Sequence Detection System (Applied Biosystems, Carlsbad, CA, USA) was used to conduct qRT-PCR using TaqMan[®] Universal PCR Master Mix and gene-specific TaqMan[®] PCR primers (Applied Biosystems): HIF-1 α (NM_001530.3), VEGF-A (NM_001025366.2), and GAPDH (NM_002046.3). Gene expression was normalized to GAPDH using the comparative threshold cycle ($\Delta\Delta$ Ct) method of quantification [26]. The data is

presented as a relative fold induction, calculated as $2^{-\Delta\Delta C_T}$, with gene expression on day 0 used as the control group in Fig. 5 and gene expression for 2D cell culture used as the control group in Fig. 6. All experiments were performed with an $n = 4$.

2.5. Statistical Analysis

Gene expression levels measured by qRT-PCR were analyzed for significance using an ANOVA test with a Tukey post hoc test. $p < 0.05$ was considered significant, and $p < 0.01$ and $p < 0.001$ were also noted.

3. Results

3.1. Cell morphology in 3D collagen I hydrogels

MDA-MB-231 cells were cultured in 3D collagen I hydrogels for 1, 3, 5, and 7 days (Fig. 2a–d, respectively). The cells developed a stellate, elongated morphology with disorganized nuclei and invasive processes by day 3, demonstrating cell–matrix interactions

(Fig. 2b). By day 5, as the cells began to proliferate throughout the hydrogel, they aggregated into clusters, demonstrating cell–cell interactions (Fig. 2c). These cell–matrix and cell–cell interactions are representative of *in vivo* biological systems and have been classified previously [27].

3.2. Cell proliferation and the progression towards cell death

Proliferation of MDA-MB-231 cells, seeded at a density of 1 million cells/ml in 3 mm thick collagen I hydrogels, was qualitatively observed using a DAPI stain. Representative $\sim 2 \text{ mm}^2$ regions of interest are shown from the bioengineered tumor cross sections. On day 1, the cells appear to be evenly distributed throughout the entire volume of the hydrogel (Fig. 3a). A noticeable increase in cell number was visible from day 1 to day 5, with numerous cell clusters forming by day 5 (Fig. 3b). On day 5, the cell clusters were evenly

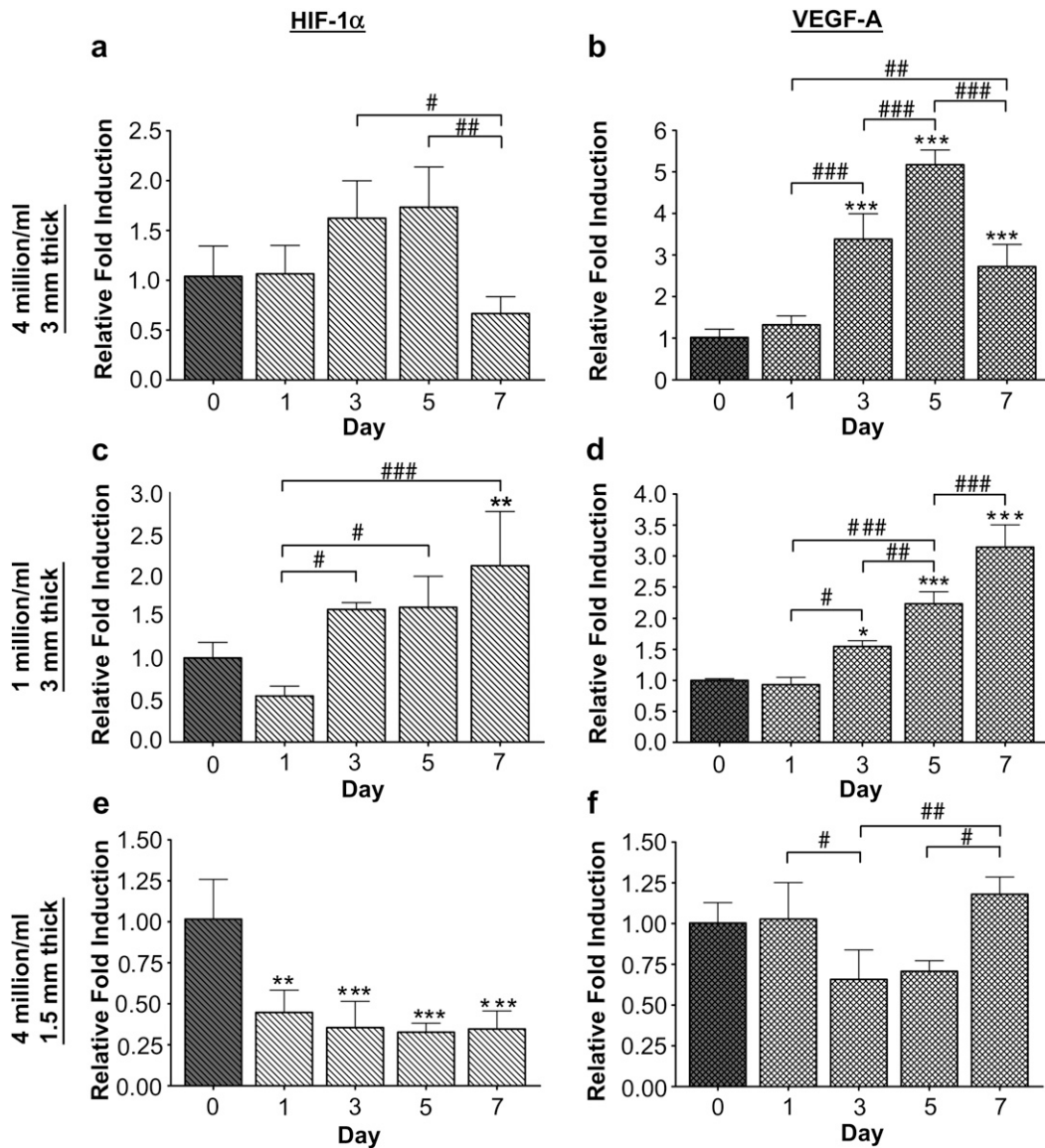


Fig. 5. Quantitative RT-PCR was used to analyze the progression of HIF-1 α and VEGF-A gene expression in the bioengineered tumors over a 7-day period, with expression on day 0 used as the control. (a, b) Similar to when both necrosis and hypoxia were observed, MDA-MB-231 cells were seeded at a density of 4 million cells/ml in 3 mm thick hydrogels. HIF-1 α was upregulated on day 3 and day 5, and VEGF-A was significantly upregulated on days 3, 5, and 7. (c, d) When the initial cell seeding density was decreased to 1 million cells/ml, HIF-1 α was significantly upregulated on day 7, and VEGF-A was significantly upregulated on days 3, 5, and 7. (e, f) When the cell seeding density was kept at 4 million cells/ml but a 1.5 mm thick hydrogel was used, neither HIF-1 α nor VEGF-A were upregulated over the 7-day period. * was used to indicate significance compared to day 0. #, **/###, and ***/### denote $p < 0.05$, 0.01, and 0.001, respectively.

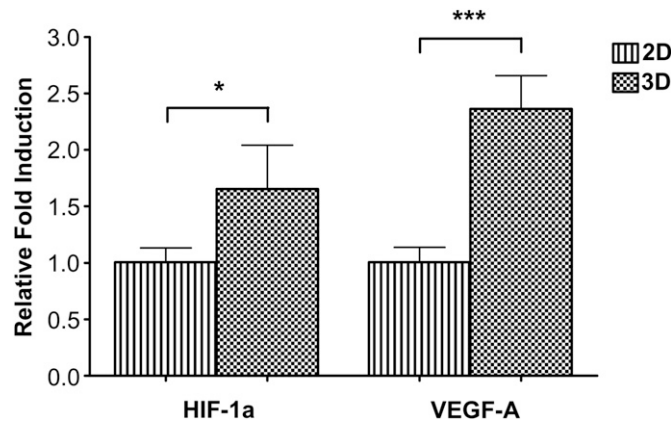


Fig. 6. HIF-1 α and VEGF-A gene expression were significantly upregulated when MDA-MB-231 cells were cultured in 3D collagen I hydrogels as compared to cells cultured in a monolayer on 2D tissue culture polystyrene. Gene expression was compared on day 0 to determine the specific effect of 3D culture without the contribution of cell proliferation or the development of hypoxia. * and *** denote $p < 0.05$ and 0.001 , respectively.

distributed, similar to the individual cells on day 1, suggesting that they formed as a result of cell proliferation rather than cell migration.

In an effort to induce necrosis at the core of the bioengineered tumors, MDA-MB-231 cells were seeded at a higher density of 4 million cells/ml in 3 mm thick collagen I hydrogels. On day 1, viable cells were visible and evenly distributed throughout the entire 400- μ m segment with only a small number of dead cells present at non-specific degrees of depth (Fig. 3c). However, on day 5, viable cells were only visible until a depth of ~150–200 μ m from the bioengineered tumor surface (Fig. 3d). Beyond this level, a large number of dead cells were present followed by a large void with no visible cells. Cell death was attributed to limitations in oxygen and nutrient diffusion through the collagen I matrix and an increase in consumption of the available nutrients. One explanation for the cellular void at the core of the bioengineered tumors is that since propidium iodide is a nuclear stain, the nuclear DNA degraded in the dead cells closest to the center [28]. Another possibility is that the cells migrated to the outer periphery of the bioengineered tumors towards the more prevalent supply of oxygen and nutrients.

3.3. Growing levels of hypoxia in the bioengineered tumors

The onset of tumor necrosis is a direct result of limited oxygen and nutrient availability [18,19]. Therefore, hypoxia is a viable precursor of cell death. To demonstrate this correlation, MDA-MB-231 cells were seeded at a density of 4 million cells/ml in 3 mm thick hydrogels, similar to the experiment used to induce necrosis. Intra-cellular levels of hypoxia were qualitatively observed through immunofluorescence imaging of HIF-1 α protein. HIF-1 α was visible on day 1 (Fig. 4a) with an increase in intensity seen on day 5 (Fig. 4b). The presence of HIF-1 α on day 1 demonstrates the initial hypoxic cellular response to being cultured in 3D. It is expected that cells will have greater difficulty in obtaining oxygen and nutrients when confined within a 3D matrix as opposed to being cultured in a monolayer where they are in direct contact with oxygenated media. The increase in HIF-1 α intensity observed on day 5 was attributed to cell proliferation and the resulting increase in competition for available oxygen and nutrients. This was evident in the large clusters of cells, which exhibited the greatest magnitude of intensity, signifying an augmented degree of intra-cellular hypoxia [22].

3.4. Bioengineered tumor hypoxic and angiogenic gene expression profile

In order to demonstrate an intrinsically induced upregulation of HIF-1 α and VEGF-A gene expression in correlation with bioengineered tumor maturation, we varied scaffold thickness and cell seeding density to alter specific microenvironmental parameters including oxygen and nutrient diffusion and competition for available nutrients. Three culturing configurations were used: 4 million cells/ml seeded in 3 mm thick hydrogels (Fig. 5a and b), 1 million cells/ml seeded in 3 mm thick hydrogels (Fig. 5c and d), and 4 million cells/ml seeded in 1.5 mm thick hydrogels (Fig. 5e and f).

When 4 million cells/ml were seeded in the thicker, 3 mm hydrogels, HIF-1 α expression was upregulated on day 3 and day 5 (Fig. 5a). Although this upregulation was not statistically significant compared to day 0, immunofluorescence staining (Fig. 4) demonstrated an initial presence of HIF-1 α protein on day 1 with an increase in intensity on day 5. The statistically significant ($p < 0.01$) decrease in HIF-1 α gene expression on day 7 is hypothesized to be a result of the hypoxic cells dying from a lack of oxygen and nutrients. VEGF-A expression was statistically upregulated ($p < 0.001$) on days 3, 5, and 7 compared to day 0 (Fig. 5b). Between day 3 and day 5, VEGF-A expression was further significantly upregulated ($p < 0.001$), whereas between day 5 and day 7, VEGF-A expression was significantly downregulated ($p < 0.001$). However, day 7 VEGF-A expression was still significantly higher compared to day 0. Since HIF-1 α expression leads to activation of VEGF-A gene transcription [23], this decrease in VEGF-A expression from day 5 to day 7 was likely due to the downregulation in HIF-1 α expression seen on day 7.

When the cell seeding density was reduced to 1 million cells/ml in the 3 mm thick hydrogels, the competition for available oxygen and nutrients decreased, resulting in an initial downregulation of HIF-1 α expression (Fig. 5c) and a delayed upregulation of VEGF-A expression (Fig. 5d), compared to when 4 million cells/ml were seeded in the same scaffold thickness. HIF-1 α expression was significantly upregulated ($p < 0.05$) on day 3 and day 5 compared to day 1 and significantly upregulated ($p < 0.01$) on day 7 compared to day 0. VEGF-A expression was significantly upregulated on day 3 ($p < 0.05$) and days 5 and 7 ($p < 0.001$) compared to day 0. Between day 3 and day 5 and between day 5 and day 7, VEGF-A expression was further significantly upregulated ($p < 0.01$ and $p < 0.001$, respectively). When comparing data from the high (4 million cells/ml) and low (1 million cells/ml) cell seeding densities in 3 mm thick bioengineered tumors, it can be concluded that HIF-1 α and VEGF-A gene expression upregulation peaked at day 5 when a high seeding density was used as a result of oxygen and nutrient deficiency-induced cell death after day 5 (Fig. 5a and b). However, with a lower seeding density, a consistent upregulation is present over the 7-day period, indicative of cell proliferation-sustained hypoxic stresses (Fig. 5c and d).

Decreasing the scaffold thickness to 1.5 mm mitigated the oxygen and nutrient diffusion limitations. Under these culturing conditions, neither HIF-1 α nor VEGF-A expression were upregulated on any day compared to day 0 (Fig. 5e and f). HIF-1 α expression was significantly downregulated ($p < 0.01$) on day 1 and maintained that level through day 7. As mentioned previously, since HIF-1 α expression is known to activate VEGF-A gene transcription [23], no significant upregulation in VEGF-A expression compared to day 0 was expected. An increase in intra-cellular hypoxic levels is expected when cells are first confined in a 3D matrix on day 0. Therefore, the significant downregulation in HIF-1 α expression seen on day 1 implies that the cells had migrated to the periphery of the bioengineered tumors to obtain more oxygen.

3.5. 2D versus 3D cell culture: comparison of hypoxic and angiogenic gene expression

Comparable gene expression analysis between cells cultured in a 2D monolayer versus in a 3D hydrogel was performed to emphasize the importance and relevance of using 3D cell culture models. Fig. 6 demonstrates a statistically significant upregulation of HIF-1 α ($p < 0.05$) and VEGF-A ($p < 0.001$) gene expression when MDA-MB-231 cells were cultured in the 3D collagen I hydrogels compared to a 2D 6-well cell culture dish. Since HIF-1 α and VEGF-A expression were shown to change over time due to microenvironmental conditions (Fig. 5), gene expression was compared on day 0 to determine the specific effect of 3D cell culture on the phenotypic changes. This initial upregulation of HIF-1 α gene expression in the 3D bioengineered tumors is consistent with the presence of HIF-1 α protein on day 1 (Fig. 4a) and supports the cell migration-mediated downregulation of HIF-1 α gene expression observed in the thinner scaffolds on day 1 (Fig. 5e).

4. Discussion

The development and utilization of 3D *in vitro* cell culture models for studying the complex mechanisms of tumorigenesis are beginning to play a major role in advancing fundamental cancer research as well as the testing and discovery of several different treatment modalities. The field of tissue engineering offers a promising approach for fabricating “functional” *in vitro* tumor models that are representative of *in vivo* tumor progression. Similar to tissue engineering an organ or tissue replacement, cells are grown on 3D polymeric scaffolds in an *in vitro* environment that induces upregulation of characteristic genetic markers, HIF-1 α and VEGF-A in this study, to promote an *in vivo* phenotype. Our previous work has investigated electrospun polycaprolactone/collagen I composites as a scaffold for *in vitro* tumor development [16]. While the electrospun scaffolds demonstrated favorable cell adhesion, viability, and proliferation, the fibers were too compact to allow for significant cell infiltration and 3D growth. Other attempts by our group have involved the fabrication of 3D electrospun poly(L-lactic acid)/polyethylene oxide (PEO) composite scaffolds where the PEO was leached out, leaving large pores for cell infiltration [29]. Although significant cell infiltration and 3D growth was achieved over several weeks, the development of intra-cellular levels of hypoxia was not observed.

In the present study, collagen I hydrogel scaffolds facilitated immediate 3D cell growth, allowing for the development of necrotic and hypoxic cellular regions. A collagen I concentration of 8 mg/ml was chosen based on mechanical characterization data from the literature [30]. Paszek et al. measured the elastic moduli of established tumors grown in transgenic mice as well as hydrogels containing 2 and 4 mg/ml collagen I, with values reported of 4.05 ± 0.94 kPa, 0.328 ± 0.09 kPa, and 1.59 ± 0.38 kPa, respectively. We expect an 8 mg/ml collagen I hydrogel to have an elastic modulus that falls within the range of the established tumor models. Matrix stiffness is an important microenvironmental parameter, because it directly affects cell-matrix interactions, including cell infiltration and matrix remodeling during cell proliferation [31,32]. In addition to controlling stiffness, the concentration of collagen I also determines the diffusivity of the hydrogel matrix [30,33], which is an important factor in the development of hypoxia [19,31,32]. Using a collagen I-based hydrogel promoted ideal cell adhesion, viability, and proliferation. Cells demonstrated visible, invasive processes that interacted with the surrounding matrix, and the cell-mediated degradation of collagen I allowed for uninhibited cell proliferation and the formation of large cell clusters (Figs. 2 and 3a and b). As opposed to

when cells are cultured in 2D, these cell-matrix and cell-cell interactions encourage cell signaling and a phenotype representative of *in vivo* biological systems [1,2].

Analogous to *in vivo* tumor progression, limitations in oxygen and nutrient diffusion through the collagen I matrix as well as increased competition for the available nutrients, led to cell death beyond a depth of ~ 150 – 200 μm from the surface of the bioengineered tumors and an increase in intra-cellular levels of hypoxia (Figs. 3d and 4). The restriction of viable cells to a ~ 150 – 200 μm region below the bioengineered tumor surface is representative of the oxygen diffusion limitations in biological tissue [19] and has been shown previously in collagen I hydrogels [34]. HIF-1 α protein and gene expression analysis were used to determine hypoxia given that the degree of HIF-1 α expression correlates with intra-cellular oxygen levels [22]. Immunofluorescence staining demonstrated expression of HIF-1 α protein on day 1 with a noticeable increase in intensity correlating with cell proliferation on day 5, in culturing conditions using a high cell seeding density (4 million cells/ml, 3 mm thick scaffolds) (Fig. 4). HIF-1 α gene expression was significantly upregulated at the lower cell seeding density (1 million cells/ml, 3 mm thick scaffolds) over the 7-day culturing period (Fig. 5c), though immunofluorescence intensity was only observed to be slightly greater than the background (data not shown). This indicated that while HIF-1 α gene expression was not significantly upregulated over time at the higher cell seeding density, the initial degree of intra-cellular hypoxia was greater than at the lower cell seeding density. Intra-cellular hypoxic levels were also shown to be initially upregulated on day 0 when cells were cultured in 3D as opposed to 2D (Fig. 6a). Our results suggest that this is a consequence of diffusion limitations and competition for the available oxygen and nutrients in the immediate vicinity within the confined 3D collagen I matrix. When a thinner hydrogel scaffold was used (1.5 mm thick), HIF-1 α was significantly downregulated on day 1 (Fig. 5e), implying that the cells were no longer experiencing the same hypoxic oxygen tension as on day 0. We believe this is a result of the cells migrating towards the periphery of the scaffold, where more oxygen was available. Overall, cells cultured in 3D were shown to experience initial intra-cellular levels of hypoxia on day 0, with a larger cell seeding density correlating with a greater degree of hypoxia and an increase in HIF-1 α expression associated with cell proliferation and the aggregation of cells into large clusters.

The developed intrinsic increase in intra-cellular hypoxic oxygen levels led to a statistically significant upregulation of VEGF-A gene expression (Fig. 5B, D), which is a strong indicator of the angiogenic potential of the *in vitro* bioengineered tumors. Achieving a hypoxic microenvironment was important for reproducing the *in vivo* stages of tumor development, specifically the HIF-1 α expression-mediated activation of VEGF-A gene transcription [23]. Our results are representative of this, with a direct correlation between HIF-1 α and VEGF-A expression demonstrated in all gene expression experiments (Figs. 5 and 6). VEGF-A is a crucial factor involved in tumor maturation, acting exclusively on endothelial cells to promote tumor angiogenesis [21,22]. Hence, the significant upregulation of VEGF-A expression induced in the *in vitro* bioengineered tumors points towards the accuracy and relevance of our model. Similar 3D *in vitro* cancer cell culture systems have also shown an upregulation in VEGF-A expression in response to both hypoxic oxygen levels and 3D cell-matrix interactions [12]. These systems, however, relied upon the use of manufactured airflow to reproduce a hypoxic environment, rather than allowing cell proliferation and matrix-imposed limitations in oxygen and nutrient diffusion to foster the development of hypoxic oxygen levels.

Although this bioengineered tumor model is only a simplistic representation of the complex nature of a malignant tumor, several key characteristics of *in vivo* solid tumor development (e.g. necrosis, hypoxia, angiogenic gene upregulation) were reproduced, thus exposing the cells to typical tumor microenvironmental stresses. Therefore, it is believed that the *in vitro* bioengineered tumors will respond to stimuli comparable to an *in vivo* response, allowing this system to be used as a more efficient tool for testing a wide range of treatment modalities over conventional methods [35]. The advantages of using 3D scaffolds over 2D tissue culture polystyrene for obtaining an *in vivo* phenotype are well documented [1–5]. However, small animal models are still the primary vehicles used for determining drug efficacy. One of the main issues with drug testing in animals is that many new drugs have success in animal pre-clinical trials but fail in human clinical trials, wasting significant time and money [36]. This failure stems from significant cellular and genetic differences between humans and animals [6]. In addition, the ethical and humane issues associated with animal trials are a noteworthy concern. Nevertheless, animal models should still be used during pre-clinical trials but in conjunction with 3D cell culture systems. Substantial progress still needs to be made before 3D *in vitro* tumor models can replace the more physiologically complete and familiar small animal models.

Physiologically relevant 3D cell culture models, such as the one developed in this study, have the potential to aid in accelerating more effective and cost efficient drug discovery. The next step in advancing our *in vitro* bioengineered tumors into more complex, “functional” tumor replicates is to incorporate additional cell types, including endothelial and stromal cells, to induce neovessel formation. Engineering an *in vitro* 3D microenvironment in which the malignant, tumorigenic mechanisms of angiogenesis, invasion, and metastasis can mature through a natural progression will yield a cell culture system with greater and more reliable predictive capability than traditional animal models. The pre-vascularized bioengineered tumor model introduced in this study is the first step towards tissue engineering a “functional” cancer model.

5. Conclusion

The results presented in this study demonstrate that collagen I hydrogels can facilitate the pre-vascularized stages of *in vivo* solid tumor development. A phenotype representative of *in vivo* tumor progression was achieved in 3D *in vitro* bioengineered tumors by adjusting specific microenvironmental parameters, including limiting oxygen and nutrient diffusion and increasing competition for available nutrients. As the bioengineered tumors matured, *in vivo*-characteristic regions of necrosis and hypoxia developed. The upregulation of VEGF-A gene expression in response to growing levels of intra-cellular hypoxia was a promising finding that may provide clinical relevance to this 3D *in vitro* bioengineered tumor model.

Acknowledgements

We would like to thank Andrea Martin for generously donating the Sprague Dawley rat tails. We also acknowledge our funding, which was provided by the NSF CAREER Award CBET 0955072 and the NIH/NHLBI R01HL098912.

References

- [1] Kim JB. Three-dimensional tissue culture models in cancer biology. *Semin Cancer Biol* 2005;15(5):365–77.
- [2] Griffith LG, Swartz MA. Capturing complex 3D tissue physiology in vitro. *Nat Rev Mol Cell Biol* 2006;7(3):211–24.
- [3] Yamada KM, Cukierman E. Modeling tissue morphogenesis and cancer in 3D. *Cell* 2007;130(4):601–10.
- [4] Horning JL, Sahoo SK, Vijayaraghavalu S, Dimitrijevic S, Vasir JK, Jain TK, et al. 3-D tumor model for in vitro evaluation of anticancer drugs. *Mol Pharmacol* 2008;5(5):849–62.
- [5] Hutmacher DW, Horch RE, Loessner D, Rizzi S, Sieh S, Reichert JC, et al. Translating tissue engineering technology platforms into cancer research. *J Cell Mol Med* 2009;13(8A):1417–27.
- [6] Rangarajan A, Weinberg RA. Opinion: comparative biology of mouse versus human cells: modelling human cancer in mice. *Nat Rev Cancer* 2003;3(12):952–9.
- [7] Kim JB, Stein R, O'Hare MJ. Three-dimensional in vitro tissue culture models of breast cancer – a review. *Breast Cancer Res Treat* 2004;85(3):281–91.
- [8] Fischbach C, Chen R, Matsumoto T, Schmelzle T, Brugge JS, Polverini PJ, et al. Engineering tumors with 3D scaffolds. *Nat Methods* 2007;4(10):855–60.
- [9] Cross VL, Zheng Y, Won Choi N, Verbridge SS, Sutermaster BA, Bonassar LJ, et al. Dense type I collagen matrices that support cellular remodeling and microfabrication for studies of tumor angiogenesis and vasculogenesis in vitro. *Biomaterials* 2010;31(33):8596–607.
- [10] Nelson CM, Bissell MJ. Modeling dynamic reciprocity: engineering three-dimensional culture models of breast architecture, function, and neoplastic transformation. *Semin Cancer Biol* 2005;15(5):342–52.
- [11] Nelson CM, Inman JL, Bissell MJ. Three-dimensional lithographically defined organotypic tissue arrays for quantitative analysis of morphogenesis and neoplastic progression. *Nat Protoc* 2008;3(4):674–8.
- [12] Verbridge SS, Choi NW, Zheng Y, Brooks DJ, Stroock AD, Fischbach C. Oxygen-controlled three-dimensional cultures to analyze tumor angiogenesis. *Tissue Eng Part A* 2010;16(7):2133–41.
- [13] Raof NA, Raja WK, Castracane J, Xie Y. Bioengineering embryonic stem cell microenvironments for exploring inhibitory effects on metastatic breast cancer cells. *Biomaterials* 2011;32(17):4130–9.
- [14] Ghajar CM, Bissell MJ. Tumor engineering: the other face of tissue engineering. *Tissue Eng Part A* 2010;16(7):2153–6.
- [15] Hutmacher DW, Loessner D, Rizzi S, Kaplan DL, Mooney DJ, Clements JA. Can tissue engineering concepts advance tumor biology research? *Trends Biotechnol* 2010;28(3):125–33.
- [16] Szot CS, Buchanan CF, Gatenholm P, Rylander MN, Freeman JW. Investigation of cancer cell behaviour on nanofibrous scaffolds. *Mater Sci Eng C* 2011;31(1):6.
- [17] Hanahan D, Weinberg RA. The hallmarks of cancer. *Cell* 2000;100(1):57–70.
- [18] Zhou J, Schmid T, Schnitzer S, Brune B. Tumor hypoxia and cancer progression. *Cancer Lett* 2006;237(1):10–21.
- [19] Brahimi-Horn MC, Chiche J, Pouyssegur J. Hypoxia and cancer. *J Mol Med* 2007;85(12):1301–7.
- [20] Kilarski WW, Bikfalvi A. Recent developments in tumor angiogenesis. *Curr Pharm Biotechnol* 2007;8(1):3–9.
- [21] Hayes AJ, Huang WQ, Yu J, Maisonnier PC, Liu A, Kern FG, et al. Expression and function of angiopoietin-1 in breast cancer. *Br J Cancer* 2000;83(9):1154–60.
- [22] Bos R, van Diest PJ, de Jong JS, van der Groep P, van der Valk P, van der Wall E. Hypoxia-inducible factor-1 α is associated with angiogenesis, and expression of bFGF, PDGF-BB, and EGFR in invasive breast cancer. *Histopathology* 2005;46(1):31–6.
- [23] Bos R, Zhong H, Hanrahan CF, Mommers EC, Semenza GL, Pinedo HM, et al. Levels of hypoxia-inducible factor-1 α during breast carcinogenesis. *J Natl Cancer Inst* 2001;93(4):309–14.
- [24] Saltzman WM. *Tissue engineering: principles for the design of replacement organs and tissues*. New York: Oxford University Press; 2004.
- [25] Ala-aho R, Kahari VM. Collagenases in cancer. *Biochim clin* 2005;87(3–4):273–86.
- [26] Livak KJ, Schmittgen TD. Analysis of relative gene expression data using real-time quantitative PCR and the $2^{-\Delta\Delta C_T}$ Method. *Methods* 2001;25(4):402–8.
- [27] Kenny PA, Lee GY, Myers CA, Neve RM, Semeiks JR, Spellman PT, et al. The morphologies of breast cancer cell lines in three-dimensional assays correlate with their profiles of gene expression. *Mol Oncol* 2007;1(1):84–96.
- [28] Nagata S. Apoptotic DNA fragmentation. *Exp Cell Res* 2000;256(1):12–8.
- [29] Whited BM, Whitney JR, Hofmann MC, Xu Y, Rylander MN. Pre-osteoblast infiltration and differentiation in highly porous apatite-coated PLLA electrospun scaffolds. *Biomaterials* 2011;32(9):2294–304.
- [30] Paszek MJ, Zahir N, Johnson KR, Lakins JN, Rozenberg GI, Gefen A, et al. Tensional homeostasis and the malignant phenotype. *Cancer Cell* 2005;8(3):241–54.
- [31] Levental KR, Yu H, Kass L, Lakins JN, Egeblad M, Erler JT, et al. Matrix cross-linking forces tumor progression by enhancing integrin signaling. *Cell* 2009;139(5):891–906.
- [32] Provenzano PP, Inman DR, Eliceiri KW, Keely PJ. Matrix density-induced mechanoregulation of breast cell phenotype, signaling and gene expression through a FAK-ERK linkage. *Oncogene* 2009;28(49):4326–43.
- [33] Ramanujan S, Pluen A, McKee TD, Brown EB, Boucher Y, Jain RK. Diffusion and convection in collagen gels: implications for transport in the tumor interstitium. *Biophys J* 2002;83(3):1650–60.
- [34] Corstorphine L, Sefton MV. Effectiveness factor and diffusion limitations in collagen gel modules containing HepG2 cells. *J Tissue Eng Regen Med* 2011;5(2):119–29.
- [35] Pampaloni F, Reynaud EG, Stelzer EH. The third dimension bridges the gap between cell culture and live tissue. *Nat Rev Mol Cell Biol* 2007;8(10):839–45.
- [36] Sharpless NE, Depinho RA. The mighty mouse: genetically engineered mouse models in cancer drug development. *Nat Rev Drug Discov* 2006;5(9):741–54.

Chapter 4: *In vitro* angiogenesis induced by tumor-endothelial cell co-culture in bilayered, collagen I hydrogel bioengineered tumors

Christopher S. Szot¹, Cara F. Buchanan¹, Joseph W. Freeman², Marissa Nichole Rylander¹

¹School of Biomedical Engineering and Sciences,
Virginia Polytechnic Institute and State University,
Blacksburg, VA 24061

²Department of Biomedical Engineering,
Rutgers University,
Piscataway, NJ 08854

CFB provided thoughtful discussion and thorough edits

4.1 Abstract

Although successful remission has been achieved when cancer is diagnosed and treated during its early stages of development, a tumor that has established neovascularization poses a significantly greater risk of mortality. The inability to recapitulate the complexities of a maturing *in vivo* tumor microenvironment in an *in vitro* setting has frustrated attempts to identify and test anti-angiogenesis therapies that are effective at permanently halting cancer progression. We established an *in vitro* tumor angiogenesis model driven solely by paracrine signaling between MDA-MB-231 breast cancer cells and microvascular endothelial (TIME) cells co-cultured in a spatially-relevant manner. The bilayered bioengineered tumor model consists of TIME cells cultured as an endothelium on the surface of an acellular collagen I hydrogel under which MDA-MB-231 cells are cultured in a separate collagen I hydrogel. Results showed that TIME cells co-cultured with the MDA-MB-231 cells demonstrated a significant increase in proliferation, rapidly developed an elongated morphology, and invasively sprouted into the underlying acellular collagen I layer. Comparatively, bioengineered tumors cultured with less aggressive MCF7 breast cancer cells did not elicit an angiogenic response. Angiogenic sprouting was demonstrated by the formation of a complex capillary-like tubule network beneath the surface of a confluent endothelial monolayer with lumen formation and anastomosing branches. *In vitro*

angiogenesis was dependent on vascular endothelial growth factor (VEGF) secretion, matrix concentration, and duration of co-culture. Basic fibroblast growth factor (bFGF) supplemented at 4 ng/ml to the co-cultures augmented angiogenic sprouting. The development of improved preclinical tumor angiogenesis models, such as the one presented here, is critical for accurate evaluation and refinement of anti-angiogenesis therapies.

4.2 Introduction

Physiological angiogenesis, or vascular neovessel formation from a pre-existing vessel, is fundamental for tissue maintenance and homeostasis during embryonic development and adult life [1-4]. Similar to normal tissue development, an expanding tumor requires oxygen and nutrients to maintain cell function, growth, and survival [4, 5]. At the early stages of development, solid tumor growth is constrained and remains dormant in the absence of angiogenesis [6]. Tumors progress from an avascular to a vascular state in response to microenvironmental changes, specifically the onset of severe hypoxia [7]. Tumor angiogenesis is a multifaceted and dynamic progression characterized by an imbalance of angiogenic promoters and inhibitors, extracellular matrix remodeling, and endothelial cell migration, proliferation, and differentiation resulting in neovessel sprouting. This process is initiated by the tumor and stromal cells, which supply an extensive panel of pro-angiogenic growth factors, most prominently vascular endothelial growth factor (VEGF) and basic fibroblast growth factor (bFGF) [8-10]. These ligands interact directly with receptor tyrosine kinases on endothelial cells from the surrounding microvasculature to promote invasive sprouting into the tumor, forming a new vascular network which propagates tumor growth [10].

The idea that inhibiting tumor angiogenesis could be an effective strategy for treating solid tumors was proposed by Judah Folkman in 1971 [11]. Since then, researchers have identified and isolated many angiogenic promoters and inhibitors that represent attractive therapeutic targets. Clinical success has been achieved, and FDA approval suggests that these drugs are capable of significantly halting cancer progression. However, in the absence of validated predictive biomarkers, developed resistance to anti-angiogenic inhibitors frequently occurs through increased redundancy of existing angiogenic factors, activation of alternative angiogenic pathways, and vasculogenic mimicry. Furthermore, anti-angiogenesis therapies often lead to augmented invasiveness and metastasis due to the selection of tumor cells capable of

surviving in severely hypoxic environments. Hence, anti-angiogenic drugs have only been shown to temporarily extend progression-free survival with merely a small improvement on overall survival [4, 12-14]. Regardless, targeting the tumor vasculature remains a promising approach for inhibiting tumor growth and merits continued investigation.

Conventional *in vitro* angiogenesis models have been designed to characterize the angiogenic activity of endothelial cells cultured on a compliant matrix, such as a collagen or fibrin hydrogel, in response to known pro-angiogenic factors [1, 15-21]. While these assays provide the foundation for contemporary angiogenesis research, a comprehensive understanding of the mechanism and interplay of angiogenic growth factors in relation to dynamic cellular and environmental interactions during tumor development is lacking. The emergence of tumor engineering, defined as the development of complex three-dimensional (3D) *in vitro* tumor models that reproduce the phenotypes and physiological responses of the *in vivo* tumor microenvironment [22], is facilitating the establishment of new platforms for identifying and testing more efficacious anti-angiogenic drugs. These systems are beginning to successfully incorporate multiple cell types (endothelial, tumor and/or stromal) into controlled 3D *in vitro* environments, demonstrating reproducible angiogenic sprouting [23-28] as well as inhibition in response to known angiogenic blockers [25, 26, 28]. However, many of these models are unable to recapitulate co-culture induced angiogenic sprouting from a confluent monolayer [24, 26, 28], which is important for maintaining proper endothelial cell polarity. Furthermore, most co-culture angiogenesis models have been unsuccessful in achieving invasive sprouting without the contribution of exogenous angiogenic growth factors [26, 27] or fibroblasts [23-25, 28].

To address this deficiency, we introduce an *in vitro* angiogenesis model based on microvascular endothelial cells cultured as a confluent monolayer on the surface of previously characterized pro-angiogenic bioengineered tumors [29] in the absence of exogenous angiogenic growth factors. These *in vitro* tumors, composed of MDA-MB-231 breast cancer cells cultured within a bulk collagen I hydrogel, have been shown to exhibit phenotypic characteristics ideal for encouraging an *in vivo*-like angiogenic response, including the development of a necrotic core, intracellular levels of hypoxia, and subsequent upregulation of VEGF gene expression. In the current study, paracrine signaling between telomerase-immortalized human microvascular endothelial (TIME) cells cultured as an endothelium on the surface of an acellular collagen I hydrogel and MDA-MB-231 cells cultured beneath in a separate collagen I hydrogel led to

augmented angiogenic activity, specifically a significant increase in TIME proliferation, the development of an elongated and aligned TIME morphology, and invasive angiogenic sprouting. This system allowed for decoupling of important cellular and environmental factors that influence co-culture induced *in vitro* angiogenesis; particularly cancer cell aggressiveness, seeding density (tumor and endothelial), matrix concentration, growth factor involvement (VEGF and bFGF), and duration of co-culture. The *in vitro* tumor angiogenesis platform presented here can be used to gain a clearer understanding of specific mechanisms involved in tumor angiogenesis, such as the time- and concentration-dependent paracrine expression and influence of different angiogenic growth factors on invasive sprouting, as well as potentially provide a more realistic and reproducible response to anti-angiogenesis therapies.

4.3 Materials and methods

4.3.1 Cell culture

MDA-MB-231 human breast cancer cells (American Type Culture Collection, Manassas, VA, USA) were cultured in DMEM/F12 (1:1) +L-Glutamine, +15mM HEPES (Invitrogen, Carlsbad, CA, USA) and supplemented with 10% fetal bovine serum (FBS) (Sigma Aldrich, St. Louis, MO, USA) and 1% Penicillin/Streptomycin (P/S) (Invitrogen). MCF7 human breast cancer cells were cultured in EMEM with L-Glutamine (ATCC) and supplemented with 10% FBS, 1% P/S, and 0.01 mg/ml insulin (Sigma Aldrich). Telomerase-immortalized human microvascular endothelial (TIME) cells stably transduced with an mKate lentivirus (generously provided by the Wake Forest Institute of Regenerative Medicine, Winston-Salem, NC, USA) were cultured in EBM-2 (Lonza Biomedical, Walkersville, MD, USA) and supplemented with an EGM-2 SingleQuots® Kit (Lonza Biomedical), which contains 2% FBS, hydrocortisone, VEGF (2 ng/ml), hFGF-B (4 ng/ml), R3-insulin growth factor, ascorbic acid, human epidermal growth factor, GA-1000, and heparin. Fluorescently labeled endothelial cells enabled convenient monitoring of angiogenic sprouting prior to immunofluorescence staining. Cell cultures were incubated in a humidified atmosphere of 95% air and 5% CO₂ at a constant temperature of 37°C.

4.3.2 Bilayered, collagen I hydrogel bioengineered tumors

Bioengineered tumors were fabricated similar to a previous study [29]. MDA-MB-231 and MCF7 cells were cultured separately in an 8 mg/ml collagen solution at a seeding density of 5×10^6 cells/ml. The tumor cell-collagen suspension was pipetted into 12-well costar transwell inserts with 0.4 μm pore polyester membranes (Corning Incorporates, Corning, NY, USA). Two-thirds of the final volume (226 μl to achieve 2 mm thickness) was allowed to polymerize for 5 min at 37°C before the final one-third of the suspension was added to fill in the naturally occurring meniscus of the collagen solution, thereby creating a flat top surface of the hydrogel. Following polymerization of the tumor cell-collagen layer, a thin acellular layer of 8 mg/ml collagen hydrogel (113 μl to achieve 1 mm thickness) was similarly added in two separate and equal volumes. Respective cell culture mediums were added to the well and insert, and medium was replenished every 24 h.

The tumor cells were cultured for 24 h, after which the TIME cells were seeded at a density of 3×10^4 cells/cm² on the surface of the acellular layer of the bilayered bioengineered tumors. The use of transwell inserts provided two separate medium compartments for the different cell types, which protected the endothelial cells from the acidic growth conditions generated by the tumor cells cultured at a high density. Respective cell culture mediums were added to the well and insert, and medium was replenished every 24 h. Figure 4.1 illustrates the co-culture experimental setup. The co-culture experimental setup maintains the appropriate

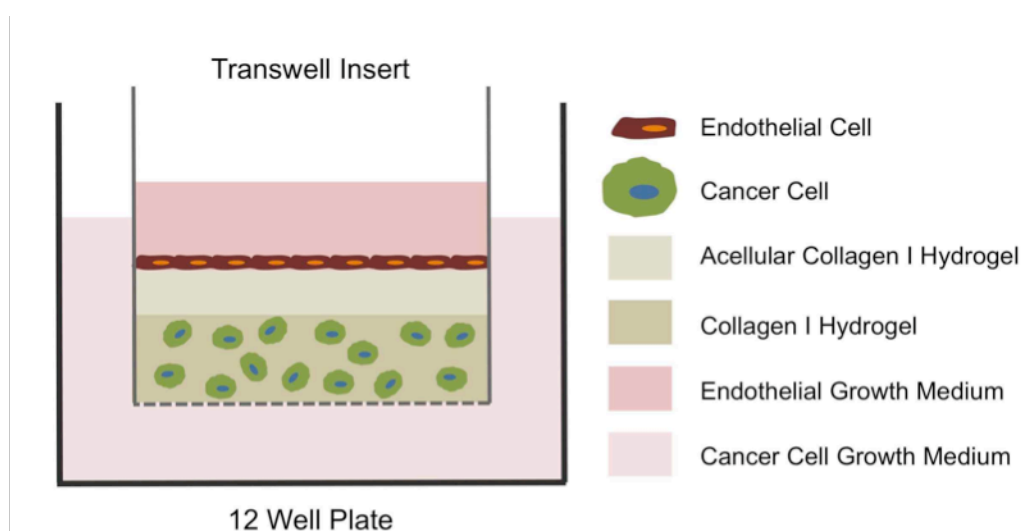


Figure 4.1. Schematic illustration of the bilayered bioengineered tumor model cultured in a transwell insert. Breast cancer cells are cultured in the bulk collagen I hydrogel and microvascular endothelial cells are cultured on the surface of an acellular layer of collagen I hydrogel separating the two cell types.

spatial relationship between the tumor and endothelial cells as well as correct endothelial cell polarity. The model was designed to focus on the cellular interactions between the tumor and endothelial cells during angiogenic sprouting without the influence of vascular flow. An acellular collagen layer was added as a barrier between the two cell types to preserve endothelial health. Previous studies have reported that direct cell-to-cell contact between breast cancer cells and endothelial cells *in vivo* and *in vitro* leads to the induction of endothelial cell apoptosis, confirmed through TUNEL labeling and a significant increase in caspase-3 activity [30]. We obtained similar results, with decreased TIME viability observed when the acellular layer was removed (Fig. 4.S1).

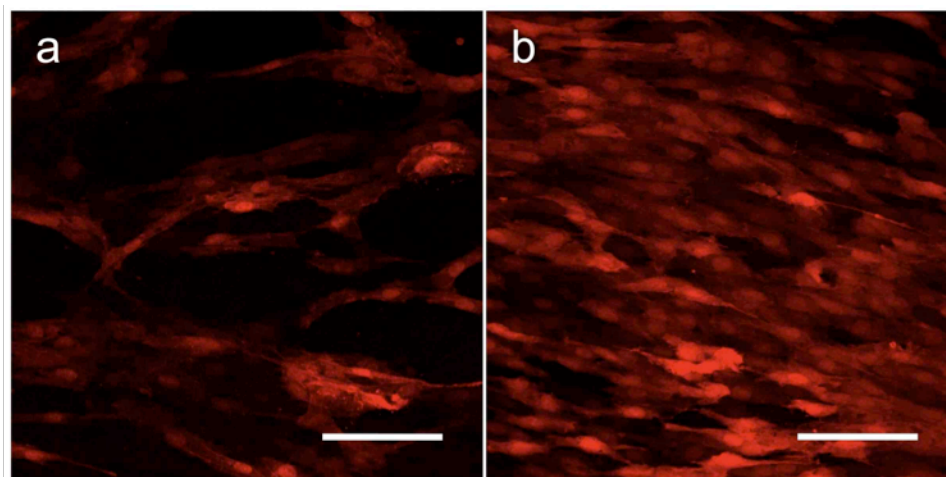


Figure 4.S1. TIME-mKate cells after 7 days of co-culture on MDA-MB-231 bioengineered tumors (a) when cultured in direct contact with the cancer cell-seeded surface and (b) when cultured on the acellular collagen hydrogel layered on top of the bioengineered tumors. TIME cell health was negatively affected through direct cell-cell contact with the breast cancer cells. Scale bars represent 100 μm .

4.3.3 Angiogenic growth factor expression

VEGF protein secretion from the bioengineered tumors (breast cancer cell monocultures only) was measured by an enzyme-linked immunosorbent assay (ELISA) using Quantikine Human Immunoassay kits (R&D Systems, Minneapolis, MN, USA) according to the manufacturer's protocol. Conditioned medium samples from the inserts were collected on days 1, 3, 5, and 7. In order to monitor temporal changes in protein secretion, fresh cell culture medium was replaced 24 h prior to each time point.

In an effort to confirm that differences in VEGF protein levels were the result of increased expression per cell, immunofluorescence staining for VEGF was conducted. The bioengineered tumors were embedded in paraffin and sectioned as described previously [29]. Sections were permeabilized with 0.5% Triton X-100 (Sigma Aldrich) and blocked with 5% goat serum (Santa Cruz Biotechnology Inc., Santa Cruz, CA, USA) for 1 h. Samples were incubated overnight with a rabbit polyclonal antibody to VEGF (Abcam Inc., Cambridge, MA, USA) at a dilution of 1:200 followed by a DyLight 488-conjugated affini-pure goat anti-rabbit IgG (H+L) secondary antibody (Jackson ImmunoResearch Laboratories Inc., West Grove, PA, USA) at a dilution of 1:100 for 1 h. VECTASHIELD® mounting medium with DAPI (Vector Laboratories, Burlingame, CA, USA) was used to preserve fluorescence and stain nuclei. Samples were imaged with a Leica DMI 6000 fluorescent microscope (Leica Microsystems Inc., Buffalo Grove, IL, USA).

4.3.4 Analysis of angiogenic activity

The capacity of the breast cancer cells in the bioengineered tumors to induce angiogenic activity by the TIME cells cultured as an endothelium was characterized by monitoring endothelial proliferation, morphological changes, and angiogenic sprouting. VEGF and bFGF were removed from the endothelial growth medium to determine if the tumor cells used in the model could provide the necessary growth factors to generate an angiogenic response without the aid of an exogenous stimulus. For the proliferation and morphology experiments, the tumors cells were seeded at a density of 5×10^6 cells/ml, the TIME cells were seeded at a density of 3×10^4 cells/cm², and the acellular collagen layer concentration was 8 mg/ml. The culturing parameters were varied for the sprouting experiments, as described below. The control group was a TIME cell monoculture on an acellular collagen hydrogel cultured with complete endothelial growth medium.

4.3.4.1 Quantification of endothelial cell proliferation

Quantification of endothelial cell number was conducted on days 1, 3, and 5 (following TIME cell seeding on bioengineered tumors). Samples were fixed with 10% formalin and permeabilized with 0.5% Triton X-100 (Sigma Aldrich). NucBlue™ Fixed Cell Stain with DAPI (Invitrogen) was used to stain nuclei. A set of 12 images were taken from each sample

using a Leica DMI 6000 fluorescent microscope, and Image J (NIH, Bethesda, MA, USA) was used to count nuclei. For these experiments, all experimental and control groups were cultured simultaneously to reduce variability due to cell passage and health, collagen batch, quality of serum, and conditions of growth.

4.3.4.2 Analysis of morphological changes

Endothelial cell morphology was analyzed on days 1, 3, 5, and 7 as described previously [31]. Briefly, cells were stained with Oregon Green® 488 phalloidin (Invitrogen), a high-affinity probe for F-actin, and NucBlue™ Fixed Cell Stain with DAPI (Invitrogen). Imaging was performed with a Zeiss LSM 510 laser scanning confocal microscope (Carl Zeiss, Thornwood, NY, USA). Representative images are shown for all groups.

4.3.4.3 Characterization of angiogenic sprouting

For the sprouting experiments, parameters were varied to characterize the cellular and environmental factors that influence co-culture induced *in vitro* angiogenesis. Besides using two breast cancer cell lines of differing aggressiveness (more aggressive MDA-MB-231 and less aggressive MCF7), the effect of growth conditions such as tumor cell seeding density (1×10^6 cells/ml and 5×10^6 cells/ml), endothelial cell seeding density (3×10^4 cells/cm² and 1×10^5 cells/cm²), acellular collagen I hydrogel concentration (2, 4, and 8 mg/ml), exogenous growth factor supplementation (complete EGM-2 with 2 ng/ml VEGF and 4 ng/ml bFGF and EGM-2 containing 10 ng/ml bFGF), and time-delay of co-culture (seeding TIME cells 1 and 5 days after initial culture of the bioengineered tumors) were investigated. Confirmation of sprouting was visualized with the fluorescent mKate lentivirus prior to immunofluorescence staining with Oregon Green® 488 phalloidin, as described above. Imaging was performed with a Zeiss LSM 510 laser scanning confocal microscope. Representative images are shown for all groups. While the trends between experimental groups remained constant throughout the study, minor variability in angiogenic sprouting within the same group was attributed to differences in cell passage and health, collagen batch, quality of serum, and conditions of growth.

4.3.5 Statistical analysis

A Student's t-test was used to determine statistical significance of the ELISA and endothelial cell proliferation data. $p < 0.05$ was considered significant. $p < 0.01$ and $p < 0.001$ were also noted.

4.4 Results

4.4.1 VEGF expression from the bioengineered tumors

Two human breast cancer cell lines of differing degrees of aggressiveness were cultured individually within bulk collagen I hydrogels cast in 12-well transwell inserts. The more aggressive MDA-MB-231 cells were shown to proliferate and interact with the surrounding collagen matrix to a greater extent than the less aggressive MCF7 cells over 7 days in culture (Fig. 4.S2). In addition, the MDA-MB-231 bioengineered tumors secreted a significantly greater ($p < 0.001$) concentration of VEGF than the MCF7 bioengineered tumors at each time point over 7 days in culture (Fig. 4.2). There was a significant increase in protein secretion by the MDA-MB-231 bioengineered tumors at each time point (day 3, 5: $p < 0.001$; day 7: $p < 0.01$), compared to the previous time point, which correlated with the observed MDA-MB-231 proliferation. The

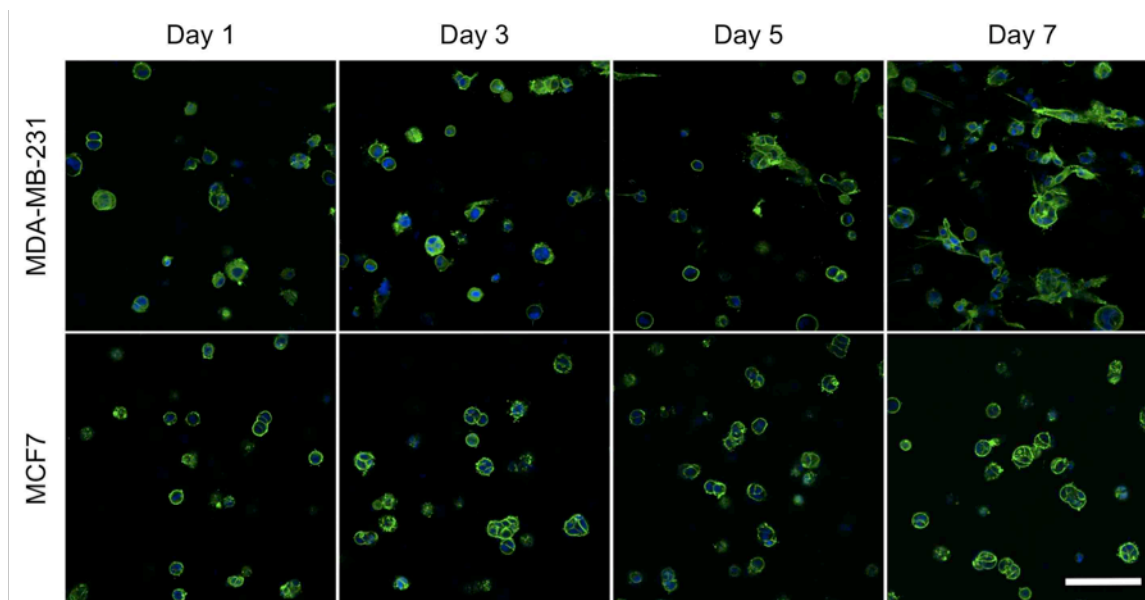


Figure 4.S2. Tumor cell proliferation and cell-matrix interactions within the bioengineered tumors. MDA-MB-231 cells proliferated and interacted with the surrounding matrix to a greater extent than MCF7 cells when cultured in dense collagen I hydrogels over a 7-day period. Green, F-actin; blue, nuclei. Scale bar represent 100 μm .

MCF7 bioengineered tumors exhibited a significant increase ($p < 0.05$) in protein secretion only from day 1-3, with no statistical difference observed after day 3. Immunofluorescence staining for VEGF confirmed that the distinction in VEGF protein secretion between the two cell types was a result of increased expression per cell rather than differences in cell number (Fig. 4.S3).

The dotted line in Figure 4.2 represents the concentration of VEGF supplemented in the complete endothelial growth medium (2 ng/ml). This is important to note since the control group for subsequent co-culture experiments was a TIME cell monoculture on an acellular collagen hydrogel cultured with complete endothelial growth medium. While the MCF7 bioengineered tumors secreted a similar concentration of VEGF compared to the complete medium, the MDA-MB-231 bioengineered tumors secreted a considerably greater concentration of VEGF at each time point. An ELISA was unable to detect bFGF in the bioengineered tumor conditioned medium, which is a limitation of using an *in vitro* model containing only one cell type.

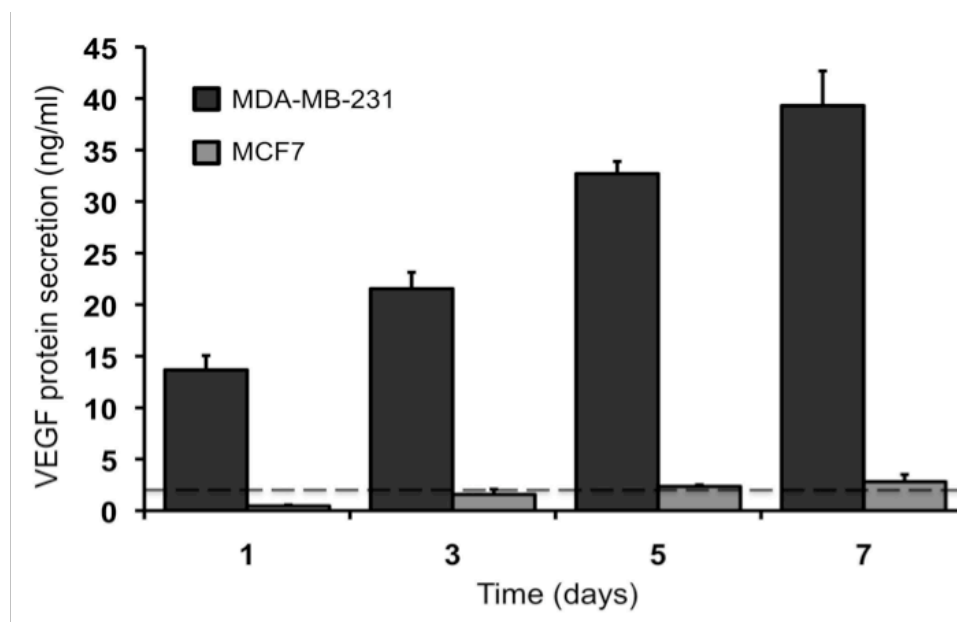


Figure 4.2. VEGF protein secretion from bioengineered tumors seeded with MDA-MB-231 or MCF7 cells. There was a significant difference ($p < 0.001$) in protein secretion between the two groups at each time point. There was a significant increase in protein secretion by the MDA-MB-231 bioengineered tumors at each time point (day 3, 5: $p < 0.001$; day 7: $p < 0.01$), as compared to the previous time point. The MCF7 bioengineered tumors exhibited a significant increase ($p < 0.05$) in protein secretion only on day 3, as compared to day 1. The dotted line represents the concentration of VEGF supplemented in the complete endothelial growth medium (2 ng/ml).

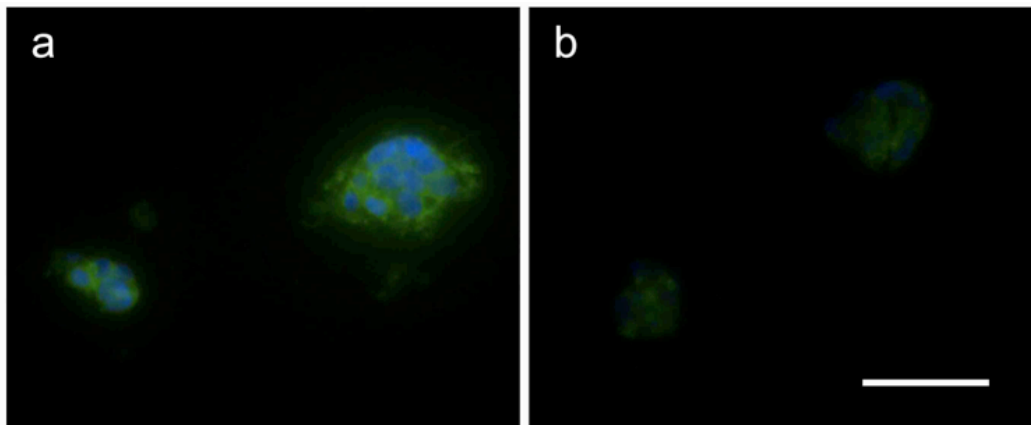


Figure 4.S3. Immunofluorescence staining for intracellular VEGF expression. (a) MDA-MB-231 cells expressed greater levels of VEGF than (b) MCF7 cells cultured within the bioengineered tumors. Green, VEGF; blue, nuclei. Scale bar represents 50 μm .

4.4.2 Tumor-endothelial cell co-culture regulates endothelial cell proliferation

Tumor-endothelial cell co-culture led to significant changes in TIME cell proliferation compared to the control group, with the MDA-MB-231 bioengineered tumors stimulating endothelial proliferation and the MCF7 bioengineered tumors reducing endothelial proliferation (Fig. 4.S4). TIME cell number on the MDA-MB-231 bioengineered tumors was significantly greater (day 1, 3: $p < 0.05$; day 5: $p < 0.01$) at each time point compared to the MCF7 bioengineered tumors (Fig. 4.3). This difference was directly related to the significant increase in VEGF protein secretion by the MDA-MB-231 bioengineered tumors as determined by an ELISA (Fig. 4.2). Compared to the control group, TIME cell number on the MDA-MB-231 bioengineered tumors was significantly greater ($p < 0.01$) on days 1 and 3. By day 5, TIME cells cultured on the MDA-MB-231 bioengineered tumors and the control group had reached confluence; therefore, there was no statistical difference in cell number. TIME cell number was statistically less ($p < 0.01$) on the MCF7 bioengineered tumors than the control group only on day 5. This difference was likely due to a combination of low VEGF protein secretion levels from the MCF7 bioengineered tumors and decreased availability of growth supplements in the medium (such as FBS) since there were a greater total number of cells competing for the same volume of medium compared to the control group. It is also possible that MCF7 cells secrete anti-angiogenic factors that suppress endothelial cell growth, similar to pancreatic cancer cells

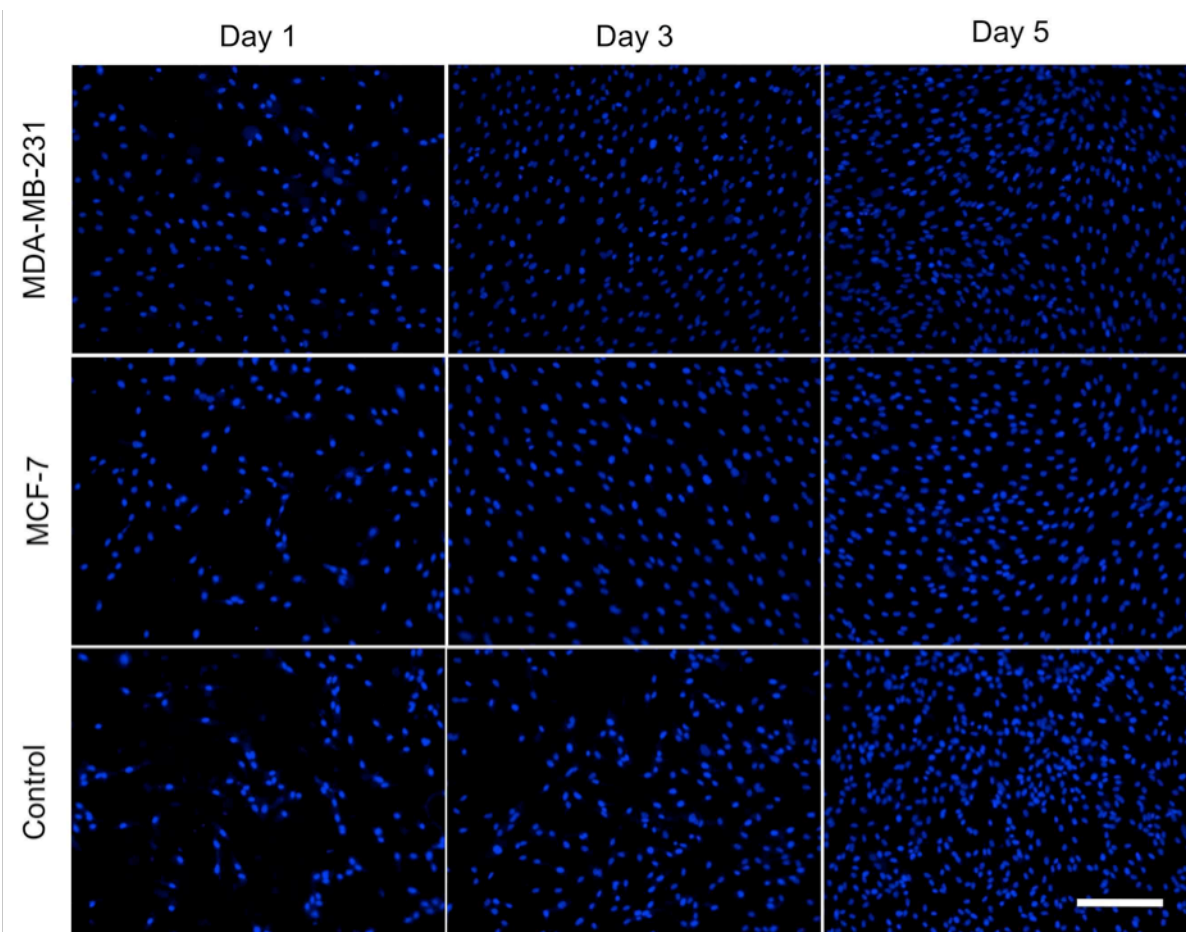


Figure 4.S4. TIME cells stained with DAPI cultured on the surface of the bioengineered tumors. TIME cells cultured on the surface of MDA-MB-231 bioengineered tumors proliferated at a faster rate than TIME cells cultured on MCF7 bioengineered tumors with TIME cell number greater at each time point. TIME cell number on the MDA-MB-231 bioengineered tumors was greater on days 1 and 3 compared to the control group. By day 5, TIME cells cultured on the MDA-MB-231 and control groups reached confluence; therefore there was no difference in cell number. Scale bar represents 200 μm .

[32], which may maintain their less aggressive phenotype *in vivo*. TIME cell number increased significantly from day 1 to day 3 and from day 3 to day 5 in all groups.

4.4.3 Tumor-endothelial cell co-culture elicits an elongated endothelial cell morphology

TIME cells cultured on the surface of the MDA-MB-231 bioengineered tumors developed elongated and tightly aligned morphologies over a 7-day period, with morphological changes becoming evident by day 3 (Fig. 4.4). Although TIME cells cultured on the MCF7

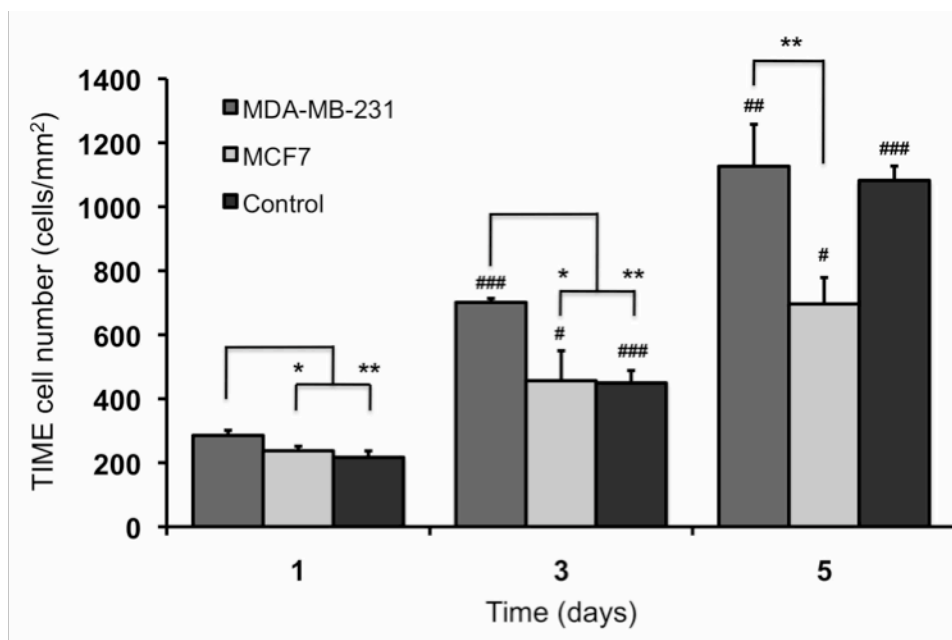


Figure 4.3. TIME cell proliferation when cultured on the surface of the bioengineered tumors. TIME cells cultured on the surface of MDA-MB-231 bioengineered tumors proliferated at a faster rate than TIME cells cultured on MCF7 bioengineered tumors with TIME cell number significantly greater at each time point. TIME cell number on the MDA-MB-231 bioengineered tumors was significantly greater on days 1 and 3 compared to the control group. By day 5, TIME cells cultured on the MDA-MB-231 and control groups reached confluence; therefore, there was no statistical difference in cell number. TIME cell number in each group was significantly greater than the previous time point on days 3 and 5. * denotes significant difference between groups, and # denotes significant difference within the same group compared to the previous time point. */#, **/##, and ***/### indicate $p < 0.05$, 0.01, and 0.001, respectively.

bioengineered tumors did not reach confluence following 7 days of co-culture, an elongated morphology was observed. When complete endothelial growth medium was provided to the TIME cells cultured on the MCF7 bioengineered tumors, the cells became confluent and displayed similar elongated and tightly aligned morphologies to the TIME cells cultured on the MDA-MB-231 bioengineered tumors (Fig. 4.S5). Conversely, TIME cells in the control group reached confluence by day 5 but did not undergo any morphological changes. The development of an elongated morphology was not a consequence of over confluence as endothelial cell number on the MDA-MB-231 bioengineered tumors and the control group were similar on day 5 (Fig. 4.3). Furthermore, since the supplemented VEGF and bFGF were removed from the co-culture groups, these results suggest that paracrine growth factors from both types of breast

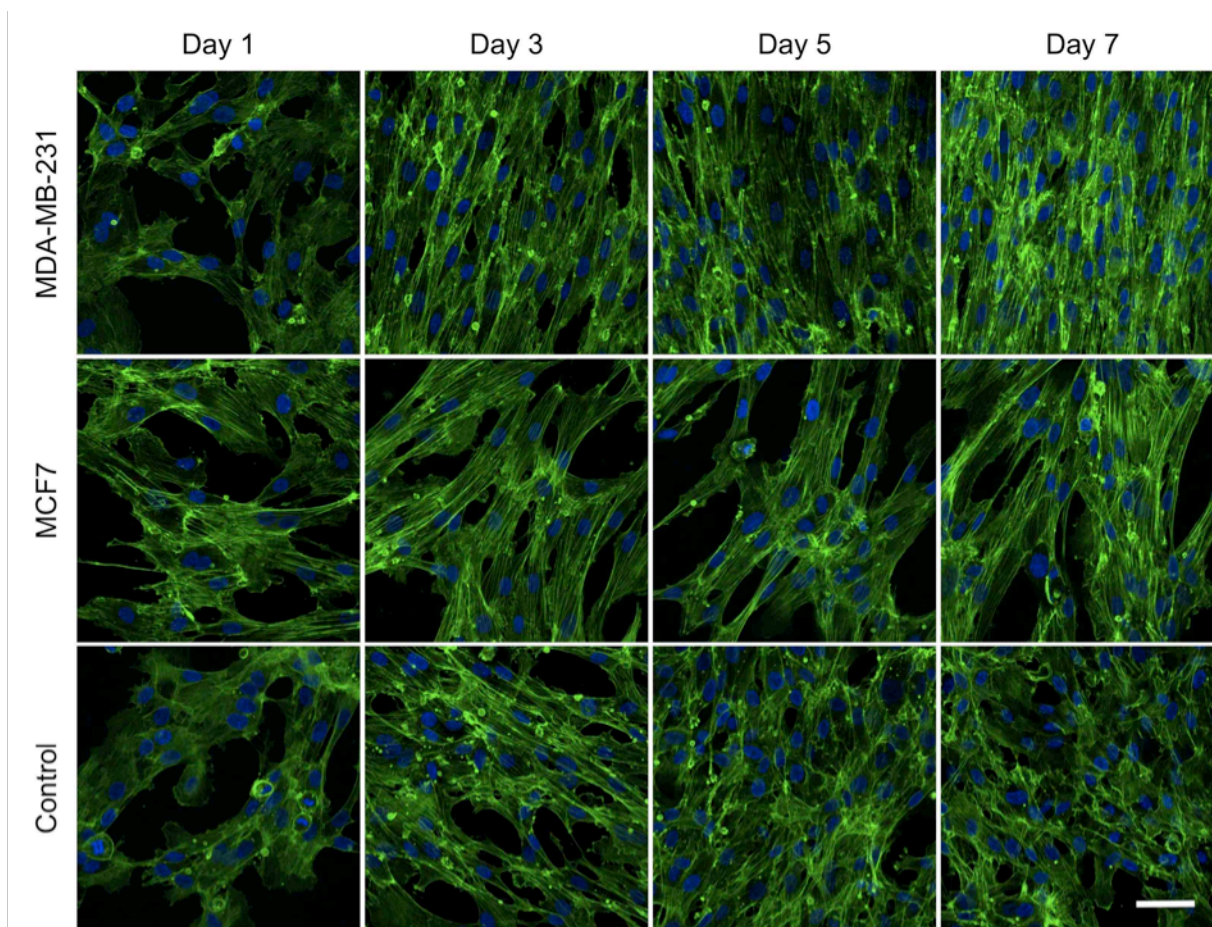


Figure 4.4. TIME cell morphology when cultured on the surface of the bioengineered tumors. TIME cells became elongated and tightly aligned when co-cultured on MDA-MB-231 bioengineered tumors. Although TIME cells did not reach confluence on the MCF7 bioengineered tumors, an elongated morphology was observed. Conversely, TIME cells in the control group reached confluence, but they did not undergo any morphological changes. Green, F-actin; blue, nuclei. Scale bars represent 50 μm .

cancer cells, other than VEGF and bFGF, are responsible for encouraging an *in vivo*-like elongated and aligned endothelial morphology in the absence of vascular flow. Similar morphological changes were observed when the TIME cells were cultured on lower concentrations of the acellular collagen hydrogel layer (2 and 4 mg/ml) (data not shown).

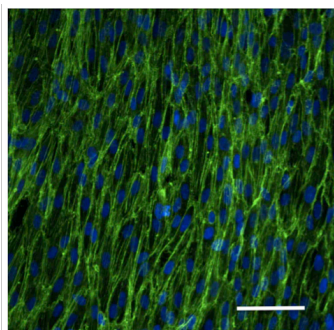


Figure 4.S5. TIME cells cultured on the MCF7 bioengineered tumors reached confluence on day 7 when supplemented with complete endothelial growth medium. TIME cells displayed an elongated and tightly aligned morphology similar to when cultured on the MDA-MB-231 bioengineered tumors. Green, F-actin; blue, nuclei. Scale bars represent 50 μm .

4.4.4 Tumor-endothelial cell co-culture induces invasive angiogenic sprouting

Invasive angiogenic sprouting was observed when TIME cells were cultured on the surface of the more aggressive MDA-MB-231 bioengineered tumors (Fig. 4.5) but not with the less aggressive MCF7 bioengineered tumors. In order to facilitate sprouting, the concentration of the acellular collagen layer was reduced as sprouting could not be attained when the TIME cells were cultured on an 8 mg/ml acellular collagen hydrogel. A capillary-like tubule network was shown to develop beneath the surface of a confluent monolayer of TIME cells (2 mg/ml acellular collagen layer) after 7 days of co-culture (Fig. 4.5a, b). Select tubules contained patent lumens, typically surrounded by a single endothelial cell (4 mg/ml acellular collagen layer) (Fig. 4.5c). These results validate that paracrine signaling between the tumor and endothelial cells in the bilayered bioengineered tumor *in vitro* angiogenesis model is sufficient to induce angiogenic sprouting with complex capillary-like tubule formation without the addition of exogenous pro-angiogenic growth factors (VEGF and bFGF removed from endothelial growth medium). Angiogenic sprouting was also observed in the control group when TIME cells were cultured on 2 mg/ml acellular collagen hydrogels with complete endothelial growth medium (Fig. 4.6). However, TIME cells were not shown to develop capillary-like tubule networks beneath the surface monolayer (Fig. 4.6a, b). Rather, sprouting was characterized by isolated points of

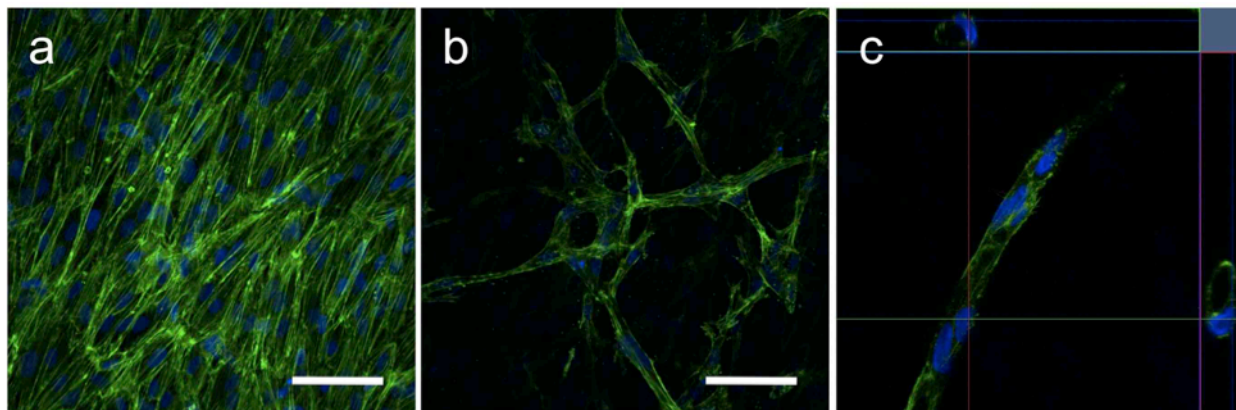


Figure 4.5. Angiogenic sprouting of TIME cells cultured on MDA-MB-231 bioengineered tumors in the absence of exogenous VEGF and bFGF. (a) TIME cells grown to confluence after 7 days on a 2 mg/ml acellular collagen hydrogel layer of the bioengineered tumor (b) formed a capillary-like tubule network beneath the surface. (c) Select tubules were shown to develop patent lumens (day 10; 4 mg/ml acellular collagen layer). The top and side panels of (c) illustrate cross-sectional cuts of a single tubule in the x-z and y-z directions. Green, F-actin; blue, nuclei. Scale bars represent 50 μ m.

endothelial invasion with radially branching filopodia (Fig. 4.6c, d). When TIME cells cultured with the MCF7 bioengineered tumors were provided complete endothelial growth medium, angiogenic sprouting was still not observed. The inability to reproduce a similar response to the control group, with identical concentrations of supplemented VEGF and bFGF, supports the possibility that MCF7 cells may secrete anti-angiogenic factors.

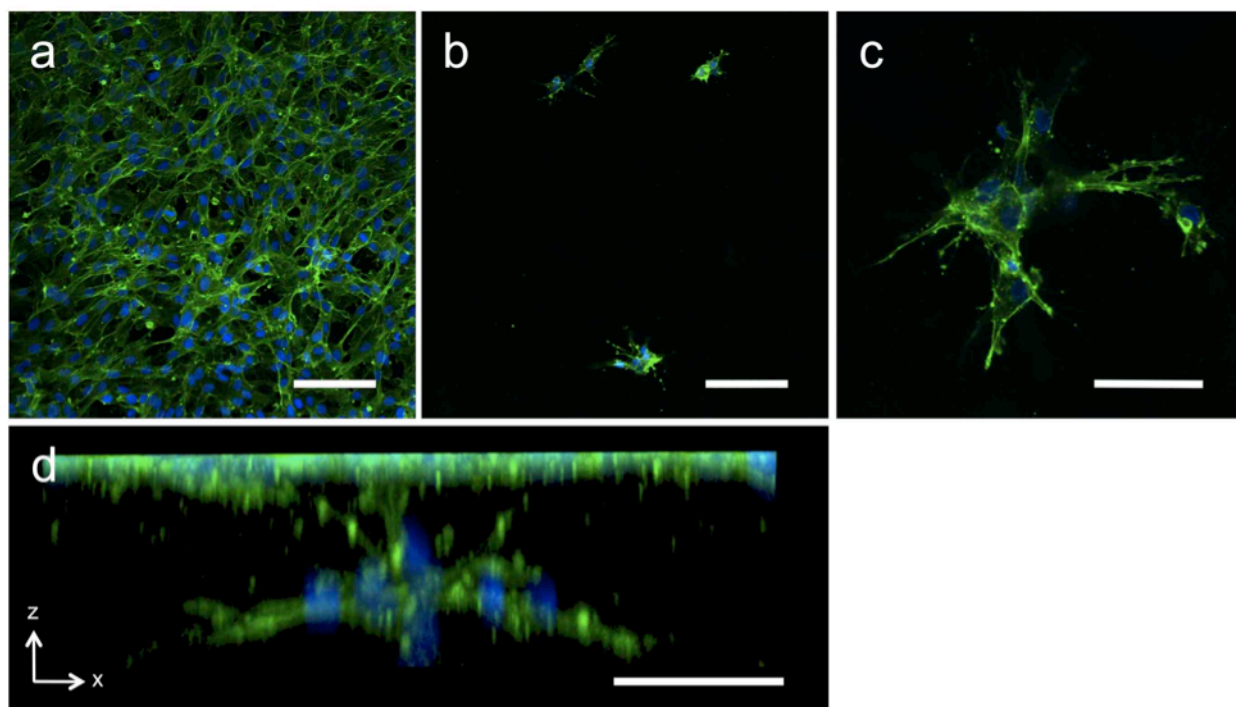


Figure 4.6. Angiogenic sprouting of TIME cells in the control group. (a) TIME cells grown to confluence after 7 days on a 2 mg/ml acellular collagen hydrogel layer of the control group demonstrated (b) isolated points of invasion with (c) radially branching filopodia beneath the surface. (d) Three-dimensional image reconstruction of an isolated sprouting event. Green, F-actin; blue, nuclei. Scale bars represent (a, b) 100 μm and (c, d) 50 μm .

4.4.5 Acellular collagen matrix concentration governs angiogenic sprouting

The concentration of the acellular collagen hydrogel layer was a limiting factor in supporting angiogenic sprouting on the MDA-MB-231 bioengineered tumors. After 7 days of co-culture, sprouting with branching tubule formation was only observed when TIME cells were cultured on a 2 mg/ml acellular collagen layer (Fig. 4.7a). Three-dimensional image reconstruction accentuated the complexity of the capillary-like tubule network that was achieved. Separate tubules were shown to anastomose and extend far beneath the confluent monolayer

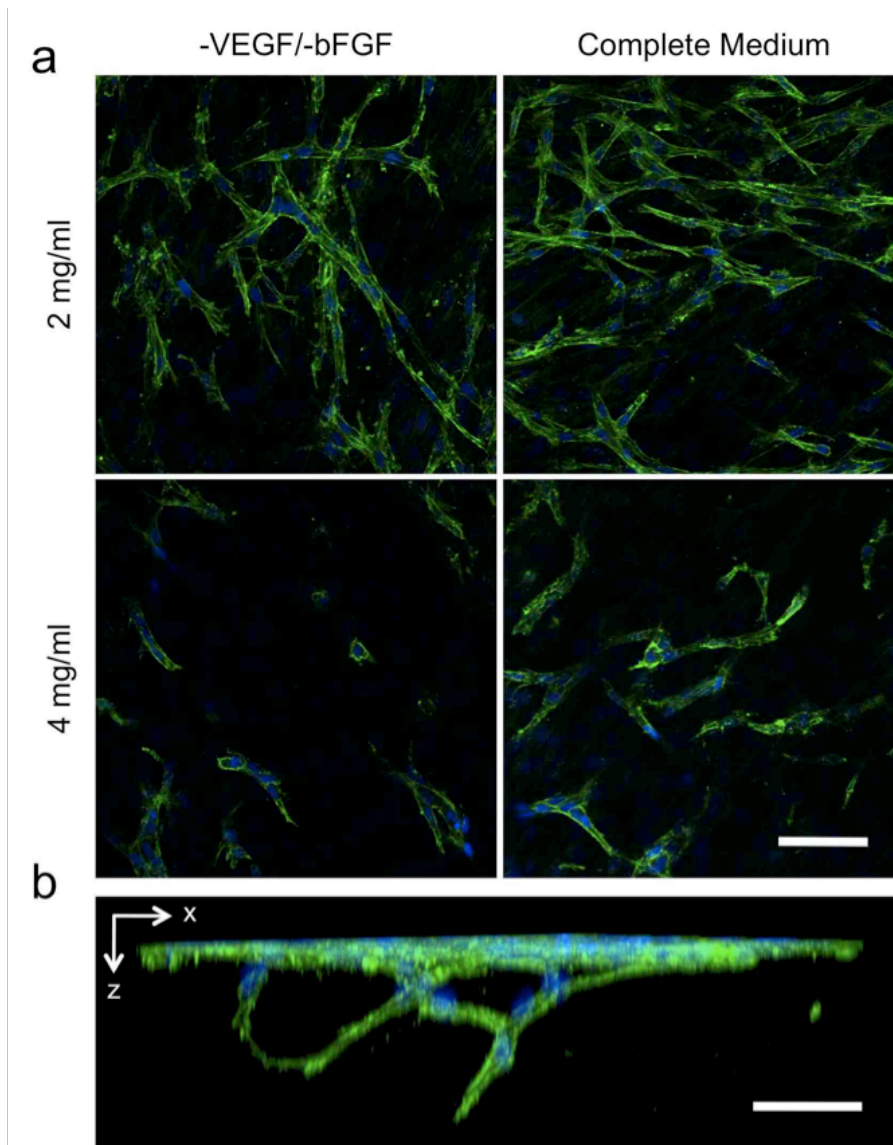


Figure 4.7. Influence of matrix concentration and supplemented bFGF on angiogenic sprouting of TIME cells cultured for 7 days on MDA-MB-231 bioengineered tumors. (a) A considerably greater degree of angiogenic sprouting was observed within the 2 mg/ml acellular collagen layers as compared to the 4 mg/ml acellular collagen. Sprouting was augmented within both collagen concentrations when complete medium containing bFGF (4 ng/ml) was supplemented to the co-culture TIME cells. (b) Three-dimensional image reconstruction shows two separate tubules anastomosing and extending down beneath the surface monolayer (2 mg/ml acellular collagen layer; 10 ng/ml bFGF). Green, F-actin; blue, nuclei. Scale bars represent 50 μm .

(Fig. 4.7b). TIME cells cultured on a 4 mg/ml acellular collagen hydrogel began to invade beneath the surface, but these sprouting tubules were scarce, shorter in length, and showed no signs of branching (Fig. 4.7a). As mentioned above, invasive tubule formation was not observed within the 8 mg/ml acellular collagen hydrogel. The observed correlation between matrix concentration and the degree of sprouting indicates that collagen degradation may be a rate-limiting step in regulating invasive sprouting, as reported previously [33].

4.4.6 Angiogenic growth factor composition and concentration influence angiogenic sprouting

The influence of exogenous bFGF and endogenous VEGF on angiogenic sprouting was explored through changing the medium composition and altering the seeding density of the MDA-MB-231 bioengineered tumors, respectively. When co-culture TIME cells were provided complete endothelial growth medium (2 ng/ml VEGF and 4 ng/ml bFGF) for the extent of the study, angiogenic sprouting was enhanced on both the 2 mg/ml and 4 mg/ml acellular collagen layers, as compared to the non-VEGF and bFGF supplemented co-cultures which only contained endogenous VEGF (Fig. 4.7a). It is probable that this increase was in response to the addition of bFGF as an ELISA was unable to detect bFGF in the MDA-MB-231 bioengineered tumor conditioned medium (data not shown). Furthermore, the endogenous concentration of VEGF secreted by the MDA-MB-231 bioengineered tumors was significantly larger than the amount provided in the complete medium; hence, it is unlikely that the exogenous VEGF from the medium provided an added stimulus to the VEGF already present within the system. Augmented *in vitro* angiogenic sprouting in response to VEGF and bFGF co-stimulation as compared to either growth factor alone has been shown previously using an endothelial cell monoculture assay [1]. In that study, optimal sprouting was obtained when 30 ng/ml VEGF and 10 ng/ml bFGF were supplemented to the endothelial cells. However, when 10 ng/ml bFGF was added to TIME cells cultured with the MDA-MB-231 bioengineered tumors, angiogenic sprouting was not further increased (data not shown).

MDA-MB-231 bioengineered tumors seeded at a lower density (1×10^6 cells/ml) were shown to secrete a significantly lower concentration of VEGF (4-fold) ($p < 0.001$) than the high seeding density (5×10^6 cells/ml) bioengineered tumors at each time point (Fig. 4.S6a). However, this concentration on day 7 was still 5-fold greater than the VEGF provided in the complete endothelial growth medium. TIME cells cultured with the low seeding density MDA-MB-231

bioengineered tumors proliferated at a similar rate to the high seeding density bioengineered tumors (Fig. 4.S6b) and developed identical elongated and aligned morphologies (Fig. 4.S6c). Invasive angiogenic sprouting was observed within both the 2 mg/ml (Fig 4.S6d) and 4 mg/ml acellular collagen layers, with and without complete endothelial growth medium. While there was a minor decrease in the extent of angiogenic sprouting within the 4 mg/ml acellular collagen layers as compared to the high seeding density bioengineered tumors, it is clear that the MDA-MB-231 bioengineered tumors seeded at a density of 1×10^6 cells/ml provided sufficient VEGF signaling to induce a comparable angiogenic response.

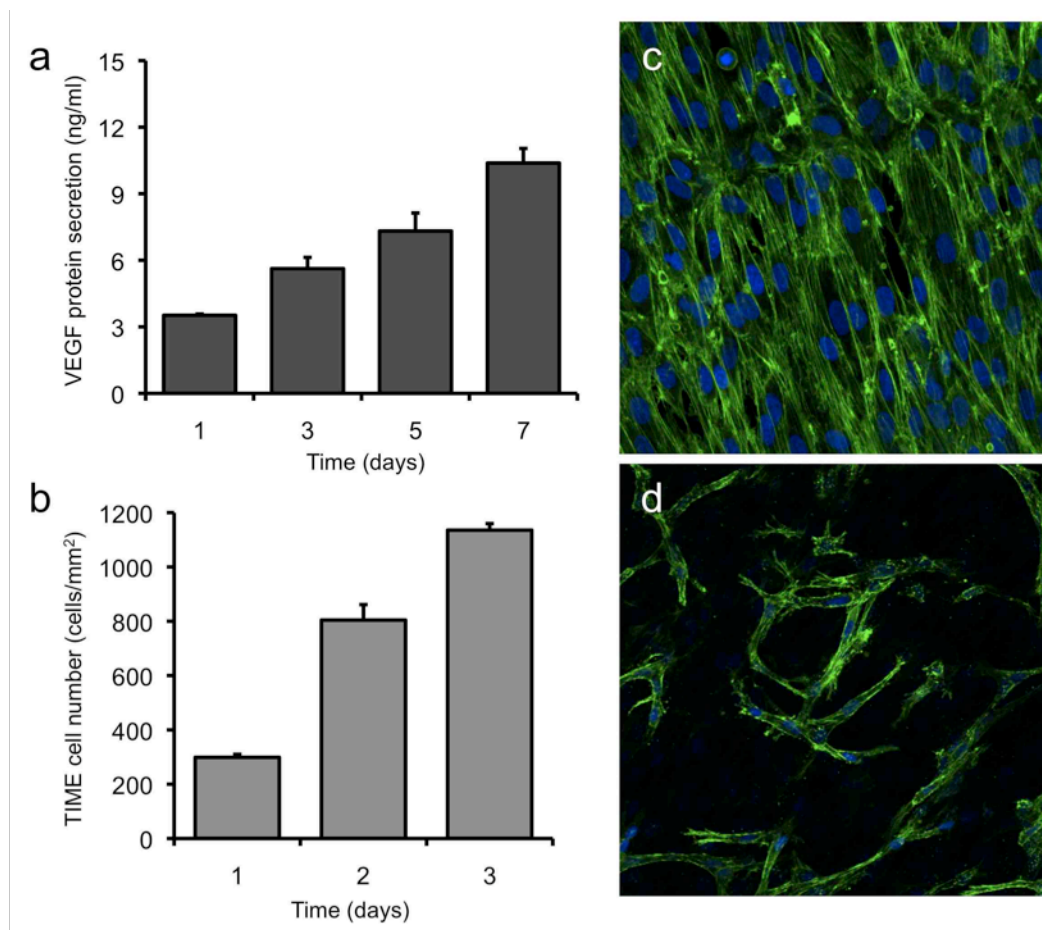


Figure 4.S6. (a) VEGF protein secretion from bioengineered tumors cultured with MDA-MB-231 cells at a density of 1×10^6 cells/ml. TIME cells cultured on the 1×10^6 cells/ml MDA-MB-231 bioengineered tumors (b) proliferated, (c) developed elongated and aligned morphologies (day 7), and (d) formed capillary-like tubules (day 7; 2 mg/ml acellular collagen) similar to when cultured on the 5×10^6 MDA-MB-231 bioengineered tumors.

4.4.7 Duration of co-culture determines induction but not extent of angiogenic sprouting

When co-cultured under optimal sprouting conditions (2 mg/ml acellular collagen; complete medium), capillary-like tubule formation was not observed until day 5 (Fig. 4.8a). In an attempt to accelerate tubule growth, TIME cells were seeded at confluence (1×10^5 cells/cm²), as determined from the proliferation experiment (Fig. 4.3). This approach was derived from previous *in vitro* angiogenesis studies that have allowed endothelial cells to reach confluence before inducing angiogenic activity [1, 17-19], as it has been shown that tubule formation only occurs when endothelial cells have a low proliferative potential [16]. While there was a minor increase in the number of sprouting events, capillary-like tubule formation was still not observed

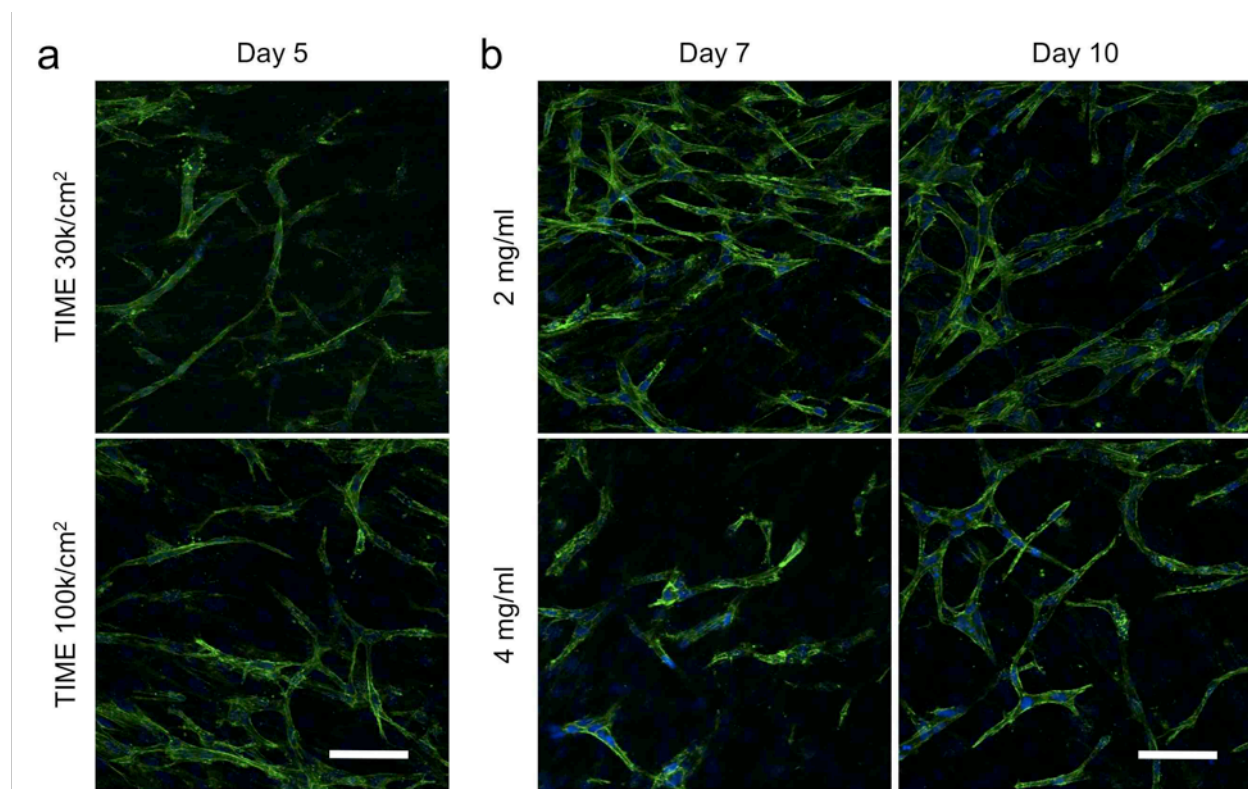


Figure 4.8. Influence of (a) TIME cell seeding density and (b) duration in co-culture on angiogenic sprouting. (a) Angiogenic sprouting with noticeable capillary-like tubule formation was not observed within the 2 mg/ml acellular collagen until day 5, regardless of the TIME cell seeding density. However, seeding the TIME cells at confluence (1×10^5 cells/cm²) resulted in a minor increase in the number of sprouting events. (b) Sprouting reached a maximum by day 7 when TIME cells were cultured on the 2 mg/ml acellular collagen layer but continued to progress through day 10 when cultured on the 4 mg/ml acellular collagen layer. Green, F-actin; blue, nuclei. Scale bars represent 50 μ m.

until day 5 (Fig. 4.8a). Another approach was to seed the TIME cells on the acellular collagen layer 5 days following initial culture of the MDA-MB-231 bioengineered tumors when there was a significantly greater concentration of secreted VEGF, as compared to day 1 (Fig. 4.2). Similar to increasing the TIME cell seeding density, a minor increase in the number of sprouting events was observed, but capillary-like tubule formation was not seen until day 5 (data not shown). Based on these results, it is possible that additional time-dependent crosstalk between the tumor and endothelial cells, besides VEGF signaling, is necessary to encourage angiogenic sprouting [34].

There was no noticeable increase in angiogenic sprouting between day 7 and day 10 from TIME cells cultured on the 2 mg/ml acellular collagen layer when supplemented with complete endothelial growth medium (Fig. 4.8b). Alternatively, sprouting continued to progress through day 10 within the 4 mg/ml acellular collagen, with tubule growth and the formation of a branching network observed (Fig. 4.8b). When the co-culture was not supplemented with complete medium, sprouting also increased on both the 2 mg/ml and 4 mg/ml acellular collagen layers (data not shown). This indicates that the rate of sprouting within this system is dependent on both matrix concentration and growth factor involvement, and the extent of sprouting is terminal. Given enough time in co-culture, sprouting will reach a maximum limit, as observed previously [18].

4.5 Discussion

The first demonstration of *in vitro* angiogenesis was reported by Judah Folkman in 1980 [15]. In that study, capillary endothelial cells were cultured on gelatin and stimulated to form tubule networks when provided tumor-conditioned medium. Over the next decade, endothelial cell monoculture assays provided a fundamental understanding of the function of many pro-angiogenic factors, including bFGF [18], VEGF [19], and phorbol esters [17], individually as well as synergistically [1, 20]. More recently, co-culture angiogenesis assays have relied on paracrine signaling to promote angiogenic tubule formation. These systems can be separated into three categories: (1) tumor and endothelial cells co-cultured in a single monolayer [35, 36], (2) endothelial cells embedded within a bulk hydrogel with the tumor cells cultured separately or in contact with the endothelial cells [24, 26, 28], and (3) endothelial cells cultured as a monolayer on the surface of a bulk hydrogel containing tumor cells [25, 27]. While these models allow for

the study of multicellular interactions during tumor angiogenesis, each of these systems is flawed for one or more of the following reasons: the lack of an underlying matrix for endothelial remodeling [35, 36], inaccurate spatial relationships between tumor/stromal and endothelial cells [25, 28, 35, 36], incorrect endothelial polarity [26, 28], and a reliance on exogenous pro-angiogenic growth factors [26, 27, 36]. In this study, we established an *in vitro* tumor angiogenesis model based on the hypothesis that paracrine signaling between tumor and endothelial cells co-cultured in a spatially-relevant manner is sufficient for inducing an angiogenic response in the absence of exogenous pro-angiogenic growth factors. Microvascular endothelial cells cultured as an endothelium on the surface of aggressive MDA-MB-231 bioengineered tumors demonstrated a significant increase in proliferation, rapidly developed an elongated morphology, and invasively sprouted into an underlying acellular collagen I layer, forming a complex capillary-like tubule network with lumen formation and anastomosing branches.

To the best of our knowledge, the bilayered bioengineered tumor angiogenesis model represents the first demonstration of tumor-endothelial cell paracrine signaling-induced invasive angiogenic sprouting into a three-dimensional matrix. Previous groups have attempted to study this interaction but have been unable to achieve angiogenic sprouting without the addition of fibroblasts. In a similar co-culture setup, tumor cells cultured in a collagen hydrogel beneath an endothelial cell monolayer were reported to have proliferated too quickly, leading to high levels of acidity and endothelial toxicity [23]. When fibroblasts were cultured in place of the tumor cells, the endothelial cells invasively sprouted into the collagen, forming capillary-like tubules. Similarly, endothelial cells cultured in direct contact with tumor cells as multicellular spheroids embedded in a collagen hydrogel were unable to sprout due to cell-cell contact-induced endothelial cell apoptosis [28]. When the multicellular spheroids were cultured with fibroblasts and tumor cells, endothelial viability was maintained and sprouting was observed. In studies where endothelial cell health was not jeopardized by tumor cell co-culture, fibroblasts were still required for supporting endothelial invasive sprouting, in addition to the tumor cells [24, 25]. It is assumed that the fibroblasts provided an additional angiogenic growth factor stimulus necessary for inducing an angiogenic response. While fibroblasts are a central component of the tumor stroma, understanding the distinct influence of tumor cells on angiogenic sprouting will

allow for decoupling of their role from fibroblasts, providing a clearer understanding of the complex paracrine signaling network that drives tumor angiogenesis.

Matrix concentration, growth factor involvement, and duration of co-culture were important aspects of our bilayered bioengineered tumor model that influenced the extent of *in vitro* angiogenic sprouting. Endothelial cell remodeling of collagen I hydrogels has recently been shown to progress in both a time and concentration dependent manner, with the magnitude of endothelial network formation increasing with time and the rate of network formation decreasing with collagen concentration [33], similar to our results. Additionally, endothelial invasion in the lowest collagen hydrogel concentration (3 mg/ml) only progressed until day 14 while invasion in the higher concentrations (6 and 10 mg/ml) continued to increase until day 21 [33]. While we attributed this to the terminal nature of *in vitro* angiogenic sprouting within our system, it has been suggested in other studies that stiffer matrices may provide a more secure architecture for maintaining angiogenic sprouting longer with stable tubule formation [21, 33, 37]. Since angiogenic sprouting was contingent on both matrix concentration and growth factor involvement in the bioengineered tumor model, the inability to induce invasive sprouting within the 8 mg/ml acellular collagen layer was likely due to an insufficient concentration and/or composition of paracrine angiogenic growth factors. This highlights an important distinction between monoculture and co-culture angiogenesis assays. Endothelial cells cultured alone can be forced to differentiate into an angiogenic phenotype on many different types and concentrations of matrices if supplemented with an appropriate cocktail of pro-angiogenic factors. Alternatively, co-culture models rely on paracrine signaling and therefore may produce an angiogenic response that is not as pronounced. Nevertheless, we believe that exploiting multicellular interactions to generate *in vitro* angiogenesis, rather than exogenous stimuli, will provide a more physiologically-accurate response.

Angiogenic sprouting was strongly influenced by endogenous VEGF and exogenous bFGF. MDA-MB-231 bioengineered tumors secreted an ample concentration of VEGF, which resulted in a significant increase in TIME proliferation and invasive sprouting. Bioengineered tumors cultured with a lower seeding density of MDA-MB-231 cells were shown to generate an identical angiogenic response, indicating that the concentration of VEGF required to provoke this level of angiogenic activity is <10 ng/ml and a 4-fold increase in concentration does not enhance this response. Supplementing the co-culture TIME cells with exogenous bFGF (4 ng/ml)

led to an increase in angiogenic sprouting. It is possible that this additive effect is related to an increase in plasminogen activator (PA) expression by the TIME cells as PA activity, which is necessary for endothelial invasion, is regulated by bFGF [18] and not influenced by VEGF [19]. bFGF has previously been shown to induce more developed capillary-like tubule formation at the same concentration as VEGF, and co-stimulation with both growth factors has led to accelerated tubule formation as compared to either ligand alone [1]. Similar to VEGF, increasing the concentration of bFGF (10 ng/ml) in our co-culture did not lead to an enhanced response. The concentrations of VEGF (10 ng/ml) and bFGF (4 ng/ml) required to obtain a maximum synergistic effect in our system were considerably less than what has been reported in a monoculture angiogenesis assay (VEGF 30 ng/ml, bFGF 10 ng/ml) [1]. This supports the notion that the impact of an individual cytokine on tumor angiogenesis is contextual, i.e. it relies on the presence of other factors in the microenvironment [1, 20]. However, within co-culture angiogenesis models, it is challenging to monitor the interplay among the multitude of growth factors secreted in relation to dynamic cellular and environmental interactions. In our study, the inability to induce angiogenic sprouting prior to 5 days in co-culture, regardless of seeding the endothelial cells at confluence or an increased concentration of endogenous VEGF, strongly suggests that additional paracrine signaling between the tumor and endothelial cells occurs in a time-dependent manner and is necessary for stimulating *in vitro* angiogenesis. It is possible that the angiopoietins (ANG) have active roles in regulating angiogenic sprouting within our model as we have previously reported that a shift in the ANG1:ANG2 ratio occurs in favor of an increase in ANG2 expression by MDA-MB-231 cells when co-cultured with microvascular endothelial cells [34].

While *in vitro* angiogenesis assays have been used in cancer research for a few decades, these systems have relied on exogenous stimuli and incorrect culturing conditions to induce an angiogenic response. This presents a problem since determining the therapeutic impact of potential angiogenic inhibitors is highly dependent on the pro-angiogenic stimulus. If the stimulus is incorrect (composition and/or concentration of exogenous growth factors) or the system is physiologically-inaccurate (incorrect spatial relationships and endothelial polarity), any conclusions obtained using those models may be unreliable in an *in vivo* setting. As the bilayered bioengineered tumor angiogenesis model presented here was driven solely by paracrine signaling between tumor and endothelial cells in a spatially-relevant manner, it is expected that this system

will provide a more clinically-translatable drug response. However, it is important to recognize the limitations of this system. The integration of additional stromal cells, such as fibroblasts, pericytes, and immune cells, may enhance angiogenic activity, influencing the magnitude, rate, and duration of sprouting. Furthermore, the incorporation of flow will allow for analysis of the effect of shear stress on the development of angiogenic sprouting. Although our system does not allow for vascular flow, it is still practical as the tortuous nature of the *in vivo* tumor vasculature leads to many regions of static circulation where angiogenic sprouting may be more inclined to occur. Future studies will focus on incorporating further complexity into the *in vitro* tumor angiogenesis model as well as test the functionality of our system through blocking angiogenic sprouting with known inhibitors.

4.6 Conclusion

A principal distinction between conventional *in vitro* angiogenesis assays and angiogenesis development *in vivo* is that exogenous angiogenic growth factors interact with the apical surface of endothelial cells cultured *in vitro*, while during *in vivo* angiogenesis, paracrine signaling from adjacent tumor cells interact with the basal endothelial cell surface. To more accurately mimic *in vivo* angiogenesis, a co-culture *in vitro* tumor angiogenesis model was introduced with microvascular endothelial cells cultured as an endothelium on the surface of an acellular collagen I hydrogel under which MDA-MB-231 breast cancer cells were cultured in a separate collagen I hydrogel. Endothelial cells were shown to assemble into a capillary-like tubule network with lumen formation and anastomosing branches evident beneath the surface of the confluent monolayer. Angiogenic sprouting was stimulated in response to paracrine signaling between the tumor and endothelial cells in the absence of exogenous angiogenic factors, and the magnitude and rate of sprouting were dependent on endogenous VEGF secretion, matrix concentration, and duration of co-culture. This model may be well suited for conducting improved anti-angiogenesis drug screening in a controlled and reproducible manner.

4.7 Acknowledgements

We would like to thank Andrea Martin for generously donating the Sprague Dawley rat tails for collagen isolation. Funding for this study was provided by the National Science

Foundation Early CAREER Award CBET 0955072 and National Institute of Health grant 1R21CA158454-01A1.

4.8 References

1. Pepper MS, Ferrara N, Orci L, Montesano R. Potent synergism between vascular endothelial growth factor and basic fibroblast growth factor in the induction of angiogenesis in vitro. *Biochem Biophys Res Commun*. 1992 Dec 15;189(2):824-31.
2. Bikfalvi A. Significance of angiogenesis in tumour progression and metastasis. *Eur J Cancer*. 1995 Jul-Aug;31A(7-8):1101-4.
3. Cross MJ, Claesson-Welsh L. FGF and VEGF function in angiogenesis: signalling pathways, biological responses and therapeutic inhibition. *Trends Pharmacol Sci*. 2001 Apr;22(4):201-7.
4. Shojaei F, Ferrara N. Antiangiogenesis to treat cancer and intraocular neovascular disorders. *Lab Invest*. 2007 Mar;87(3):227-30.
5. Hanahan D, Weinberg RA. The hallmarks of cancer. *Cell*. 2000 Jan 7;100(1):57-70.
6. Naumov GN, Akslen LA, Folkman J. Role of angiogenesis in human tumor dormancy: animal models of the angiogenic switch. *Cell Cycle*. 2006 Aug;5(16):1779-87.
7. Brahim-Horn MC, Chiche J, Pouyssegur J. Hypoxia and cancer. *J Mol Med*. 2007 Dec;85(12):1301-7.
8. Sfiligoi C, de Luca A, Cascone I, Sorbello V, Fuso L, Ponzzone R, et al. Angiopoietin-2 expression in breast cancer correlates with lymph node invasion and short survival. *Int J Cancer*. 2003 Feb 10;103(4):466-74.
9. Kerbel RS. Tumor angiogenesis. *N Engl J Med*. 2008 May 8;358(19):2039-49.
10. Hanahan D, Folkman J. Patterns and emerging mechanisms of the angiogenic switch during tumorigenesis. *Cell*. 1996 Aug 9;86(3):353-64.
11. Folkman J. Tumor angiogenesis: therapeutic implications. *N Engl J Med*. 1971 Nov 18;285(21):1182-6.
12. Wu H, Huang C, Chang D. Anti-angiogenic therapeutic drugs for treatment of human cancer. *J Cancer Mol*. 2008;4(2):37-45.
13. Ferrara N, Kerbel RS. Angiogenesis as a therapeutic target. *Nature*. 2005 Dec 15;438(7070):967-74.

14. Shojaei F. Anti-angiogenesis therapy in cancer: current challenges and future perspectives. *Cancer Lett.* 2012 Jul 28;320(2):130-7.
15. Folkman J, Haudenschild C. Angiogenesis in vitro. *Nature.* 1980 Dec 11;288(5791):551-6.
16. Maciag T, Kadish J, Wilkins L, Stemerman MB, Weinstein R. Organizational behavior of human umbilical vein endothelial cells. *J Cell Biol.* 1982 Sep;94(3):511-20.
17. Montesano R, Orci L. Tumor-promoting phorbol esters induce angiogenesis in vitro. *Cell.* 1985 Sep;42(2):469-77.
18. Montesano R, Vassalli JD, Baird A, Guillemin R, Orci L. Basic fibroblast growth factor induces angiogenesis in vitro. *Proc Natl Acad Sci U S A.* 1986 Oct;83(19):7297-301.
19. Bikfalvi A, Sauzeau C, Moukadiri H, Maclouf J, Busso N, Bryckaert M, et al. Interaction of vasculotropin/vascular endothelial cell growth factor with human umbilical vein endothelial cells: binding, internalization, degradation, and biological effects. *J Cell Physiol.* 1991 Oct;149(1):50-9.
20. Mandriota SJ, Pepper MS. Vascular endothelial growth factor-induced in vitro angiogenesis and plasminogen activator expression are dependent on endogenous basic fibroblast growth factor. *J Cell Sci.* 1997 Sep;110 (Pt 18):2293-302.
21. van Hinsbergh VW, Collen A, Koolwijk P. Role of fibrin matrix in angiogenesis. *Ann N Y Acad Sci.* 2001;936:426-37.
22. Ghajar CM, Bissell MJ. Tumor engineering: the other face of tissue engineering. *Tissue Eng Part A.* 2010 Jul;16(7):2153-6.
23. Montesano R, Pepper MS, Orci L. Paracrine induction of angiogenesis in vitro by Swiss 3T3 fibroblasts. *J Cell Sci.* 1993 Aug;105 (Pt 4):1013-24.
24. Janvier R, Sourla A, Koutsilieris M, Doillon CJ. Stromal fibroblasts are required for PC-3 human prostate cancer cells to produce capillary-like formation of endothelial cells in a three-dimensional co-culture system. *Anticancer Res.* 1997 May-Jun;17(3A):1551-7.
25. Walter-Yohrling J, Pratt BM, Ledbetter S, Teicher BA. Myofibroblasts enable invasion of endothelial cells into three-dimensional tumor cell clusters: a novel in vitro tumor model. *Cancer Chemother Pharmacol.* 2003 Oct;52(4):263-9.

26. Chen Z, Htay A, Dos Santos W, Gillies GT, Fillmore HL, Sholley MM, et al. In vitro angiogenesis by human umbilical vein endothelial cells (HUVEC) induced by three-dimensional co-culture with glioblastoma cells. *J Neurooncol.* 2009 Apr;92(2):121-8.
27. Verbridge SS, Choi NW, Zheng Y, Brooks DJ, Stroock AD, Fischbach C. Oxygen-controlled three-dimensional cultures to analyze tumor angiogenesis. *Tissue Eng Part A.* 2010 Jul;16(7):2133-41.
28. Correa de Sampaio P, Auslaender D, Krubasik D, Failla AV, Skepper JN, Murphy G, et al. A heterogeneous in vitro three dimensional model of tumour-stroma interactions regulating sprouting angiogenesis. *PLoS One.* 2012;7(2):e30753.
29. Szot CS, Buchanan CF, Freeman JW, Rylander MN. 3D in vitro bioengineered tumors based on collagen I hydrogels. *Biomaterials.* 2011 Nov;32(31):7905-12.
30. Kebers F, Lewalle JM, Desreux J, Munaut C, Devy L, Foidart JM, et al. Induction of endothelial cell apoptosis by solid tumor cells. *Exp Cell Res.* 1998 May 1;240(2):197-205.
31. Szot CS, Buchanan CF, Gatenholm P, Rylander MN, Freeman JW. Investigation of cancer cell behaviour on nanofibrous scaffolds. *Materials Science and Engineering C.* 2011;31(1):37-42.
32. Erkan M, Reiser-Erkan C, Michalski CW, Deucker S, Sauliunaite D, Streit S, et al. Cancer-stellate cell interactions perpetuate the hypoxia-fibrosis cycle in pancreatic ductal adenocarcinoma. *Neoplasia.* 2009 May;11(5):497-508.
33. Cross VL, Zheng Y, Won Choi N, Verbridge SS, Sutermaister BA, Bonassar LJ, et al. Dense type I collagen matrices that support cellular remodeling and microfabrication for studies of tumor angiogenesis and vasculogenesis in vitro. *Biomaterials.* 2010 Nov;31(33):8596-607.
34. Buchanan CF, Szot CS, Wilson TD, Akman S, Metheny-Barlow LJ, Robertson JL, et al. Cross-talk between endothelial and breast cancer cells regulates reciprocal expression of angiogenic factors in vitro. *J Cell Biochem.* 2012 Apr;113(4):1142-1151.
35. Koziem D, Gerol M, Hendey B, RayChaudhury A. A novel in vitro model of tumor angiogenesis. *In Vitro Cell Dev Biol Anim.* 2000 Oct;36(9):555-8.
36. Venetsanakos E, Mirza A, Fanton C, Romanov SR, Tlsty T, McMahon M. Induction of tubulogenesis in telomerase-immortalized human microvascular endothelial cells by glioblastoma cells. *Exp Cell Res.* 2002 Feb 1;273(1):21-33.

37. Chung S, Sudo R, Mack PJ, Wan CR, Vickerman V, Kamm RD. Cell migration into scaffolds under co-culture conditions in a microfluidic platform. *Lab Chip*. 2009 Jan 21;9(2):269-75.

Chapter 5: Future Work

5.1 Immediate objective

5.1.1 Quantification of angiogenic sprouting

It will be necessary to determine a valid metric for quantifying angiogenic sprouting within the bilayered bioengineered tumor angiogenesis model before it can be used as a reliable drug screening tool. *In vitro* angiogenesis assays from the literature have reported mean sprout length beneath a surface monolayer [108, 109], # and length of sprouts from an endothelial coated bead [110] or tumor spheroid [95], and # of endothelial invasions/mm² [74]. While these are all valid metrics, measuring sprout length or counting the number of invasions will be challenging within this system as sprouting from the co-culture groups was often random and chaotic, making it difficult to distinguish between separate points of invasion (Fig. 5.1). For this reason, angiogenic sprouting was qualitatively assessed in **Chapter 4**. This was sufficient as obvious and consistent trends were noticeable among the different groups.

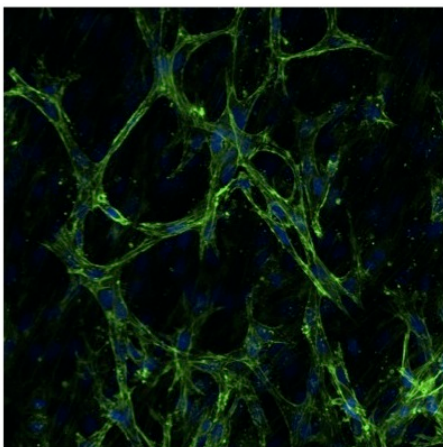


Figure 5.1. Angiogenic sprouting beneath the surface endothelial monolayer when co-cultured on the MDA-MB-231 bioengineered tumors. Sprouting is random and chaotic, which makes it difficult to quantify.

Another challenge that must be addressed while determining an appropriate metric for quantitative analysis is the contour of the acellular collagen layer, which is not flat but slightly concave. By allowing a fraction of the collagen solution to polymerize before adding the remaining volume, the naturally occurring meniscus that formed within the transwell insert was minimized. However, the endothelial monolayer cultured on the surface of the acellular collagen layer was still slightly curved, which made imaging difficult. The only way to visualize angiogenic sprouting within the bilayered bioengineered tumor co-culture setup is to use

confocal microscopy to focus beneath the surface. Without a completely flat surface, it was not possible to obtain images from the entire sample for quantitative analysis. This issue was frustrating as meniscus formation was more prominent with the lower concentrations of collagen (2 mg/ml), where the degree of sprouting was greatest. To address this, glass coverslips are now placed on the surface of the collagen hydrogel solution during polymerization to produce a flat surface. Specifically, 12 mm diameter glass coverslips (the diameter of the 12-well transwell insert is 12 mm) have been attached to 20 μ l pipette tips to allow for placement and removal of the coverslips (Fig. 5.2a). Since the diameter of the coverslips is an exact match to the diameter of the transwell insert, a small portion of the coverslip has to be removed with a sanding machine to allow for air to escape when the coverslip is placed onto the collagen solution. Although this works well for the higher concentrations of collagen (8 mg/ml), the coverslips sank when first placed on the lower concentrations of collagen (2 mg/ml). By reducing the volume of the solution, the surface tension of the collagen is now sufficient to support the coverslips, allowing the acellular collagen to form a flat surface (Fig. 5.2b).

While imaging angiogenic sprouting within the acellular collagen layer has been greatly improved by creating a completely flat surface, a valid metric for quantifying angiogenic sprouting still needs to be determined. One approach attempted was to trypsinize the endothelial

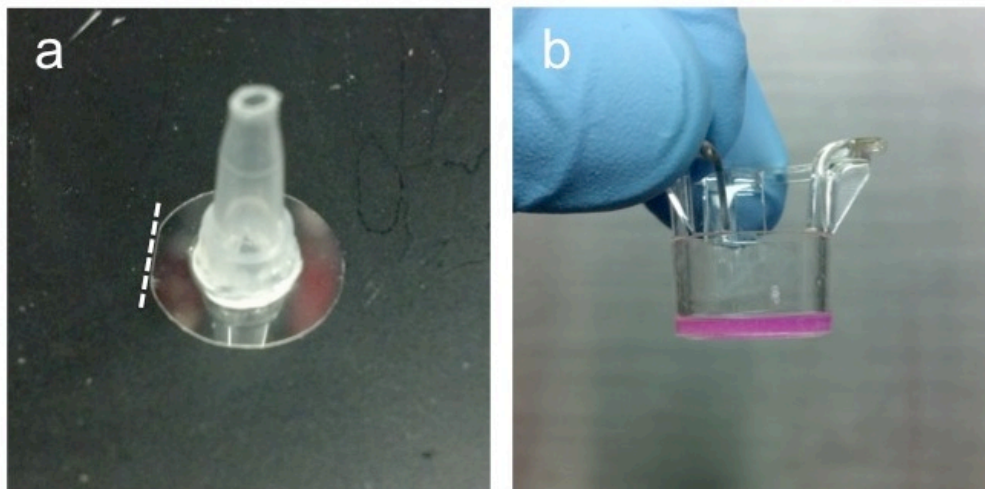


Figure 5.2. a) Glass coverslip used to create a flat surface on the collagen hydrogel during polymerization. The dotted line highlights where a portion was sanded away to allow air to escape. b) Collagen hydrogel within the transwell insert with a completely flat surface.

monolayer on the surface in order to leave only the endothelial cells that had successfully invaded into the underlying collagen matrix, similar to another group that had used a fibrin hydrogel matrix [111]. However, after 10 min of incubation with 0.25% trypsin, the entire endothelial monolayer was still attached to the collagen surface. Another idea is to grade angiogenic sprouting through blind assessment using a generic scale, similar to histological grading. Although this is not a true quantitative measurement, it may be more appropriate than trying to measure accurate sprout lengths and number of invasions from the images obtained. Finally, commercially available software, such as S.CORE web-based image analysis, can be purchased to assess angiogenic sprouting. However, these types of software are expensive and may not be able to accurately distinguish between individual tubules from the chaotic sprouting observed within this system.

5.1.2 Fibroblast co-culture

Incorporating additional stromal cell types into the existing *in vitro* tumor model will be necessary in order to further expand the complexity and accuracy of the system. While immune cells and mural cells play important roles within the tumor microenvironment, fibroblasts should be integrated next as they are the most prevalent stromal cell type, responsible for remodeling the matrix, stimulating cancer cell proliferation, and enhancing neovascularization [4, 48]. Fibroblasts have been co-cultured previously with tumor and endothelial cells within hydrogel-based *in vitro* tumor models, providing an angiogenic stimulus that was necessary in order to achieve angiogenic sprouting [95, 112, 113]. Co-culturing fibroblasts within the bilayered bioengineered tumor angiogenesis model, which has already demonstrated tumor-endothelial cell induced *in vitro* angiogenesis, will allow us to isolate the additive influence that fibroblasts have on angiogenic sprouting, effectively decoupling the angiogenic-specific role of fibroblasts from tumor cells. This has been briefly highlighted in a recent study where tumor spheroids containing either fibroblasts and endothelial cells or tumor cells, fibroblasts, and endothelial cells were treated with angiogenic inhibitors. A neutralizing antibody targeting interleukin (IL)-8 was shown to reduce sprouting from the spheroids containing tumor cells to the same level as the fibroblast-endothelial cell spheroids, demonstrating that IL-8 is an angiogenic promoter expressed by the tumor cells but not by the fibroblasts [95].

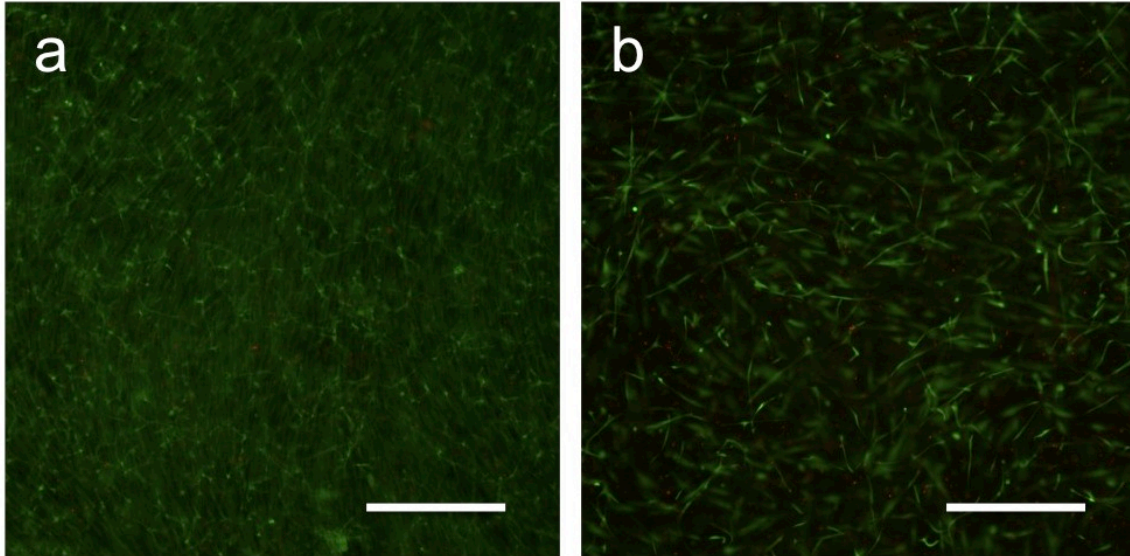


Figure 5.3. Live/Dead stain on day 7 of NHDFs cultured within a collagen hydrogel a) without and b) with prior mitomycin-C treatment. a) The NHDFs proliferated to such a great extent that the entire surface of the hydrogel was covered in a confluent monolayer of NHDFs. However, there was no indication of matrix compaction from either group. Green, live cells stained with calcein AM; red, dead cells stained with propidium iodide. Scale bars represent 500 μm .

5.1.2.1 Preliminary results

An initial concern regarding culturing fibroblasts within collagen hydrogels was matrix compaction. MRC-5 normal lung fibroblasts were previously cultured within 8 mg/ml collagen hydrogels at a seeding density of 1×10^6 cells/ml, resulting in noticeable compaction following 4 days in culture (data not available). More recently, primary neonatal human dermal fibroblasts (NHDF) were cultured within 8 mg/ml collagen hydrogels at a seeding density of 1×10^6 cells/ml. At the advice of Dr. Chris Roberts, the NHDFs were incubated in 50 $\mu\text{g/ml}$ of mitomycin-C for 30 min prior to seeding in an effort to prevent matrix compaction. While the function of mitomycin-C is to crosslink DNA, which inhibits DNA replication, Dr. Robert's group has had success previously in preventing matrix compaction when treating fibroblasts with mitomycin-C. Perhaps there is a cell density threshold at which compaction starts to have a noticeable effect on the matrix, and the anti-proliferative influence of mitomycin-C ensures that this threshold is never reached. Following 7 days in culture, collagen hydrogels containing NHDFs with and without mitomycin-C treatment showed no signs of matrix compaction (Fig. 5.3).

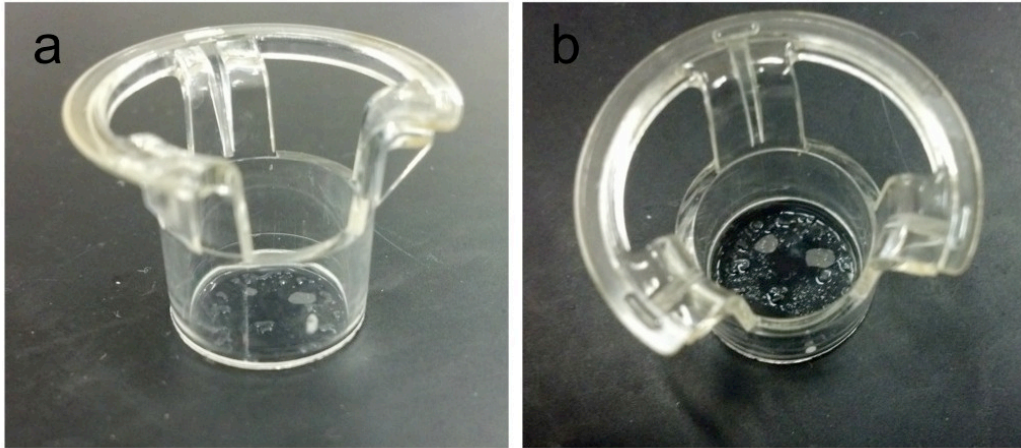


Figure 5.4. The NHDF collagen hydrogels after 1 day of co-culture with TIME cells from the a) side and b) top view. All that remained were small fragments of the hydrogel.

In view of this, fibroblast-endothelial and tumor-fibroblast-endothelial co-cultures were setup similar to the tumor-endothelial cell groups from **Chapter 4**. Specifically, NHDFs with and without MDA-MB-231 cells were cultured within 8 mg/ml collagen hydrogels at a seeding density of 1×10^6 cells/ml for each cell type, and telomerase-immortalized human microvascular endothelial (TIME) cells were seeded on the surface of a 2 mg/ml acellular collagen layer 24 h later at a seeding density of 3×10^4 cells/mm². Complete endothelial growth medium was provided to the TIME cells cultured within the inserts, and complete fibroblast growth medium was provided to the wells. After 1 day of co-culture with the TIME cells, the hydrogels from both groups were no longer whole but reduced to small fragments (Fig. 5.4). In an attempt to alleviate this issue, the NHDF seeding density was reduced to 5×10^5 cells/ml and the NHDFs were treated with mitomycin-C. After 1 day of co-culture with the TIME cells, the fibroblast-endothelial hydrogels were at approximately half of the original volume with a noticeable change in structure (the hydrogels were softer), suggesting that an endothelial cell-mediated upregulation in protease activity may be the issue. When the NHDF seeding density was further reduced to 2.5×10^5 cells/ml with mitomycin-C treatment and co-cultured with MDA-MB-231 cells at 1×10^6 cells/ml, no reduction in hydrogel volume was observed up to 5 days after co-culture with the TIME cells. Both the NHDF and MDA-MB-231 cells appeared normal when stained with Oregon Green® 488 phalloidin, and invasive angiogenic sprouting with capillary-like tubule formation was observed beneath the surface endothelial monolayer (Fig. 5.5).

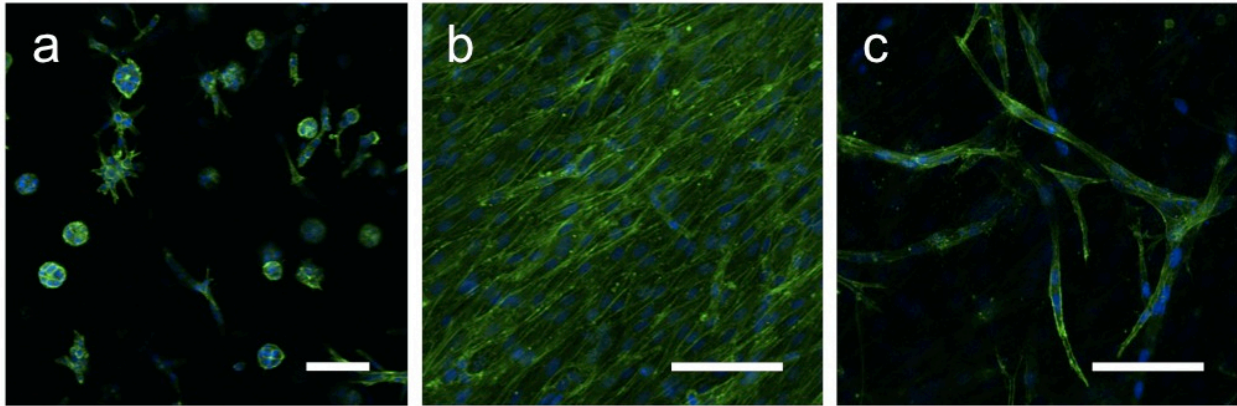


Figure 5.5. The tumor-fibroblast-endothelial cell hydrogels after 7 days of co-culture gave no indication of volume reduction. a) The NHDFs displayed extended morphologies throughout the collagen matrix, as observed in Fig. 5.3, and the MDA-MB-231 cells formed small aggregates. b) TIME cells reached confluence and c) began to invasively sprout beneath the surface forming capillary-like tubules. Green, f-actin; blue, nuclei. Scale bars represent 100 μm .

Although the initial issues hindering fibroblast co-culture with the TIME cells appear to be solved after several trial and error attempts at altering the seeding densities and ratio, the cause of the volume reduction still needs to be determined. There are two possible explanations that have begun to be investigated – matrix compaction by the NHDFs following activation to myofibroblasts and significant matrix metalloproteinase (MMP) secretion by the NHDFs. While it has been reported that tumor cells, in particular breast cancer cells, have the ability to activate fibroblasts through transforming growth factor- β 1 paracrine signaling [114-116] as well as stimulate fibroblast expression of MMPs [117, 118], our results suggest that endothelial cells may also play a role in influencing fibroblast activity. For these preliminary experiments, TIME cells were cultured on 12-well costar transwell inserts with 0.4 μm pore polyester membranes and NHDFs were cultured below in the 12-well dish. On days 1 and 3, NHDFs were either stained for α -smooth muscle actin (SMA), a marker of fibroblast activation, or the NHDF RNA was isolated for quantitative reverse transcription polymerase chain reaction (qRT-PCR). α -SMA was expressed at similar levels from both groups (NHDFs cultured alone and NHDFs co-cultured with the TIME cells) (data not shown), implying that fibroblasts are not activated to myofibroblasts as a result of co-culture with endothelial cells in a two-dimensional setting. Therefore, matrix compaction as a result of fibroblast activation may not be the cause of the observed hydrogel volume reduction. For the qRT-PCR experiment, the cycle thresholds for

MMP9 expression from both groups was high (> 37) on day 1, indicating that the NHDF basal levels of MMP9 mRNA are low. Because of this, there was too much variability in the cycle thresholds to generate reliable data. However, there were obvious trends; specifically, the cycle thresholds for MMP9 from the co-culture group decreased considerably from day 1 to day 3, and the cycle thresholds from the co-culture group were noticeably lower than the control NHDF group on day 3. These observations suggest that MMP9 expression from the co-culture NHDFs may have increased from day 1 to day 3, and the day 3 expression levels were likely higher than the control group.

Additional work is needed to confirm these assumptions as well as measure the expression of other MMPs, such as MMP2 and MMP13, which are exclusively expressed by stromal fibroblasts [117, 118]. Furthermore, now that all three cell types (tumor cells, fibroblasts, and endothelial cells) can be successfully co-cultured within the bilayered bioengineered tumor model, it is necessary to begin characterizing the influence of fibroblasts on angiogenic sprouting.

5.1.3 Screening of angiogenesis inhibitors

The ultimate goal of this project is to develop a three-dimensional *in vitro* tumor model that can serve as a reliable tool for accurate evaluation and refinement of anti-angiogenic therapies. Similar hydrogel-based *in vitro* tumor models have previously demonstrated inhibition of angiogenic sprouting in response to known angiogenesis blockers, including neutralizing antibodies and receptor tyrosine kinase inhibitors (TKIs) [95, 110, 113]. In particular, a recent study reported significantly different responses to angiogenic inhibitors between spheroids embedded in a collagen hydrogel containing either fibroblasts and endothelial cells or tumor cells, fibroblasts, and endothelial cells [95]. As mentioned in the previous sub-section, a neutralizing antibody targeting IL-8 was shown to reduce sprouting from the spheroids containing tumor cells, fibroblasts, and endothelial cells but not from the spheroids containing only fibroblasts and endothelial cells. In addition, endostatin and thalidomine were only shown to reduce angiogenic sprouting from the fibroblast-endothelial spheroids. These results emphasize the importance of screening angiogenesis inhibitors within complex *in vitro* tumor angiogenesis models, as these systems can successfully isolate the angiogenic-specific role of different cell types within the tumor microenvironment. However, as discussed in **Chapter 4**,

these systems relied on exogenous stimuli and inaccurate culturing conditions to induce an angiogenic response. Therefore, the conclusions drawn from those studies may be unreliable in an *in vivo* setting and should be validated using a more physiologically-accurate *in vitro* tumor model.

We have conducted preliminary experiments using a neutralizing antibody targeting vascular endothelial growth factor (VEGF). Specifically, a human VEGF monoclonal antibody was supplied to TIME cells cultured on the surface of the bilayered bioengineered tumors at a concentration of 500 ng/ml every 24 h for 7 days. Our results varied significantly, with sprouting successfully inhibited during only 1 of 3 sets of experiments (data not shown). This was likely due to variability in VEGF secretion from the MDA-MB-231 cells. For the set of experiments where angiogenic sprouting was inhibited, the concentration of the VEGF antibody was sufficient for neutralizing the endogenous VEGF secretion. However, since the concentration of VEGF required to induce an angiogenic response was determined to be ~10 ng/ml (from **Chapter 4**), any positive variability in VEGF secretion may be enough to outweigh the neutralizing antibody. When planning future experiments, a wide range of antibody/TKI concentrations should be tested, and each set of experiments should contain a control group due to experimental variability.

Additional inhibitors that should be screened include neutralizing antibodies targeting IL-8 and platelet-derived growth factor (PDGF), TKIs, such as SU4312 and SU6668, and endogenous anti-angiogenic inhibitors, including endostatin, thrombospondin-1, and angiostatin. While these inhibitors are frequently used throughout the literature, the bilayered bioengineered tumor angiogenesis model provides a more physiologically-accurate co-culture setup that allows for inexpensive, easy, and reproducible testing of multiple inhibitors either individually or in different combinations. Furthermore, the transwell co-culture setup allows for angiogenic inhibitors to be supplied to both the apical and basal surfaces of the endothelial monolayer. This may provide useful information about receptor localization, which is not well known [119] and is important to consider when planning treatment regimens. Differences in apical and basal stimulation have been reported previously in a study where pro-angiogenic conditioned medium supplied to endothelial cells cultured on collagen hydrogels only induced an angiogenic response when injected into the hydrogel where it could interact with the basal surface [120]. Conditioned medium provided to the apical surface was not shown to have an effect. Bioengineered tumors

cultured with other cancer types, such as brain and pancreatic, can be screened as well to determine which inhibitors are most appropriate for different types of cancer.

5.2 Long term objective

There are two areas where this project can be expanded in the future: 1) incorporating additional layers of complexity to the existing *in vitro* tumor model and 2) comparing angiogenic inhibitor response to *in vivo* mouse models. Besides other cell types, as discussed above, the acellular collagen layer can be replaced with a more accurate representation of the basement membrane, such as varying mixtures of laminin and collagen IV. Specifically, laminin has an active role within the tumor microenvironment, influencing cell survival and invasion [121, 122]. This model can also be adapted to allow for microfluidic flow. While the tortuous nature of the *in vivo* tumor vasculature leads to many regions of static circulation where angiogenic sprouting may be more inclined to occur, aberrant blood flow, chaotic branching, uneven vessel lumens, vascular shunts, and increased vessel permeability also influence angiogenic sprouting and the response/resistance to angiogenic inhibitors [2, 64, 65]. A microfluidic model for studying the influence of shear stress on tumor angiogenesis is currently being developed in our lab. In the future, expertise from both projects can be combined to develop a tortuous microfluidic tumor angiogenesis model for more realistic drug screening.

In the *Clinical significance* section from **Chapter 1** I mentioned that although it is unlikely these *in vitro* tumor models will reach a level of complexity that will allow them to completely replace *in vivo* models, they can serve as powerful tools for the accurate evaluation and refinement of therapies before investing significant time and money in conducting *in vivo* animal trials. Comparing the angiogenic inhibitor response of the bilayered bioengineered tumor angiogenesis model to *in vivo* mouse models will determine whether this statement is valid. The expectation is that effective doses and combinations of angiogenic inhibitors can be more accurately judged during *in vitro* preclinical experiments, leading to higher *in vivo* success rates and a greater percentage of drugs receiving FDA approval.

5.3 Conclusions

According to the National Cancer Institute, the U.S. cancer death rate has been declining since 1994 from 211.76 deaths per 100,000 people to 175.86 deaths per 100,000 people in 2008. This improved death rate is approaching the Department of Health and Human Services “Healthy People Target” of 160.6 cancer deaths per 100,000 people by 2020. While this emphasizes the advances being made in cancer research over the last couple of decades and is encouraging for individuals diagnosed with this disease, the financial costs of cancer care have been steadily increasing with the national cancer care expenditures in 2010 estimated to be \$124.6 billion. One area of cancer research that can reduce the financial burden of cancer while identifying more effective anti-cancer agents for improving the death rate is the development of more physiologically-relevant *in vitro* tumor models for preclinical drug screening prior to *in vivo* animal and human clinical trials.

Throughout this project, my goal has been to develop an improved three-dimensional *in vitro* tumor model. This began with investigating cancer cell growth on several different types of scaffolds. After deciding to take a hydrogel-based approach, aggressive breast cancer cells cultured within a collagen I hydrogel matrix were shown to mimic important characteristics of the *in vivo* tumor microenvironment. Specifically, limitations in oxygen diffusion and competition for nutrients forced the cells to experience hypoxia and undergo necrosis, resulting in a significant upregulation of VEGF expression. Microvascular endothelial cells cultured on the surface of the designated pro-angiogenic “bioengineered tumors” displayed a pronounced angiogenic response in the absence of exogenous angiogenic stimuli. The co-cultured endothelial cells demonstrated a significant increase in proliferation, rapidly developed an elongated morphology, and invasively sprouted into the underlying collagen matrix, forming a capillary-like tubule network. With the incorporation of fibroblasts and the determination of a valid angiogenic sprouting quantification metric, my hope is that the bilayered bioengineered tumor angiogenesis model will provide a more physiologically-relevant response to angiogenesis inhibitors that can be clinically-translatable in the future.

References

1. Brahim-Horn MC, Chiche J, Pouyssegur J. Hypoxia and cancer. *J Mol Med*. 2007 Dec;85(12):1301-7.
2. Tredan O, Galmarini CM, Patel K, Tannock IF. Drug resistance and the solid tumor microenvironment. *J Natl Cancer Inst*. 2007 Oct 3;99(19):1441-54.
3. Hanahan D, Weinberg RA. The hallmarks of cancer. *Cell*. 2000 Jan 7;100(1):57-70.
4. Kalluri R, Zeisberg M. Fibroblasts in cancer. *Nat Rev Cancer*. 2006 May;6(5):392-401.
5. Black WC, Welch HG. Advances in diagnostic imaging and overestimations of disease prevalence and the benefits of therapy. *N Engl J Med*. 1993 Apr 29;328(17):1237-43.
6. Naumov GN, Akslen LA, Folkman J. Role of angiogenesis in human tumor dormancy: animal models of the angiogenic switch. *Cell Cycle*. 2006 Aug;5(16):1779-87.
7. Bikfalvi A. Significance of angiogenesis in tumour progression and metastasis. *Eur J Cancer*. 1995 Jul-Aug;31A(7-8):1101-4.
8. Hanahan D, Folkman J. Patterns and emerging mechanisms of the angiogenic switch during tumorigenesis. *Cell*. 1996 Aug 9;86(3):353-64.
9. Weinberg RA. *The Biology of Cancer*. New York: Garland Science; 2007.
10. National Cancer Institute. [cited 2012]; Available from: <http://www.cancer.gov>.
11. Colston JAC. SURGICAL REMOVAL OF CANCER OF THE PROSTATE GLAND. *JAMA*. 1945;127(2):69-74.
12. Stock CC. Aspects of approaches in experimental cancer chemotherapy. *The American journal of medicine*. 1950 May;8(5):658-74.
13. Roswit B, Patno ME, Rapp R, Veinbergs A, Feder B, Stuhlberg J, et al. The survival of patients with inoperable lung cancer: a large-scale randomized study of radiation therapy versus placebo. *Radiology*. [Clinical Trial Randomized Controlled Trial]. 1968 Apr;90(4):688-97.
14. Kennedy BJ, Nathanson IT. EFFECTS OF INTENSIVE SEX STEROID HORMONE THERAPY IN ADVANCED BREAST CANCER. *JAMA*. 1953;152(12):1135-1141.
15. Burkhardt D, Ghosh P. Hyperthermia and cancer. *The Australian and New Zealand journal of surgery*. 1977 Oct;47(5):571-6.

16. Zbar B, Bernstein ID, Bartlett GL, Hanna MG, Jr., Rapp HJ. Immunotherapy of cancer: regression of intradermal tumors and prevention of growth of lymph node metastases after intralesional injection of living *Mycobacterium bovis*. *J Natl Cancer Inst.* 1972 Jul;49(1):119-30.
17. Roth JA, Cristiano RJ. Gene therapy for cancer: what have we done and where are we going? *J Natl Cancer Inst.* [Research Support, Non-U.S. Gov't Research Support, U.S. Gov't, P.H.S. Review]. 1997 Jan 1;89(1):21-39.
18. Folkman J. Tumor angiogenesis: therapeutic implications. *N Engl J Med.* 1971 Nov 18;285(21):1182-6.
19. Leaf C. Why We're Losing The War On Cancer (And How To Win It). *Fortune.* 2004:77-92.
20. Kola I, Landis J. Can the pharmaceutical industry reduce attrition rates? *Nat Rev Drug Discov.* 2004 Aug;3(8):711-5.
21. Rangarajan A, Hong SJ, Gifford A, Weinberg RA. Species- and cell type-specific requirements for cellular transformation. *Cancer Cell.* 2004 Aug;6(2):171-83.
22. Voskoglou-Nomikos T, Pater JL, Seymour L. Clinical predictive value of the in vitro cell line, human xenograft, and mouse allograft preclinical cancer models. *Clin Cancer Res.* 2003 Sep 15;9(11):4227-39.
23. Kelland LR. Of mice and men: values and liabilities of the athymic nude mouse model in anticancer drug development. *Eur J Cancer.* 2004 Apr;40(6):827-36.
24. Sivaraman A, Leach JK, Townsend S, Iida T, Hogan BJ, Stolz DB, et al. A microscale in vitro physiological model of the liver: predictive screens for drug metabolism and enzyme induction. *Curr Drug Metab.* 2005 Dec;6(6):569-91.
25. Rangarajan A, Weinberg RA. Opinion: Comparative biology of mouse versus human cells: modelling human cancer in mice. *Nat Rev Cancer.* 2003 Dec;3(12):952-9.
26. Yamada KM, Cukierman E. Modeling tissue morphogenesis and cancer in 3D. *Cell.* 2007 Aug 24;130(4):601-10.
27. Sharpless NE, Depinho RA. The mighty mouse: genetically engineered mouse models in cancer drug development. *Nat Rev Drug Discov.* 2006 Sep;5(9):741-54.

28. Fischbach C, Kong HJ, Hsiong SX, Evangelista MB, Yuen W, Mooney DJ. Cancer cell angiogenic capability is regulated by 3D culture and integrin engagement. *Proc Natl Acad Sci U S A*. [Research Support, N.I.H., Extramural Research Support, Non-U.S. Gov't]. 2009 Jan 13;106(2):399-404.
29. Kim JB, Stein R, O'Hare MJ. Three-dimensional in vitro tissue culture models of breast cancer-- a review. *Breast Cancer Res Treat*. 2004 Jun;85(3):281-91.
30. Pampaloni F, Reynaud EG, Stelzer EH. The third dimension bridges the gap between cell culture and live tissue. *Nat Rev Mol Cell Biol*. 2007 Oct;8(10):839-45.
31. Griffith LG, Swartz MA. Capturing complex 3D tissue physiology in vitro. *Nat Rev Mol Cell Biol*. 2006 Mar;7(3):211-24.
32. Durand RE, Sutherland RM. Effects of intercellular contact on repair of radiation damage. *Exp Cell Res*. 1972 Mar;71(1):75-80.
33. Hutmacher DW, Loessner D, Rizzi S, Kaplan DL, Mooney DJ, Clements JA. Can tissue engineering concepts advance tumor biology research? *Trends Biotechnol*. 2010 Mar;28(3):125-33.
34. Ghajar CM, Bissell MJ. Tumor engineering: the other face of tissue engineering. *Tissue Eng Part A*. 2010 Jul;16(7):2153-6.
35. Vaupel P, Mayer A. Hypoxia in cancer: significance and impact on clinical outcome. *Cancer Metastasis Rev*. 2007 Jun;26(2):225-39.
36. O'Reilly MS, Holmgren L, Chen C, Folkman J. Angiostatin induces and sustains dormancy of human primary tumors in mice. *Nat Med*. 1996 Jun;2(6):689-92.
37. Brown JM, Wilson WR. Exploiting tumour hypoxia in cancer treatment. *Nat Rev Cancer*. 2004 Jun;4(6):437-47.
38. Zhou J, Schmid T, Schnitzer S, Brune B. Tumor hypoxia and cancer progression. *Cancer Lett*. 2006 Jun 8;237(1):10-21.
39. Vaupel P, Mayer A, Hockel M. Tumor hypoxia and malignant progression. *Methods Enzymol*. 2004;381:335-54.
40. Yuan J, Narayanan L, Rockwell S, Glazer PM. Diminished DNA repair and elevated mutagenesis in mammalian cells exposed to hypoxia and low pH. *Cancer Res*. 2000 Aug 15;60(16):4372-6.

41. Ronnov-Jessen L, Bissell MJ. Breast cancer by proxy: can the microenvironment be both the cause and consequence? *Trends Mol Med*. 2009 Jan;15(1):5-13.
42. Dvorak HF. Tumors: wounds that do not heal. Similarities between tumor stroma generation and wound healing. *N Engl J Med*. 1986 Dec 25;315(26):1650-9.
43. Elenbaas B, Weinberg RA. Heterotypic signaling between epithelial tumor cells and fibroblasts in carcinoma formation. *Exp Cell Res*. 2001 Mar 10;264(1):169-84.
44. Kim JB. Three-dimensional tissue culture models in cancer biology. *Semin Cancer Biol*. 2005 Oct;15(5):365-77.
45. Ronnov-Jessen L, Petersen OW, Bissell MJ. Cellular changes involved in conversion of normal to malignant breast: importance of the stromal reaction. *Physiol Rev*. 1996 Jan;76(1):69-125.
46. Sappino AP, Skalli O, Jackson B, Schurch W, Gabbiani G. Smooth-muscle differentiation in stromal cells of malignant and non-malignant breast tissues. *Int J Cancer*. 1988 May 15;41(5):707-12.
47. Ronnov-Jessen L, Petersen OW, Kotliansky VE, Bissell MJ. The origin of the myofibroblasts in breast cancer. Recapitulation of tumor environment in culture unravels diversity and implicates converted fibroblasts and recruited smooth muscle cells. *J Clin Invest*. 1995 Feb;95(2):859-73.
48. Olumi AF, Grossfeld GD, Hayward SW, Carroll PR, Tlsty TD, Cunha GR. Carcinoma-associated fibroblasts direct tumor progression of initiated human prostatic epithelium. *Cancer Res*. 1999 Oct 1;59(19):5002-11.
49. Crowther M, Brown NJ, Bishop ET, Lewis CE. Microenvironmental influence on macrophage regulation of angiogenesis in wounds and malignant tumors. *J Leukoc Biol*. 2001 Oct;70(4):478-90.
50. Soucek L, Lawlor ER, Soto D, Shchors K, Swigart LB, Evan GI. Mast cells are required for angiogenesis and macroscopic expansion of Myc-induced pancreatic islet tumors. *Nat Med*. 2007 Oct;13(10):1211-8.
51. Rajput AB, Turbin DA, Cheang MC, Voduc DK, Leung S, Gelmon KA, et al. Stromal mast cells in invasive breast cancer are a marker of favourable prognosis: a study of 4,444 cases. *Breast Cancer Res Treat*. 2008 Jan;107(2):249-57.

52. Levental KR, Yu H, Kass L, Lakins JN, Egeblad M, Erler JT, et al. Matrix crosslinking forces tumor progression by enhancing integrin signaling. *Cell*. 2009 Nov 25;139(5):891-906.
53. Paszek MJ, Zahir N, Johnson KR, Lakins JN, Rozenberg GI, Gefen A, et al. Tensional homeostasis and the malignant phenotype. *Cancer Cell*. 2005 Sep;8(3):241-54.
54. Jodele S, Blavier L, Yoon JM, DeClerck YA. Modifying the soil to affect the seed: role of stromal-derived matrix metalloproteinases in cancer progression. *Cancer Metastasis Rev*. 2006 Mar;25(1):35-43.
55. Aznavoorian S, Moore BA, Alexander-Lister LD, Hallit SL, Windsor LJ, Engler JA. Membrane type I-matrix metalloproteinase-mediated degradation of type I collagen by oral squamous cell carcinoma cells. *Cancer Res*. 2001 Aug 15;61(16):6264-75.
56. Nagase H, Woessner JF, Jr. Matrix metalloproteinases. *J Biol Chem*. 1999 Jul 30;274(31):21491-4.
57. Park JE, Keller GA, Ferrara N. The vascular endothelial growth factor (VEGF) isoforms: differential deposition into the subepithelial extracellular matrix and bioactivity of extracellular matrix-bound VEGF. *Mol Biol Cell*. 1993 Dec;4(12):1317-26.
58. Kerbel RS. Tumor angiogenesis: past, present and the near future. *Carcinogenesis*. 2000 Mar;21(3):505-15.
59. Tolsma SS, Volpert OV, Good DJ, Frazier WA, Polverini PJ, Bouck N. Peptides derived from two separate domains of the matrix protein thrombospondin-1 have anti-angiogenic activity. *J Cell Biol*. 1993 Jul;122(2):497-511.
60. O'Reilly MS, Holmgren L, Shing Y, Chen C, Rosenthal RA, Moses M, et al. Angiostatin: a novel angiogenesis inhibitor that mediates the suppression of metastases by a Lewis lung carcinoma. *Cell*. 1994 Oct 21;79(2):315-28.
61. O'Reilly MS, Boehm T, Shing Y, Fukai N, Vasios G, Lane WS, et al. Endostatin: an endogenous inhibitor of angiogenesis and tumor growth. *Cell*. 1997 Jan 24;88(2):277-85.
62. Carmeliet P. Mechanisms of angiogenesis and arteriogenesis. *Nat Med*. 2000 Apr;6(4):389-95.
63. Cross MJ, Claesson-Welsh L. FGF and VEGF function in angiogenesis: signalling pathways, biological responses and therapeutic inhibition. *Trends Pharmacol Sci*. 2001 Apr;22(4):201-7.

64. Relf M, LeJeune S, Scott PA, Fox S, Smith K, Leek R, et al. Expression of the angiogenic factors vascular endothelial cell growth factor, acidic and basic fibroblast growth factor, tumor growth factor beta-1, platelet-derived endothelial cell growth factor, placenta growth factor, and pleiotrophin in human primary breast cancer and its relation to angiogenesis. *Cancer Res.* 1997 Mar 1;57(5):963-9.
65. Carmeliet P, Jain RK. Molecular mechanisms and clinical applications of angiogenesis. *Nature.* 2011 May 19;473(7347):298-307.
66. Kilarski WW, Bikfalvi A. Recent developments in tumor angiogenesis. *Curr Pharm Biotechnol.* 2007 Feb;8(1):3-9.
67. Sivridis E, Giatromanolaki A, Koukourakis MI. The vascular network of tumours--what is it not for? *J Pathol.* 2003 Oct;201(2):173-80.
68. Kerbel R, Folkman J. Clinical translation of angiogenesis inhibitors. *Nat Rev Cancer.* 2002 Oct;2(10):727-39.
69. Suuronen EJ, Sheardown H, Newman KD, McLaughlin CR, Griffith M. Building in vitro models of organs. *Int Rev Cytol.* 2005;244:137-73.
70. Baker BM, Chen CS. Deconstructing the third dimension: how 3D culture microenvironments alter cellular cues. *J Cell Sci.* 2012 Jul 1;125(Pt 13):3015-24.
71. Hutmacher DW, Horch RE, Loessner D, Rizzi S, Sieh S, Reichert JC, et al. Translating tissue engineering technology platforms into cancer research. *J Cell Mol Med.* 2009 Aug;13(8A):1417-27.
72. Ghosh S, Spagnoli GC, Martin I, Ploegert S, Demougin P, Heberer M, et al. Three-dimensional culture of melanoma cells profoundly affects gene expression profile: a high density oligonucleotide array study. *J Cell Physiol.* 2005 Aug;204(2):522-31.
73. Szot CS, Buchanan CF, Freeman JW, Rylander MN. 3D in vitro bioengineered tumors based on collagen I hydrogels. *Biomaterials.* 2011;Article in Press.
74. Verbridge SS, Choi NW, Zheng Y, Brooks DJ, Stroock AD, Fischbach C. Oxygen-controlled three-dimensional cultures to analyze tumor angiogenesis. *Tissue Eng Part A.* 2010 Jul;16(7):2133-41.
75. dit Faute MA, Laurent L, Ploton D, Poupon MF, Jardillier JC, Bobichon H. Distinctive alterations of invasiveness, drug resistance and cell-cell organization in 3D-cultures of MCF-7, a

- human breast cancer cell line, and its multidrug resistant variant. *Clin Exp Metastasis*. 2002;19(2):161-8.
76. St Croix B, Florenes VA, Rak JW, Flanagan M, Bhattacharya N, Slingerland JM, et al. Impact of the cyclin-dependent kinase inhibitor p27Kip1 on resistance of tumor cells to anticancer agents. *Nat Med*. 1996 Nov;2(11):1204-10.
77. Fischbach C, Chen R, Matsumoto T, Schmelzle T, Brugge JS, Polverini PJ, et al. Engineering tumors with 3D scaffolds. *Nat Methods*. 2007 Oct;4(10):855-60.
78. Horning JL, Sahoo SK, Vijayaraghavalu S, Dimitrijevic S, Vasir JK, Jain TK, et al. 3-D tumor model for in vitro evaluation of anticancer drugs. *Mol Pharm*. 2008 Sep-Oct;5(5):849-62.
79. Tannock IF, Lee CM, Tunggal JK, Cowan DS, Egorin MJ. Limited penetration of anticancer drugs through tumor tissue: a potential cause of resistance of solid tumors to chemotherapy. *Clin Cancer Res*. 2002 Mar;8(3):878-84.
80. Dalton WS. The tumor microenvironment as a determinant of drug response and resistance. *Drug Resist Updat*. 1999 Oct;2(5):285-288.
81. Morin PJ. Drug resistance and the microenvironment: nature and nurture. *Drug Resist Updat*. 2003 Aug;6(4):169-72.
82. Sethi T, Rintoul RC, Moore SM, MacKinnon AC, Salter D, Choo C, et al. Extracellular matrix proteins protect small cell lung cancer cells against apoptosis: a mechanism for small cell lung cancer growth and drug resistance in vivo. *Nat Med*. 1999 Jun;5(6):662-8.
83. Sutherland RM. Cell and environment interactions in tumor microregions: the multicell spheroid model. *Science*. 1988 Apr 8;240(4849):177-84.
84. Sutherland RM, Inch WR, McCredie JA, Kruuv J. A multi-component radiation survival curve using an in vitro tumour model. *International journal of radiation biology and related studies in physics, chemistry, and medicine*. 1970;18(5):491-5.
85. Unsworth BR, Lelkes PI. Growing tissues in microgravity. *Nat Med*. [Research Support, U.S. Gov't, Non-P.H.S. Review]. 1998 Aug;4(8):901-7.
86. Kunz-Schughart LA, Heyder P, Schroeder J, Knuechel R. A heterologous 3-D coculture model of breast tumor cells and fibroblasts to study tumor-associated fibroblast differentiation. *Exp Cell Res*. [Research Support, Non-U.S. Gov't]. 2001 May 15;266(1):74-86.

87. Becker JL, Prewett TL, Spaulding GF, Goodwin TJ. Three-dimensional growth and differentiation of ovarian tumor cell line in high aspect rotating-wall vessel: morphologic and embryologic considerations. *J Cell Biochem.* 1993 Mar;51(3):283-9.
88. Dhiman HK, Ray AR, Panda AK. Three-dimensional chitosan scaffold-based MCF-7 cell culture for the determination of the cytotoxicity of tamoxifen. *Biomaterials.* 2005 Mar;26(9):979-86.
89. Arya N, Sardana V, Saxena M, Rangarajan A, Katti DS. Recapitulating tumour microenvironment in chitosan-gelatin three-dimensional scaffolds: an improved in vitro tumour model. *J R Soc Interface.* 2012 Dec 7;9(77):3288-302.
90. Chen L, Xiao Z, Meng Y, Zhao Y, Han J, Su G, et al. The enhancement of cancer stem cell properties of MCF-7 cells in 3D collagen scaffolds for modeling of cancer and anti-cancer drugs. *Biomaterials.* 2012 Feb;33(5):1437-44.
91. Gurski LA, Jha AK, Zhang C, Jia X, Farach-Carson MC. Hyaluronic acid-based hydrogels as 3D matrices for in vitro evaluation of chemotherapeutic drugs using poorly adherent prostate cancer cells. *Biomaterials.* 2009 Oct;30(30):6076-85.
92. Xu X, Gurski LA, Zhang C, Harrington DA, Farach-Carson MC, Jia X. Recreating the tumor microenvironment in a bilayer, hyaluronic acid hydrogel construct for the growth of prostate cancer spheroids. *Biomaterials.* 2012 Dec;33(35):9049-60.
93. Talukdar S, Mandal M, Hutmacher DW, Russell PJ, Soekmadji C, Kundu SC. Engineered silk fibroin protein 3D matrices for in vitro tumor model. *Biomaterials.* 2011 Mar;32(8):2149-59.
94. Szot CS, Buchanan CF, Freeman JW, Rylander MN. 3D in vitro bioengineered tumors based on collagen I hydrogels. *Biomaterials.* 2011 Nov;32(31):7905-12.
95. Correa de Sampaio P, Auslaender D, Krubasik D, Failla AV, Skepper JN, Murphy G, et al. A heterogeneous in vitro three dimensional model of tumour-stroma interactions regulating sprouting angiogenesis. *PLoS One.* 2012;7(2):e30753.
96. Sahoo SK, Panda AK, Labhasetwar V. Characterization of porous PLGA/PLA microparticles as a scaffold for three dimensional growth of breast cancer cells. *Biomacromolecules.* 2005 Mar-Apr;6(2):1132-9.

97. Sieh S, Taubenberger AV, Rizzi SC, Sadowski M, Lehman ML, Rockstroh A, et al. Phenotypic characterization of prostate cancer LNCaP cells cultured within a bioengineered microenvironment. *PLoS One*. [Research Support, Non-U.S. Gov't]. 2012;7(9):e40217.
98. Ju YM, Choi JS, Atala A, Yoo JJ, Lee SJ. Bilayered scaffold for engineering cellularized blood vessels. *Biomaterials*. 2010 May;31(15):4313-21.
99. Backdahl H, Helenius G, Bodin A, Nannmark U, Johansson BR, Risberg B, et al. Mechanical properties of bacterial cellulose and interactions with smooth muscle cells. *Biomaterials*. 2006 Mar;27(9):2141-9.
100. Yazdani SK, Watts B, Machingal M, Jarajapu YP, Van Dyke ME, Christ GJ. Smooth muscle cell seeding of decellularized scaffolds: the importance of bioreactor preconditioning to development of a more native architecture for tissue-engineered blood vessels. *Tissue Eng Part A*. [Research Support, Non-U.S. Gov't]. 2009 Apr;15(4):827-40.
101. Saltzman WM. *Tissue Engineering: Principles for the Design of Replacement Organs and Tissues*. New York: Oxford University Press; 2004.
102. Lee KY, Mooney DJ. Hydrogels for tissue engineering. *Chem Rev*. 2001 Jul;101(7):1869-79.
103. Augst AD, Kong HJ, Mooney DJ. Alginate hydrogels as biomaterials. *Macromol Biosci*. 2006 Aug 7;6(8):623-33.
104. Kolacna L, Bakesova J, Varga F, Kostakova E, Planka L, Necas A, et al. Biochemical and biophysical aspects of collagen nanostructure in the extracellular matrix. *Physiol Res*. 2007;56 Suppl 1:S51-60.
105. Sottile J. Regulation of angiogenesis by extracellular matrix. *Biochim Biophys Acta*. 2004 Mar 4;1654(1):13-22.
106. Campbell NE, Kellenberger L, Greenaway J, Moorehead RA, Linnerth-Petrik NM, Petrik J. Extracellular matrix proteins and tumor angiogenesis. *J Oncol*. 2010;2010:586905.
107. Ala-aho R, Kahari VM. Collagenases in cancer. *Biochimie*. 2005 Mar-Apr;87(3-4):273-86.
108. Pepper MS, Ferrara N, Orci L, Montesano R. Potent synergism between vascular endothelial growth factor and basic fibroblast growth factor in the induction of angiogenesis in vitro. *Biochem Biophys Res Commun*. 1992 Dec 15;189(2):824-31.

109. Mandriota SJ, Pepper MS. Vascular endothelial growth factor-induced in vitro angiogenesis and plasminogen activator expression are dependent on endogenous basic fibroblast growth factor. *J Cell Sci.* 1997 Sep;110 (Pt 18):2293-302.
110. Chen Z, Htay A, Dos Santos W, Gillies GT, Fillmore HL, Sholley MM, et al. In vitro angiogenesis by human umbilical vein endothelial cells (HUVEC) induced by three-dimensional co-culture with glioblastoma cells. *J Neurooncol.* 2009 Apr;92(2):121-8.
111. Kilarski WW, Jura N, Gerwins P. Inactivation of Src family kinases inhibits angiogenesis in vivo: implications for a mechanism involving organization of the actin cytoskeleton. *Exp Cell Res.* 2003 Nov 15;291(1):70-82.
112. Janvier R, Sourla A, Koutsilieris M, Doillon CJ. Stromal fibroblasts are required for PC-3 human prostate cancer cells to produce capillary-like formation of endothelial cells in a three-dimensional co-culture system. *Anticancer Res.* 1997 May-Jun;17(3A):1551-7.
113. Walter-Yohrling J, Pratt BM, Ledbetter S, Teicher BA. Myofibroblasts enable invasion of endothelial cells into three-dimensional tumor cell clusters: a novel in vitro tumor model. *Cancer Chemother Pharmacol.* 2003 Oct;52(4):263-9.
114. Gorsch SM, Memoli VA, Stukel TA, Gold LI, Arrick BA. Immunohistochemical staining for transforming growth factor beta 1 associates with disease progression in human breast cancer. *Cancer Res.* 1992 Dec 15;52(24):6949-52.
115. Ronnov-Jessen L, Petersen OW. Induction of alpha-smooth muscle actin by transforming growth factor-beta 1 in quiescent human breast gland fibroblasts. Implications for myofibroblast generation in breast neoplasia. *Lab Invest.* 1993 Jun;68(6):696-707.
116. Vaughan MB, Howard EW, Tomasek JJ. Transforming growth factor-beta1 promotes the morphological and functional differentiation of the myofibroblast. *Exp Cell Res.* 2000 May 25;257(1):180-9.
117. Singer CF, Kronsteiner N, Marton E, Kubista M, Cullen KJ, Hirtenlehner K, et al. MMP-2 and MMP-9 expression in breast cancer-derived human fibroblasts is differentially regulated by stromal-epithelial interactions. *Breast Cancer Res Treat.* 2002 Mar;72(1):69-77.
118. Uria JA, Stahle-Backdahl M, Seiki M, Fueyo A, Lopez-Otin C. Regulation of collagenase-3 expression in human breast carcinomas is mediated by stromal-epithelial cell interactions. *Cancer Res.* 1997 Nov 1;57(21):4882-8.

119. Stefanini MO, Wu FT, Mac Gabhann F, Popel AS. The presence of VEGF receptors on the luminal surface of endothelial cells affects VEGF distribution and VEGF signaling. *PLoS computational biology*. [Research Support, N.I.H., Extramural]. 2009 Dec;5(12):e1000622.
120. Montesano R, Pepper MS, Orci L. Paracrine induction of angiogenesis in vitro by Swiss 3T3 fibroblasts. *J Cell Sci*. 1993 Aug;105 (Pt 4):1013-24.
121. Berndt A, Hyckel P, Konneker A, Katenkamp D, Kosmehl H. Oral squamous cell carcinoma invasion is associated with a laminin-5 matrix re-organization but independent of basement membrane and hemidesmosome formation. clues from an in vitro invasion model. *Invasion & metastasis*. [Research Support, Non-U.S. Gov't]. 1997;17(5):251-8.
122. Kim BG, An HJ, Kang S, Choi YP, Gao MQ, Park H, et al. Laminin-332-rich tumor microenvironment for tumor invasion in the interface zone of breast cancer. *The American journal of pathology*. [Research Support, Non-U.S. Gov't]. 2011 Jan;178(1):373-81.

Appendix A: Highly porous PLLA electrospun scaffolds for increased cell infiltration

A.1 Introduction

Although nanofibrous scaffolds such as bacterial cellulose and electrospun polycaprolactone (PCL)/collagen I structurally resemble the extracellular matrix, neither was capable of facilitating three-dimensional (3D) cell growth in our previous study [1]. A potential solution to this problem was to engineer cell-size pores between the electrospun fibers to enhance cell infiltration. Several techniques have been shown to successfully increase the porosity of electrospun scaffolds and subsequently augment cell infiltration. These methods include salt leaching [2], the removal of sacrificial fibers [3, 4], and increasing fiber diameter so that the spacing between the fibers act as natural cell-size pores [5]. While increasing fiber diameter was attempted and an increase in cell infiltration was observed (data not shown), the removal of sacrificial fibers was shown to be more effective at increasing 3D cell growth.

Poly(L-lactic Acid) (PLLA) was dual electrospun with polyethylene oxide (PEO), a synthetic polymer that dissolves in aqueous solution [4]. PLLA is a commonly used synthetic polymer in tissue engineering scaffolds because of its biocompatibility and biodegradability [6]. Electrospinning PLLA and PEO simultaneously on the same mandrel has been shown to form an inter-woven mesh of fibers from both polymers. A series of ethanol and DI water washes effectively removes the PEO fibers, leaving cell-size pores between the PLLA fibers [3]. Cell infiltration studies in the literature suggest that the highly porous PLLA electrospun scaffolds may be capable of facilitating sufficient 3D cell growth for encouraging regions of oxygen deficiencies, or hypoxia, to develop. In this short study, scanning electron microscopy was used to characterize scaffold fabrication, a nuclear stain was used to monitor cell infiltration, and gene expression analysis for hypoxia-inducible factor (HIF)-1 α was used to determine if the cells were experiencing hypoxic stress.

A.2 Materials and methods

A.2.1 Dual electrospun PLLA/PEO scaffolds

Poly(L-lactic acid) (Sigma Aldrich, St. Louis, MO, USA) was dissolved in a 3:1 mixture of dichloromethane and N,N-dimethylformamide at a total solution concentration of 12% (w/v). Using a syringe pump (KDS120, KD Scientific Inc., Holliston, MA, USA), the PLLA solution was delivered out of an 18 gauge blunt tip syringe needle at a constant rate of 5 ml/hr. The needle was kept at a distance of 20 cm from a spinning mandrel. Using a higher power voltage supply (Gamma High Voltage Research, Inc., Ormond Beach, FL, USA), a positive voltage of 16 kV was applied to the polymer solution and a negative voltage of 1 kV was applied to the spinning mandrel to attract the fibers. For fabricating the dual electrospun scaffolds, a second syringe pump was used to deliver a 10% (w/v) solution of PEO (Sigma Aldrich) dissolved in 90% ethanol (EtOH) (Fig. A.1). The PEO syringe pump was set up directly facing the PLLA syringe pump on the opposite side of the mandrel. An 18 gauge blunt tip needle was used to deliver the PEO solution at a distance of 17 cm from the spinning mandrel. The PEO solution was also connected to the higher power voltage supply at 16 kV. For dual electrospinning the mandrel was grounded. Following scaffold fabrication, the PEO fibers were leached from the dual electrospun scaffolds following separate 3 h washes in 95% EtOH and DI water.

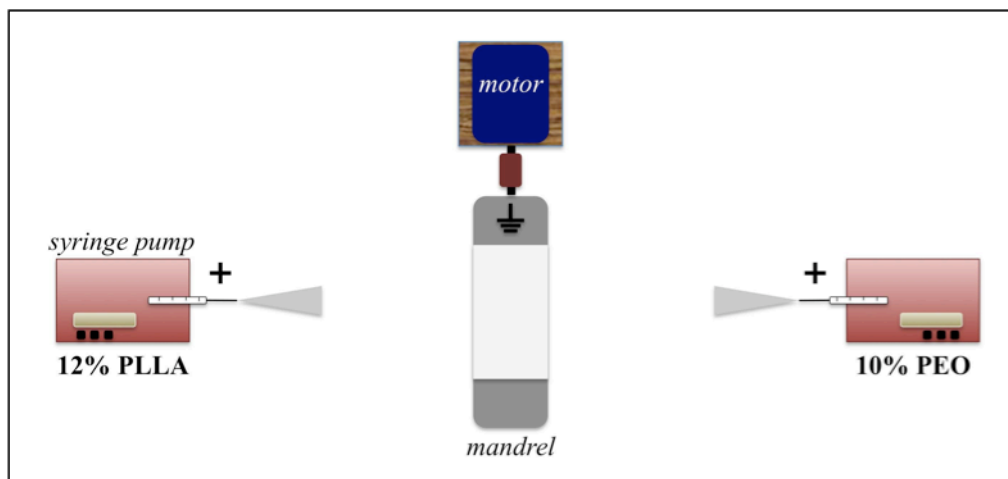


Figure A.1. Schematic drawing of the PLLA/PEO dual electrospinning set up.

A.2.2 Scanning electron microscopy

A FEI Quanta 600 FEG environmental scanning electron microscope (ESEM; FEI, Hillsboro, OR, USA) was used to characterize scaffold fabrication. Images were obtained under high vacuum at an accelerating voltage of 5 kV and a working distance of 9.6 – 9.8 mm.

A.2.3 Cell infiltration

The highly porous PLLA scaffolds were cut into 9 mm \odot circles and sterilized in 70% EtOH for 2 h followed by a series of PBS washes. The scaffolds were then placed in 48-well culture plates, pinned down with polymer tubing inserts, and allowed to soak in cell culture medium overnight prior to seeding. MDA-MB-231 human breast cancer cells (American Type Culture Collection, Manassas, VA, USA) were cultured in DMEM/F12 (1:1) +L-Glutamine, +15 mM HEPES (Invitrogen, Carlsbad, CA, USA), supplemented with 10% fetal bovine serum (Sigma Aldrich) and 1% Penicillin/Streptomycin (Invitrogen), and seeded at a density of 2.5×10^5 cells/scaffold. At set time points of 7, 14, and 21 days, the cell seeded scaffolds were embedded in Optimum Cutting Temperature Compound (Sakura Finetek, Torrance, CA, USA) at -20°C and sectioned using a MICROM HM 550 cryostat (Thermo Scientific, Kalamazoo, MI, USA) to obtain cross-sections. VECTASHIELD® mounting medium with DAPI (Vector Laboratories, Burlingame, CA, USA) was used to visualize nuclei with a Leica DMI 6000 fluorescent microscope (Leica Microsystems Inc., Buffalo Grove, IL, USA).

A.2.4 Gene expression analysis

HIF-1 α and VEGF-A gene expression were measured using quantitative reverse transcription polymerase chain reaction (qRT-PCR). MDA-MB-231 cells were seeded on 2.4 cm \odot circular scaffolds in 6-well culture plates at a density of 2×10^6 cells/scaffold. Total RNA was isolated on days 7, 14, and 21 using TRI Reagent® Solution (Applied Biosystems/Ambion, Austin, TX, USA). Next, 1 μg of total RNA was reverse-transcribed to cDNA using a Reverse Transcription System (Promega, Madison, WI, USA). Lastly, an ABI 7300 Sequence Detection System (Applied Biosystems, Carlsbad, CA, USA) was used to conduct qRT-PCR using TaqMan® Universal PCR Master Mix and gene-specific TaqMan® PCR primers (Applied Biosystems): HIF-1 α (NM_001530.3), VEGF-A (NM_001025366.2) and GAPDH (NM_002046.3). Gene expression was normalized to GAPDH using the comparative threshold cycle ($\Delta\Delta\text{Ct}$) method of quantification [7]. The data is presented as a relative fold induction, calculated as $2^{-\Delta\Delta\text{Ct}}$, with gene expression for cells cultured in 6-well culture plates used as the control. All experiments were performed as $n = 3$.

A.2.5 Statistical analysis

Relative fold induction measured using qRT-PCR was analyzed for significance using a Student's t-test. $p < 0.01$ was considered significant.

A.3 Results and discussion

Similar to what has been shown in the literature, removal of the PEO fibers from the dual electrospun scaffolds left large pores that were able to facilitate cell infiltration. Fig. A.2 shows SEM images of PLLA electrospun alone, PLLA dual electrospun with PEO, and the dual electrospun highly porous PLLA scaffolds following aqueous dissolution of the PEO fibers. There was a noticeable increase in pore size between the PLLA scaffolds before and after removal of the PEO fibers (Fig. A.2a and Fig. A.2c, respectively).

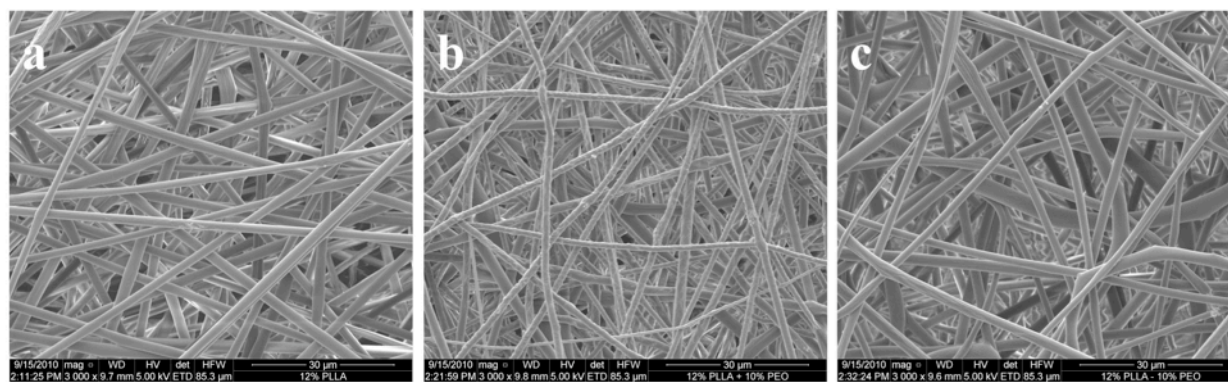


Figure A.2. a) 12% (w/v) PLLA was electrospun alone and b) dual electrospun with 10% (w/v) PEO. c) The PEO fibers were leached out through aqueous dissolution, leaving large voids for cell infiltration.

Over a 21-day period, cell infiltration into the highly porous PLLA scaffolds was shown to increase, monitored using a DAPI stain for nuclei. Maximum cell infiltration was observed at an average depth of 250 μm from the scaffold surface (Fig. A.3). However, cell density was still greatest at the surface rather than being evenly distributed throughout the scaffold. The lack of uniform cell density is discouraging for achieving 3D *in vitro* tumor growth as maintaining cells in culture for 21 days is challenging and a greater cell density (i.e. more time in culture) may be required to encourage hypoxia and subsequent upregulation of pro-angiogenic growth factors.

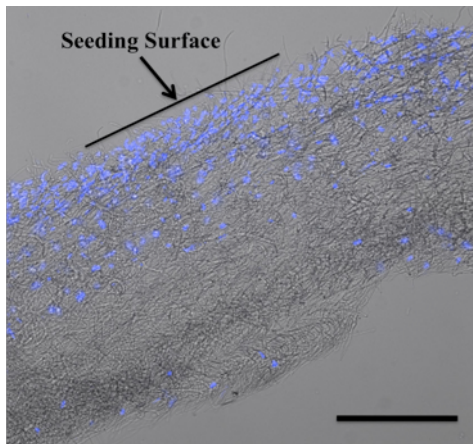


Figure A.3. Cross-section of a highly porous PLLA electrospun scaffold following 21 days of culture with the MDA-MB-231 cells. Considerable cell infiltration into the scaffold was observed, visualized with a DAPI stain for cell nuclei. Scale bar is 250 μm .

Quantitative RT-PCR was used to determine if the MDA-MB-231 cells cultured within the highly porous PLLA electrospun scaffolds experienced hypoxic stress. HIF-1 α was significantly downregulated ($p < 0.01$) at all time points over the 21-day period compared to MDA-MB-231 cells cultured as 2D monolayers on polystyrene 6-well culture plates (Fig. A.4). While the cause of the downregulation is unknown, it is clear that the cells cultured within the highly porous PLLA scaffolds were not experiencing hypoxic stress. In the absence of hypoxia, there was no upregulation of VEGF-A gene expression. This supports our previous concern that

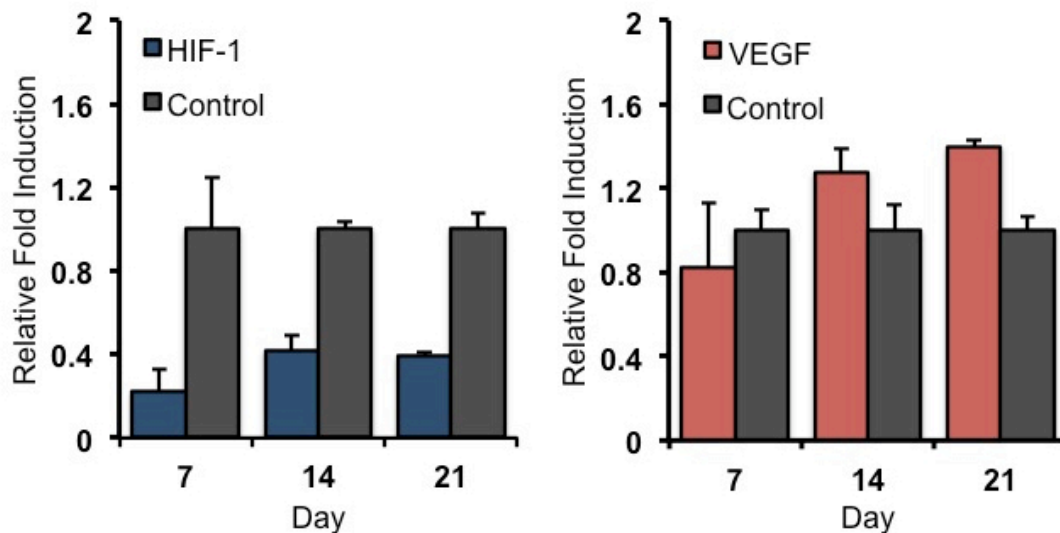


Figure A.4. Quantitative RT-PCR for determining intra-cellular levels of hypoxia and VEGF expression following cell infiltration within the highly porous PLLA electrospun scaffolds. Neither HIF-1 α nor VEGF-A were upregulated. * indicates significance ($p < 0.01$) compared to cells cultured in 2D monolayers.

the cell density within the scaffolds would not be sufficient to enforce limitations in oxygen and nutrient diffusion.

A.4 Conclusion

The highly porous PLLA electrospun scaffolds facilitated a considerably greater degree of cell infiltration compared to the composite PCL/collagen I electrospun scaffolds [1]. Aqueous dissolution of the PEO fibers left pores in the scaffold large enough to allow for noticeable cell infiltration over a 21-day period. However, these scaffolds were inadequate for encouraging 3D *in vitro* tumor growth. Gene expression analysis demonstrated that even after 21 days in culture, the MDA-MB-231 cells were not experiencing hypoxic stress or upregulating VEGF-A. Seeding efficiency and scaffold fabrication can be altered to help improve cell density, but the amount of time required to achieve the observed level of insufficient cell infiltration was substantial. An alternative scaffold type that promotes more efficient 3D cell growth will be considered in future studies.

A.5 Acknowledgements

I would like to thank Bryce Whited for teaching me how to fabricate the highly porous PLLA electrospun scaffolds.

A.6 References

1. Szot CS, Buchanan CF, Gatenholm P, Rylander MN, Freeman JW. Investigation of cancer cell behaviour on nanofibrous scaffolds. *Materials Science and Engineering C*. 2011;31(1):37-42.
2. Wright LD, Andric T, Freeman JW. Utilizing NaCl to increase the porosity of electrospun materials. *Materials Science and Engineering C*. 2011;31(1):30-36.
3. Whited BM, Whitney JR, Hofmann MC, Xu Y, Rylander MN. Pre-osteoblast infiltration and differentiation in highly porous apatite-coated PLLA electrospun scaffolds. *Biomaterials*. 2011 Mar;32(9):2294-304.
4. Baker BM, Gee AO, Metter RB, Nathan AS, Marklein RA, Burdick JA, et al. The potential to improve cell infiltration in composite fiber-aligned electrospun scaffolds by the selective removal of sacrificial fibers. *Biomaterials*. 2008 May;29(15):2348-58.

5. Ju YM, Choi JS, Atala A, Yoo JJ, Lee SJ. Bilayered scaffold for engineering cellularized blood vessels. *Biomaterials*. 2010 May;31(15):4313-21.
6. Yang F, Murugan R, Wang S, Ramakrishna S. Electrospinning of nano/micro scale poly(L-lactic acid) aligned fibers and their potential in neural tissue engineering. *Biomaterials*. 2005 May;26(15):2603-10.
7. Livak KJ, Schmittgen TD. Analysis of relative gene expression data using real-time quantitative PCR and the 2(-Delta Delta C(T)) Method. *Methods*. 2001 Dec;25(4):402-8.

A Three-Dimensional In Vitro Tumor Platform for Modeling Therapeutic Irreversible Electroporation

Christopher B. Arena,^{†Δ} Christopher S. Szot,^{†Δ} Paulo A. Garcia,[†] Marissa Nichole Rylander,[†] and Rafael V. Davalos^{†*}

[†]School of Biomedical Engineering and Sciences (SBES), Virginia Tech-Wake Forest University, Blacksburg, Virginia

ABSTRACT Irreversible electroporation (IRE) is emerging as a powerful tool for tumor ablation that utilizes pulsed electric fields to destabilize the plasma membrane of cancer cells past the point of recovery. The ablated region is dictated primarily by the electric field distribution in the tissue, which forms the basis of current treatment planning algorithms. To generate data for refinement of these algorithms, there is a need to develop a physiologically accurate and reproducible platform on which to study IRE in vitro. Here, IRE was performed on a 3D in vitro tumor model consisting of cancer cells cultured within dense collagen I hydrogels, which have been shown to acquire phenotypes and respond to therapeutic stimuli in a manner analogous to that observed in in vivo pathological systems. Electrical and thermal fluctuations were monitored during treatment, and this information was incorporated into a numerical model for predicting the electric field distribution in the tumors. When correlated with Live/Dead staining of the tumors, an electric field threshold for cell death (500 V/cm) comparable to values reported in vivo was generated. In addition, submillimeter resolution was observed at the boundary between the treated and untreated regions, which is characteristic of in vivo IRE. Overall, these results illustrate the advantages of using 3D cancer cell culture models to improve IRE-treatment planning and facilitate widespread clinical use of the technology.

INTRODUCTION

Irreversible electroporation (IRE) is a nonthermal, focal ablation technique that has shown tremendous promise as an effective cancer therapy (1–7). This procedure uses electrodes to apply a series of short-duration, high-intensity electric pulses through tissue. At the appropriate parameters, the pulses produce irreversible structural changes in the cell membranes within the targeted region, generating a predictable range of cell death with submillimeter resolution (8,9). IRE-based therapy is in the beginning phases of human clinical trials for prostate, kidney, liver, lung, and pancreatic cancer (4–7,10). Because the mechanism of cell death is linked to altered membrane permeability and not thermal processes, IRE spares important extracellular matrix components, such as major blood vessel and nerve architecture (11,12). This enables the treatment of tumors that are normally considered surgically inoperable, due to their close proximity to these sensitive structures (2,3). In addition, IRE is not subject to heat-sink effects from nearby blood flow, and IRE-induced lesions heal rapidly within 2 weeks after treatment (13). The lesion that develops during IRE is visible in real time on multiple imaging platforms (13–16), which is of great benefit to the surgeon, as there can be direct visual confirmation of treatment.

Developing accurate IRE-treatment planning models is essential for the technology to achieve widespread clinical use. Currently, the predictability of IRE outcomes relies

upon one's ability to predict the electric field distribution in the tissue and an a priori knowledge of the electric field threshold for cell death given a specific set of pulse parameters (duration, number, repetition rate). This is a complicated task. Altered membrane permeability leads to nonlinear changes in the dielectric tissue properties. In addition, although thermal damage is avoided by properly tuning the pulse parameters, there can still be significant Joule heating within the tissue that influences the dielectric response. Many studies have been performed to investigate the physiological response of various tissue types to IRE pulses without focusing on the engineering aspects of treatment planning (17–20). To the best of our knowledge, the electric field threshold for cell death has only been well documented in vivo for liver tissue (9,21,22), brain tissue (23), and an orthotopic model of mammary tumors in mice (24). Also, studies conducted to elucidate the dynamic relationship between IRE and changes in dielectric properties are limited to experiments on liver (25,26), skin (27), brain (28), kidney (29), and a subcutaneous model of fibrosarcoma in mice (30). Many types of tissue remain unexplored, including a variety of tumors. This can partially be attributed to the cost and difficulty associated with performing in vivo experiments.

A broader literature exists on in vitro cell suspensions (31–33). In this platform, the electric field threshold for cell death can be readily determined using commercially available indicators of membrane integrity or mitochondrial activity. However, there are significant limitations associated with using information derived from this model for treatment planning. Cells in suspension do not provide an accurate representation of their in vivo morphology, and

Submitted July 18, 2012, and accepted for publication September 14, 2012.

^ΔChristopher B. Arena and Christopher S. Szot contributed equally to this work.

*Correspondence: davalos@vt.edu

Editor: Sean Sun.

© 2012 by the Biophysical Society
0006-3495/12/11/2033/10 \$2.00

<http://dx.doi.org/10.1016/j.bpj.2012.09.017>

the cellular response obtained from these cultures is altered in the absence of cell-cell and cell-matrix interactions. In addition, cells in suspension lack the structural foundation necessary to provide useful spatial information after pulse delivery. To account for spatial information, researchers have proposed using vegetable tissue, such as potato. Potatoes are useful for economically determining field thresholds, because regions subject to IRE are markedly darker (34,35). Also, changes in potato dielectric properties during IRE have been shown to mimic those seen in vivo (34). However, although vegetables are useful for economically investigating trends, it is difficult to draw direct comparisons to tissue with the absence of physiologically responsive cancer cells.

There is a clear need for a system that can be used to model IRE-based cancer therapies and improve treatment planning in a more physiologically relevant manner without requiring the use of animal models. It has been well established in the fields of tissue engineering and cancer biology that cells cultured within a three-dimensional (3D) in vitro environment are capable of acquiring phenotypes and responding to stimuli in a manner analogous to that observed in in vivo biological systems (36–38). We hypothesize that engineering a platform for 3D tumor growth that mimics an in vivo tumor microenvironment will allow the cells to respond to IRE-based therapies in a manner that can be directly related to an in vivo response and therefore have direct clinical impact. Several groups have investigated the phenotypic response of culturing cancer cells in a 3D in vitro environment (39–41). Specifically, our group has developed 3D bioengineered tumors that exhibit phenotypic characteristics representative of in vivo cancer progression (40). This model involves culturing cancer cells within dense collagen I hydrogels, which facilitates proper cell-cell and cell-matrix interactions and encourages the development of a necrotic core, intracellular levels of hypoxia, and angiogenic potential. Therefore, these collagen I hydrogel-based bioengineered tumors can potentially be used for more accurate modeling of IRE-based cancer therapies in an in vitro setting.

In this study, a 3D cancer cell culture model is introduced for improving IRE-treatment planning. Changes in electrical conductivity and temperature were measured for a range of applied voltages. In addition, the role of cell concentration was explored in producing an electrically relevant model of tissue. After treatment, a Live/Dead assay was performed on intact constructs to demonstrate the relationship between the applied voltage and the extent of cell death. Select samples were fixed and processed for hematoxylin and eosin (H&E) staining. All data generated were incorporated into a numerical model. This allowed for the accurate determination of the electric field threshold for cell death (500 V/cm). These results were then compared to experiments using in vitro cell suspensions, which predicted a much higher threshold for cell death (1500 V/cm), illus-

trating the benefits of 3D cell culture models for IRE-treatment planning.

MATERIALS AND METHODS

Cell culture

Primary dispersed murine pancreatic cancer cells (provided by Dr. Dieter Saur, Technische Universität München, Munich, Germany) were established from pancreatic ductal adenocarcinomas (PDACs) of *Ptfl1a^{Cre/+}; LSL-Kras^{G12D/+}* mice on a C57Bl/6J genetic background. Specifically, primary pancreatic tumors (PPTs) were removed from a mouse (number 8182) and digested in 10 ml Dulbecco's modified Eagle's medium (DMEM) containing 150 U/ml collagenase Type 2 (Worthington, Lakewood, NJ) as described (42). Single PPT-8182 cell suspensions were cultivated in DMEM (supplemented with L-glutamine, ATCC, Manassas, VA) containing 10% fetal bovine serum (Sigma Aldrich, St. Louis, MO) and 1% penicillin/streptomycin (Invitrogen, Carlsbad, CA). These cells have been shown to replicate human pancreatic cancer in terms of histology, metastasis, and genetic alterations (42–44).

Collagen I hydrogel in vitro tumors

Collagen I hydrogel-based in vitro tumors were fabricated as described previously (40). Briefly, Sprague Dawley rat tail tendons were dissolved in 10 mM HCL under agitation overnight, the suspension was centrifuged at $22,500 \times g$ for 45 min, and the supernatant containing the collagen I was decanted. The concentration of the collagen I solution was calculated using dry-weight measurements, and the solution was sterilized by layering chloroform beneath the collagen I for 24 h. A neutralizing buffer containing $10 \times$ DMEM (Mediatech, Manassas, VA), 1N NaOH, and dH₂O was used to resuspend a pellet of PPT-8182 cells to obtain a final seeding density of 5×10^6 or 50×10^6 cells/ml. The cell suspension was then gently mixed on ice with an appropriate volume of collagen I to achieve a concentration of 8 mg/ml, which provides a matrix stiffness close to measured values for in vivo tumors (45), and pipetted into 10-mm-diameter cylindrical molds. After a 20-min polymerization period at 37°C, the cancer-cell-seeded hydrogels were removed from the molds and cultured in complete media overnight before IRE pulse delivery. It is important to note that the 5×10^6 cells/ml seeding density was used in a majority of the experiments, because this was found to adequately maintain cell viability throughout the construct over a 24-h period. The seeding density of 50×10^6 cells/ml was used to investigate whether a higher concentration of cells could modulate the electrical properties of the in vitro tumors. Control hydrogels were also fabricated using the neutralizing buffer alone without cells as a comparison to elucidate any effects due to electroporation.

IRE pulse delivery for in vitro tumors

In vitro tumors were temporarily removed from media and placed in six-well plates for IRE pulse delivery. Pulses were applied through custom electrodes (1.3 mm Ø) fabricated from stainless steel hollow dispensing needles (Howard Electronic Instruments, El Dorado, KS) using the ECM 830 electroporation system (BTX-Harvard Apparatus, Holliston, MA) (Fig. 1 a). The pulse duration (100 µs), number (80 pulses), and repetition rate (1 pulse/s) were held constant and chosen based on established protocols (8,46). In the 5×10^6 cells/ml seeded in vitro tumors, the applied voltage was varied (0 V, 150 V, 300 V, 450 V, and 600 V) to generate voltage/distance ratios of 0–1800 V/cm across the 3.35-mm electrode spacing (center to center). In the no-cells control and 50×10^6 cells/ml seeded in vitro tumors, the applied voltage was held constant at 300 V. Before the full IRE protocol, a prepulse was delivered at 30 V to determine the baseline electrical conductivity of the in vitro tumors. A port located 2.3 mm below the center point between the electrodes was included in

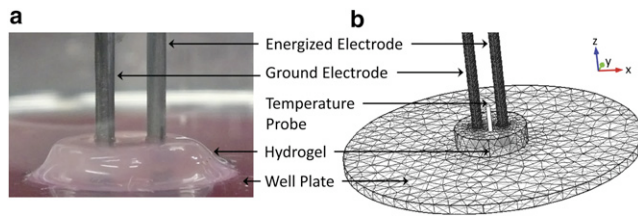


FIGURE 1 (a) Experimental setup for IRE pulse delivery in collagen I hydrogel-based in vitro tumors in which PDAC cells are embedded. (b) Geometry and mesh used in the finite element model for simulating the electrical and thermal response of the in vitro tumors to IRE.

the electrode design to monitor temperature in real time during treatment with a fiber optic probe (Luxtron m3300, LumaSense Technologies, Santa Clara, CA). In addition, current (TCP305 and TCPA300, Tektronix, Beaverton, OR) and voltage (P5200, Tektronix) were recorded noninvasively during treatment. The generated temperature, current, and voltage data were used to validate the numerical model for predicting the electric field threshold for IRE (see Results, Numerical model validation). Further, to eliminate the influence of the temperature probe on the electrical measurements, samples used for monitoring temperature were separate from those used for performing the viability analysis. After each treatment, the tumor diameter and thickness were measured with calipers for use in determining electrical properties. Each parameter combination was tested a minimum of three times ($n = 3$).

Viability analysis for in vitro tumors

After IRE pulse delivery, the in vitro tumors were incubated in complete media for 2 h before conducting a Live/Dead assay to allow any cells experiencing reversible electroporation to fully recover. Calcein acetomethoxy (AM) (4 μ M; $\lambda_{em} = 515$ nm; Invitrogen) was added to the media 30 min before analysis, and propidium iodide (1.5 mM; $\lambda_{em} = 617$ nm; Invitrogen) was added to the media 5 min before analysis. Calcein AM stains live cells, as it can be transported across the cell membrane and fluoresces when intracellular esterases remove the attached AM group. Propidium iodide (PI) fluorescently labels dead cells, as it only enters compromised cell membranes and binds to nucleic acids. A Leica DMI 6000 fluorescent microscope (Leica Microsystems, Buffalo Grove, IL) was used to tile a set of images and reconstruct the entire surface of the IRE-treated in vitro tumors. A Zeiss LSM 510 laser scanning confocal microscope (Carl Zeiss, Thornwood, NY) was used to analyze the live-dead cell interface and reconstruct a Z-stack. Viability imaging was performed on complete, nonsectioned in vitro tumors.

In addition, cytoskeletal disruption within the IRE-treated regions was investigated. The tumors were stained with rhodamine phalloidin (Invitrogen), a high-affinity probe for F-actin, and NucBlue fixed cell stain (Invitrogen) to visualize nuclei. The samples were then routinely fixed in 10% formalin, paraffin-embedded, and sectioned at 5 μ m for histological analysis. An H&E stain was performed to further analyze cell death within the IRE-treated regions.

Analysis of IRE on cell suspensions

The details of the methods associated with IRE pulse delivery and viability analysis for cell suspensions can be found in the [Supporting Material](#).

Numerical modeling

Description of the model geometry and mesh

Finite element analysis software (COMSOL Multiphysics 4.2a, Stockholm, Sweden) was used to solve for the electric field and temperature

distributions within the in vitro tumor during IRE therapy. A 3D geometry was constructed with dimensions equivalent to those in the experimental setup (Fig. 1 b). Each treatment was performed in a single well of a polystyrene six-well plate with a thickness of 1.2 mm and radius of 1.9 cm. The stainless steel electrodes had a length of 5.5 cm through which heat could dissipate. A finer mesh was used that consisted of 67,557 tetrahedral elements. This resulted in a <0.02% difference in temperature calculations at the site of the fiber optic probe upon successive refinements.

Determination of baseline electrical properties

To solve for the baseline electrical conductivity of the in vitro tumors, a three-variable parametric study was performed on the tumor radius (4.5, 4.75, and 5 mm), thickness (2, 2.5, and 3 mm), and conductivity (0.25, 0.5, 0.75, 1.0, 1.25 S/m) using the numerical model. Based on the pulse characteristics associated with IRE and the subdomain dielectric (Table 1) and geometry properties, propagation effects and transients were assumed to be negligible, and the quasistatic approximation was implemented (47,48). This allows for definition of the electric field magnitude as $E = -\nabla\phi$, where ϕ is the electric potential. Therefore, the spatial distribution of electric potential can be expressed as

$$0 = -\nabla \cdot (\sigma_0 E), \quad (1)$$

where σ_0 is the baseline electrical conductivity. Equation 1 was used to solve for the total current flowing in the in vitro tumor when a constant 30 V prepulse was applied to the energized electrode, with the other electrode set as ground. Specifically, the magnitude of the current density (J) was integrated over a cut plane dividing the geometry in half between the electrodes. All outer boundaries, excluding the electrodes, were assumed to be electrically insulating ($-n \cdot J = 0$), and the initial voltage (V_0) within each subdomain was 0 V.

The resulting data relating current (I) to each parameter combination were imported into Mathematica 8.0 (Wolfram, Champaign, IL). A regression analysis was performed to determine the baseline electrical conductivity using the measured current from the prepulse routine along with the corresponding tumor dimensions.

For comparison to the experimentally determined values for in vitro tumor baseline electrical conductivity, a theoretical calculation was performed using effective medium theory (EMT) (49). Specifically, Maxwell's equation for a dilute suspension was solved for the effective conductivity, σ :

$$\frac{\sigma_e - \sigma}{2\sigma_e + \sigma} = f \frac{\sigma_e - \sigma_p}{2\sigma_e + \sigma_p}, \quad (2)$$

where σ_e is the extracellular medium conductivity (1.2 S/m), σ_p is the homogeneous particle conductivity (0.2×10^{-4} S/m for an equivalent cell (49)), and f is the volume fraction of particles dispersed in the medium. Equation 2 is valid for predicting the low-frequency effective conductivity of a cell suspension for volume fractions up to 0.8 (50). This allowed for extrapolations of tumor baseline conductivity at cell concentrations higher than those tested experimentally to estimate what cell concentration would be required to be electrically similar to tissue.

TABLE 1 Physical properties used in numerical simulations

Parameter	Tumor	Electrode [†]	Plate [‡]
k (W m ⁻¹ K ⁻¹)	0.6	14	0.14
c (J kg ⁻¹ K ⁻¹)	4181.8	477	1300
ρ (kg m ⁻³)	997.8	7900	1050
σ_0 (S m ⁻¹)	1.2	2.22×10^6	1×10^{-16}

[†]Electrode numerical data are taken from Al Sakere et al. (46).

[‡]Plate numerical data are taken from Chiu and Fair (67).

Determination of transient current and temperature development

The temperature distribution (T) within the in vitro tumor was obtained by transiently solving a modified heat conduction equation with inclusion of the Joule heating-source term ($J \cdot E = \sigma|E|^2$):

$$\rho c \frac{\partial T}{\partial t} = \nabla \cdot (k \nabla T) + \frac{\tau (\sigma |E|^2)}{P}, \quad (3)$$

where τ is the pulse duration, P is the period of the pulses, k is the thermal conductivity, c is the specific heat at constant pressure, and ρ is the density (Table 1). Due to the fact that the collagen-I-hydrogel-based tumors have a water content of >98%, the thermal properties of the tumor were chosen to be the same as those of water. The tumor baseline electrical conductivity (1.2 S/m) was determined experimentally from the average of the no-cells and 5×10^6 -cells/ml trials (Table 2), as there was no statistical difference between those two groups (see Results, Determination of baseline electrical properties). In addition, the tumor radius (4.705 mm) and thickness (2.45 mm) were also selected by averaging the measurements from the same groups. Equation 1 was modified to include a temperature dependence on electrical conductivity:

$$0 = -\nabla \cdot (\sigma(T)E), \quad (4)$$

where

$$\sigma(T) = \sigma_0(1 + \alpha(T - T_0)) \quad (5)$$

and α is the coefficient that describes how the conductivity varies with temperature. This parameter was estimated to be 2%/°C by optimizing the measured change in temperature and current throughout treatment to match the theoretical changes. The optimization was performed by running a parametric study on α at 0.5%/K increments. A value of 2%/°C is similar to values observed in biological tissue (51).

At each time step, the conductivity and electric field are determined and updated in the Joule heating term. As opposed to simulating individual pulses, a duty cycle approach was employed to calculate the temperature increase resulting from various IRE protocols. A constant voltage (150, 300, 450, and 600 V) was applied to the energized electrode, with the other electrode set as ground. The Joule heating term was scaled by the duty cycle ($\tau/P = 100 \times 10^{-6}$) to ensure that equal amounts of energy were deposited into the tissue by the onset of each pulse. This approach has been validated in our previous work (29,52) as providing an accurate prediction of the temperature distribution with a fraction of the computational requirements necessary to resolve microsecond-order pulses within a treatment lasting several seconds.

All outer boundaries, excluding the outer vertical edge of the well plate, were treated as convective cooling ($-n \cdot (-k \nabla T) = h(T_{ext} - T)$) with an exterior temperature of 22°C and a heat-transfer coefficient of 25 ($\text{W m}^{-2} \text{K}^{-1}$). The vertical edge of the well plate was treated as thermally insulating ($-n \cdot (-k \nabla T) = 0$), and the initial temperature (T_0) within each subdomain was the same as the exterior temperature. Intermediate time stepping was used to ensure that at least one time step was taken each second.

TABLE 2 Baseline electrical conductivity from prepulse measurements and EMT theory

Concentration (cells ml ⁻¹)	Experimental σ_0 (S m ⁻¹)	Theoretical σ_0 (S m ⁻¹)
0 ($n = 6$)	1.18 ± 0.09	1.2
5×10^6 ($n = 15$)	1.24 ± 0.11	1.2
50×10^6 ($n = 6$)	1.08 ± 0.08	1.1

Determination of electric field threshold for cell death

After the in vitro tumor viability analysis, the area, height, and width of the treated region were measured using Image J (National Institutes of Health, Bethesda MD) for three samples of each parameter combination and averaged. All measurements were made on the surface of the tumors. The width measurements were taken in the x -direction and the height measurements were taken in the y -direction. The electric-field threshold for cell death was determined in three ways, using the area, height, and width measurements (Table 3). For determining the threshold from the area measurement, the electric field on the top surface of the tumors was integrated at the end of the treatment ($t = 80$ s) for values greater than the threshold value. The threshold value was varied until the area calculation best matched the measured values within 1 V/cm (excluding the area of the electrodes). For determining the threshold from the height and width measurements, the value of the electric field at a point on the surface corresponding to the measurements was taken at the end of treatment.

RESULTS

Physiological response to IRE pulse delivery within in vitro tumors

When the 30 V prepulse was delivered to determine the baseline electrical conductivity of the in vitro tumors, no cell death was observed as a result of the treatment (Fig. 2 a). At this low voltage/distance ratio (90 V/cm taken from the center-to-center electrode spacing), any electroporation that may have occurred was reversible (21). Minimal cell death was observed where the electrodes punctured the surface of the tumors. When the electric field strength was increased to 150 V, cell death was observed on the medial side of both electrodes, but the treated regions did not expand far enough to completely connect (Fig. 2 b). Rather, a transition zone of both live and dead cells was observed at the center of the two electrodes. At the higher electric-field strengths (300 V and 450 V), the treated region was amplified with increasing electric-field strength, expanding in both the x - and y -directions (Fig. 2, c and d). The nonspecific regions of cell death present around the periphery of the tumors were a result of handling the samples with tweezers.

A sharp interface between live and dead cells was observed at the threshold boundary for cell death with submillimeter resolution (Fig. 3 a). The specificity of these treatments was similar to what has been achieved during in vivo IRE pulse delivery (8,9). Confocal microscopy was used to show that the IRE-induced cell death was uniform in the z -direction (Fig. 3 b), demonstrating that the in vitro tumors can provide spatial information in both the xy and z planes. In addition, the 3D reconstruction highlighted the transition zone at the live/dead cell interface where there were clear contrasting gradients of live and dead cells that converged at the threshold boundary for cell death.

Histology was used to further assess the IRE-induced cell death in the in vitro tumors. Again, a sharp interface between live and dead cells was evident from an H&E stain (Fig. 4 a). The PPT-8182 cells within the untreated regions

TABLE 3 Treatment dimensions and electric field threshold for cell death

Voltage (V)	Conc. (cells ml ⁻¹)	Area (mm ²)	Height (mm)	Width (mm)	E_T (Area, Height, and Width) (V cm ⁻¹)
300 ($n = 3$)	5×10^6	16.28 ± 2.73	4.02 ± 0.40	4.91 ± 0.34	491, 501, 500
450 ($n = 3$)	5×10^6	25.80 ± 1.48	5.83 ± 0.40	5.58 ± 0.13	498, 502, 470

Conc., concentration.

appeared normal with healthy nuclei and complete cytoplasm, signifying that they were not affected by the IRE pulse delivery (Fig. 4 *c*). Conversely, the cells within the IRE-treated regions were completely destroyed except for their remaining nuclei, which appeared abnormal and no longer contained nucleoli (Fig. 4 *b*). The absence of cytoplasmic material indicated that the IRE pulses had irreversibly compromised the cell membranes, leaving clear voids in the collagen hydrogel where the cells had been.

An F-actin stain was performed to determine the effect of the IRE pulses on the actin cytoskeleton of PPT-8182 cells cultured within the in vitro tumors (Fig. 4, *d* and *e*). PPT-8182 cells within the untreated regions had spherical morphologies with high concentrations of actin present around the periphery of the cells (Fig. 4 *e*). Since the tumors were only cultured overnight before IRE pulse delivery, the cells did not proliferate into large clusters or develop invasive processes, as observed previously (40). The cytoskeleton of cells within the IRE-treated regions seems to be permanently disrupted, appearing speckled and faded (Fig. 4 *d*). This suggests that the IRE pulses led to degrada-

tion of the actin filaments, which differs from reversible electroporation, where actin filaments have been shown to reassemble 1 h after electroporation (53). The presence of a disrupted cytoskeleton within the IRE-treated cells revealed that some cytoplasmic material was still present after IRE pulse delivery. Over time, this remaining cytoplasm was either fully degraded or washed away during histology preparation (Fig. 4 *b*). In treatment groups where the Live/Dead stain was not performed until 24 h after IRE treatment, there were no visible PI-stained dead cells within the treated regions, indicating that the nuclei had also been fully degraded or washed away (data not shown).

Determination of baseline electrical properties

The baseline electrical conductivity of the in vitro tumors is given in Table 2. A one-way ANOVA was used to investigate the effect of cell concentration on the rank of baseline conductivity. In the event of a significant main effect, pairwise comparisons were completed using Tukey's honestly significant difference (HSD). All statistical analysis were conducted using JMP 9 (SAS Institute, Cary, NC) with a significance level of $p \leq 0.05$. Results indicate that a cell concentration of 50×10^6 cells/ml is high enough to produce a detectable decrease of ~ 0.1 S/m in baseline conductivity when compared to the 5×10^6 cells/ml group. Further, there is no significant difference in baseline conductivity between the no-cells and 5×10^6 cells/ml groups. These

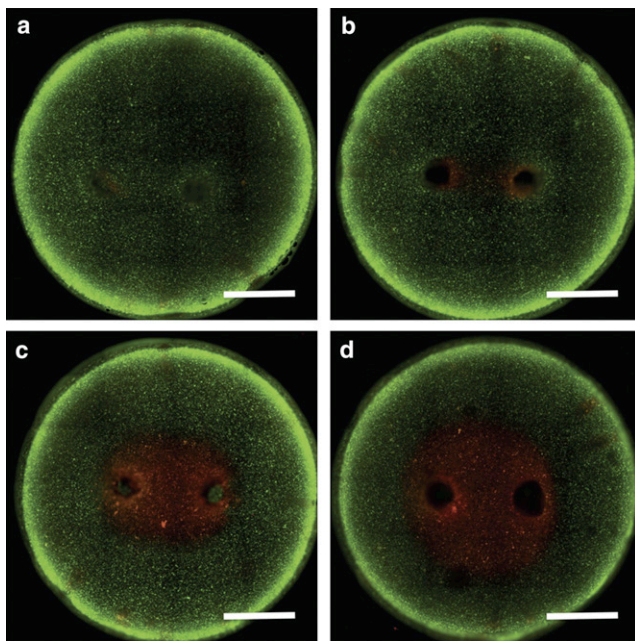


FIGURE 2 A live/dead assay for assessment of cell death after IRE pulse delivery of 30 V (*a*), 150 V (*b*), 300 V (*c*), and 450 V (*d*). Live cells were stained green using Calcein AM and dead cells were stained red using propidium iodide. Images were tiled to reconstruct the entire surface of the IRE-treated in vitro tumors. The bright rings encircling the hydrogels are a consequence of out-of-plane fluorescence at the rounded edges. Scale bars, 2.5 mm.

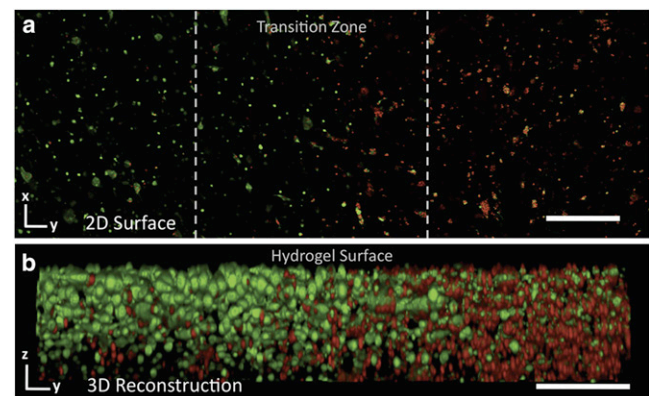


FIGURE 3 (*a*) A sharp interface between live (green; left) and dead (red; right) cells at the threshold boundary for cell death with submillimeter resolution. (*b*) 3D reconstruction at this interface highlights the transition zone between live and dead cells and demonstrates that IRE-induced cell death was uniform throughout the in vitro tumors. The dotted lines in (*a*) define the representative region from which the image in (*b*) was taken. Scale bars, 400 μ m (*a*) and 200 μ m (*b*).

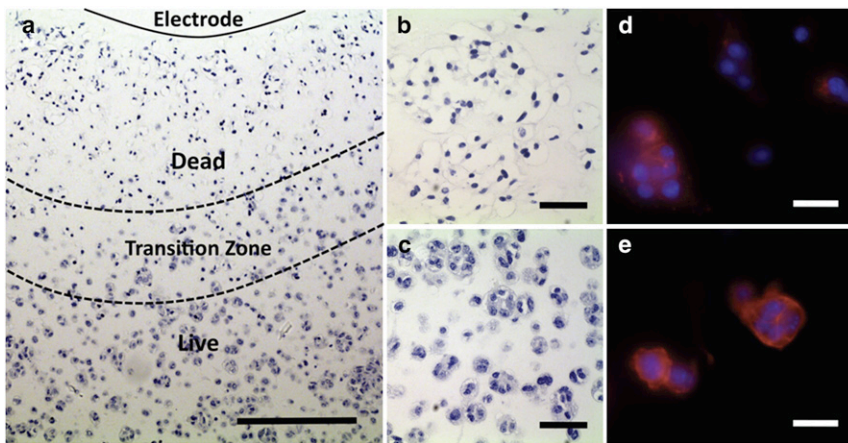


FIGURE 4 (a) An H&E stain for further assessment of cell viability after IRE pulse delivery of 450 V through in vitro tumors seeded with 50×10^6 cells/ml. (b and c) Cells located within the IRE-treated regions appeared to be devoid of most cytoplasmic material (b), whereas cells located within the untreated regions appeared normal, with intact cell membranes (c). (d and e) Dotted lines in (a) define the transition zone at the live/dead cell interface. An F-actin stain (red) was used to determine the effect of IRE-pulse delivery on the cytoskeleton of PPT-8182 cells cultured within the IRE-treated (d) and untreated (e) regions of the in vitro tumors. The actin cytoskeleton within the IRE-treated cells appears permanently disrupted. Nuclei were stained with DAPI (blue). Scale bars, 250 μm (a), 50 μm (b and c), and 25 μm (d and e).

results agree well with the theoretical calculations based on EMT. Specifically, a cell concentration on the order of 48×10^6 cells/ml is required to reduce the baseline conductivity by 0.1 S/m. This corresponds to a volume fraction of cells of ~ 0.06 .

Numerical model validation

The numerical model was validated through comparisons to experimentally measured changes in current and temperature between the first and last pulse of treatment (Fig. 5). The predicted change in current delivered through the in vitro tumors was accurate around 1 standard deviation at all voltages tested (Fig. 5 a). As the applied voltage increased, the change in current during treatment also increased. This change is nonlinear due to the inclusion of a temperature-dependent conductivity. The predicted change in temperature at the location of the fiber optic temperature probe was accurate within a single standard deviation at all voltages tested (Fig. 5 b). The temperature change during treatment also increased nonlinearly with the applied voltage. The inclusion of the actual metal electrodes and polystyrene plate was required to dissipate the heat and match experimental temperatures using a reasonable heat-transfer coefficient for free convection with air of $25 \text{ W m}^{-2} \text{ K}^{-1}$ (54).

Determination of transient current and temperature development

Representative surface plots of the predicted electric field, temperature, and electrical conductivity distributions for an applied voltage of 300 V are shown in Fig. 6. The maximum temperature at the end of treatment occurred at the center of the domain. For all simulated voltages, the maximum temperature was calculated to be 23°C , 27°C , 35°C , and 51°C for applied voltages of 150 V, 300 V, 450 V, and 600 V, respectively, with the baseline set at 22°C . Experimentally, an applied voltage of 600 V resulted in

the formation of a void at the center of the in vitro tumors, presumably due to collagen denaturation (data not shown) (55). By comparing the dimensions of the void with the temperature distribution, it was conservatively estimated that temperatures $>45^\circ\text{C}$ should be avoided in future experiments on this in vitro platform.

Due to the inclusion of a temperature-dependent electrical conductivity, the maximum conductivity at the end of treatment also occurred at the center of the domain. For all simulated voltages, the maximum conductivity was calculated to be 1.2 S/m, 1.3 S/m, 1.5 S/m, and 1.9 S/m for applied voltages of 150 V, 300 V, 450 V, and 600 V, respectively, with the baseline set at 1.2 S/m. Even at the highest voltages, the noticeable increase in conductivity had an insignificant effect on the electric-field distribution in the current experimental setup. For example, between

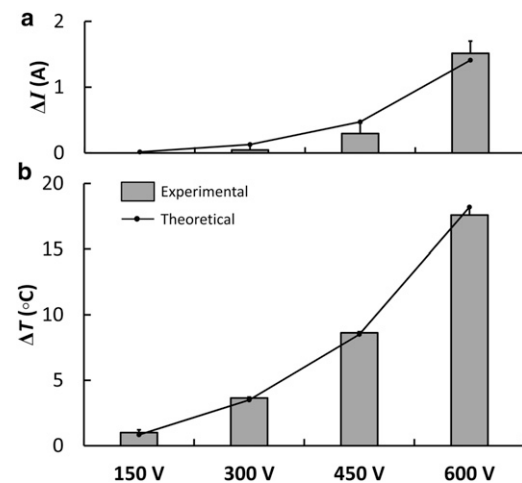


FIGURE 5 Change in current (a) and temperature (b) delivered through the in vitro tumors during IRE performed at 150 V, 300 V, 450 V, and 600 V. The treatment consisted of 80 100- μs -long pulses delivered at a rate of 1/s. The bars with 1 standard deviation indicate the experimentally measured values. The data points along the line illustrate the results of the numerical model, which was optimized to match the measured changes in current and temperature from onset to offset of pulsing.

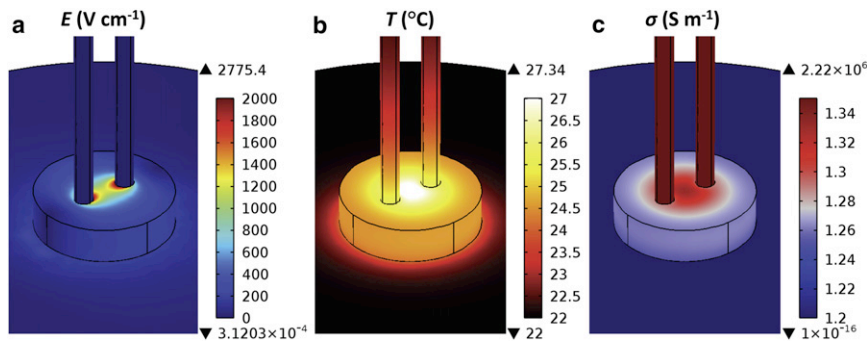


FIGURE 6 Surface plots from the numerical model showing the electric-field distribution (a), temperature distribution (b), and conductivity distribution (c) at the end of an 80-s IRE treatment at 300 V. The upper and lower triangles along the scale bars indicate maximum and minimum values, respectively, present within the entire domain. In the case of (c) these values are consistent with those reported in Table 1 for the electrode and plate domains. Regions experiencing values outside the given color range (e.g., electrode and plate conductivity) assume the color associated with the limits of the displayed data.

the onset and offset of pulsing, the area of the top surface of the in vitro tumors exposed to an electric field >500 V/cm changed by 0.01 mm², 0.02 mm², 0.09 mm², and 0.4 mm² for applied voltages of 150 V, 300 V, 450 V, and 600 V, respectively. This correlates with a slight change in the dimensions of the 500 V/cm electric-field contour from the onset to offset of pulsing. However, even at 600 V, the height of the area encompassed by the contour (y-direction) changed by only 0.08 mm, and the width (x-direction) changed by only 0.04 mm. All of these variations are within 1 standard deviation of experimentally measured values (Table 3).

Determination of electric-field threshold for cell death of in vitro tumors

Only applied voltages of 300 V and 450 V were used to determine the electric-field threshold for cell death (Table 3). As mentioned, an applied voltage of 150 V did not produce a complete lesion extending past the lateral surfaces of the electrodes or completely connecting in the center (Fig. 2), which eliminated the possibility of accurate width measurements. At 600 V, void formation at the center of the in vitro tumors, presumably due to collagen denaturation, also eliminated the possibility of accurate measure-

ments. There was a close agreement in the electric-field threshold for cell death as determined by both the 300 V and 450 V treatment groups. In the 300 V group, averaging the electric-field threshold as determined by each separate measurement resulted in a threshold of 497 V/cm. In a similar way, in the 450 V group, the average threshold from each measurement was 490 V/cm. Between the groups, the highest variability was present within thresholds determined from width measurements. This is likely due to the difficulty in measuring lesion width near the electrodes and the steep gradient in electric potential near the lateral electrode surfaces. When width measurements were omitted from the analysis, the electric-field threshold for cell death became 496 V/cm and 500 V/cm for the 300 V and 450 V groups, respectively.

Overlaying the 500 V/cm contour on the live/dead stained images of the in vitro tumors from each of these groups illustrates the accuracy of the numerical model for determining the electric-field threshold for cell death (Fig. 7). Although no data are present in the literature on the threshold in pancreatic tumors, our result is comparable to that obtained in vivo for brain tissue (23) when a similar pulsing protocol was implemented. Results citing a higher threshold of 637 V/cm in vivo for liver tissue were likely due to a 10-fold reduction in the number of pulses delivered (21), and this effect could be elucidated in future experiments.

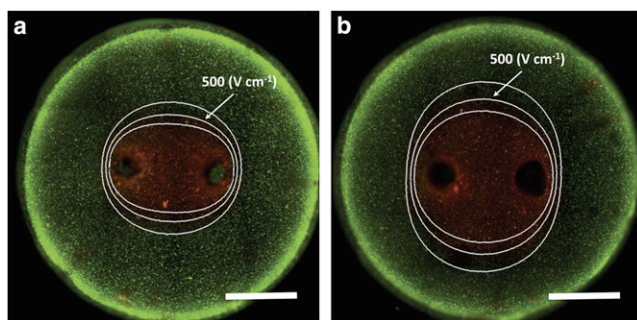


FIGURE 7 Overlay of electric-field contours predicted by the numerical model at the end of 80-s IRE treatments at 300 V (a) and 450 V (b) with the corresponding live/dead tiled images from Fig. 2. The field contours shown are at 400 V/cm (inner), 500 V/cm (middle), and 600 V/cm (outer). The contour labeled 500 V/cm denotes the threshold for cell death. Scale bars, 2.5 mm.

Determination of electric-field threshold for cell death in suspension

It is difficult to determine a distinct electric-field threshold for cell death from the viability analysis on cell suspensions. In the past, conservative estimates have been made under the assumption that the threshold in vivo corresponds to the value of the electric field, resulting in $<5\%$ viability in suspension (31). Under the same logic, our results suggest that a conservative estimate of the electric-field threshold for cell death in vivo would be ~ 1500 V/cm (see Fig. S1). In addition, at 500 V/cm there was no corresponding reduction of cell viability in suspension. Similar results have been shown for the onset of reversible electroporation,

which was found to occur at a significantly lower electric-field strength *in vivo* compared to the same cells in suspension (56).

DISCUSSION

Cancer cells cultured in 3D collagen I hydrogels were shown to respond to IRE pulse delivery comparable to published *in vivo* results. This included a similar electric-field threshold for cell death (Table 3) (23), sparing of the underlying collagen network (8), and submillimeter resolution at the boundary between treated and untreated regions (Fig. 3) (8,9). Recently, collagen I hydrogels have been used to study reversible electroporation and electrogene transfer (57). In that study, conducted by Haberl and Pavlin, it was found that electrogene transfer had a dependency on plasmid concentration and pulse duration similar to that seen *in vivo* when performed in a 3D *in vitro* environment. Further, transfection was more pronounced on the surface of the collagen I hydrogels, due to diffusion limitations through the collagen mesh, which is also a characteristic seen *in vivo* (58). Outside the field of electroporation, 3D cell culture models have been shown to elicit an *in-vivo*-like response for other cancer therapies, including chemotherapy (59), radiation therapy (60), and nanoparticle delivery (61). This platform could also be used to optimize therapies that utilize low-intensity alternating electric fields to arrest cell proliferation by disrupting cells during cleavage (62), as opposed to directly inducing cell death through membrane disruption, as shown here.

Compared to conventional *in vitro* IRE-treatment-planning models, such as cell suspensions and cell-culture monolayers, the 3D *in vitro* tumor model generated more accurate predictability of IRE outcomes. This is likely due to the ability of the cells cultured in 3D to reproduce the cell-cell/cell-matrix interactions seen in the original tissue that are important for dictating an *in-vivo*-like morphology. As a result of cell protrusions interacting with the collagen matrix, the cell diameters in the hydrogel are larger than they are in suspension (13.1 μm). This may contribute to the decreased electric-field threshold for cell death, as a larger diameter increases the calculated transmembrane potential (63):

$$\Delta\varphi(\theta) = \frac{3}{2}E a \cos(\theta), \quad (6)$$

where a is the radius of the cell and θ is the polar angle measured from the center of the cell with respect to the direction of the electric field. The induced transmembrane potential creates a suprphysiologic electric field in the membrane that is thought to be responsible for permeabilization. For a membrane thickness of 5 nm, an external electric field of 500 V/cm applied across a cell in suspension ($\Delta\varphi_{\text{max}} = 0.98$ V) generates a voltage/distance ratio on

the order of ~ 2 MV/cm within the membrane. In cell monolayers, 2D spatial information and limited cell-cell/cell-matrix interactions can be obtained, but the path taken by electrical current is significantly altered when compared to a 3D environment (a majority of current flows through the culture media over the top of cells that are adhered to a highly insulative surface), which may alter the transmembrane potential and electric-field threshold for cell death. Furthermore, analysis of dead cells is complicated by the fact that they can detach from the culture surface.

Current measurements were unable to detect any dynamic change in bulk electrical conductivity due to electroporation for *in vitro* tumors consisting of 5×10^6 cells/ml. Specifically, at an applied voltage of 300 V, there was no statistical difference in the change in current between the first and last pulse when comparing the 5×10^6 -cells/ml group to the no-cells control group. Therefore, any dynamic changes in bulk-tissue electrical conductivity due to electroporation that have been reported *in vivo* (64) could be neglected from the numerical model of the *in vitro* tumor. This greatly reduced the number of parameters contributing to an accurate determination of the electric-field threshold for IRE.

When the cell concentration was increased to 50×10^6 cells/ml, there was a significant decrease in the measured current during treatment at 300 V compared to the no-cells control and 5×10^6 -cells/ml groups (data not shown). This is unlike what happens *in vivo*, and it may be the result of the fact that the cytoplasm has a lower electrical conductivity than the extracellular space (65). Upon electroporation, the release of cytosol into the extracellular space may dominate the bulk electrical properties at this specific cell concentration. At higher cell concentrations in tissue, the bulk electrical properties during electroporation are dominated by the creation of membrane defects, which greatly increase the conductivity and resulting current during treatment. According to the EMT model, a cell concentration on the order of 340×10^6 cells/ml would be required to cut the baseline conductivity of the *in vitro* tumors in half, from 1.2 S/m to 0.6 S/m, which is more electrically relevant to tissue and corresponds to a volume fraction of 0.4. Due to diffusion limitations through the collagen hydrogel, obtaining such high concentrations while maintaining cell viability is a challenging task. This will be the subject of future work directed toward replicating the dynamic conductivity changes seen *in vivo* on a 3D *in vitro* platform.

A current limitation of the relatively high electrical conductivity of the *in vitro* tumors compared to an *in vivo* environment is the added heat generated during treatment. As a result, select protocols that do not cause significant thermal damage *in vivo* may be unsuitable for testing *in vitro* due to collagen I denaturation. Similar concerns are present when treating cells in suspension. For the range of applicable pulse parameters tested here, thermal changes had a minimal influence on the electric field distribution. This may be attributed to the small size of the *in vitro* tumor

domain relative to the electrode spacing, which causes the entire tumor to experience both an elevated temperature and conductivity. In the future, the hydrogel volume could be increased to mimic a clinical scenario in which the electrodes are inserted into a targeted tumor and the treatment region varies in all directions. Here, the experimental setup was designed to induce a region of cell death that was symmetric in the z -direction (Fig. 3).

CONCLUSION

Performing IRE on a 3D in vitro tumor platform produced an electric field dependence on cell death characteristic of an in vivo response. Thus, this model is suitable for generating a wide range of data that will be useful in refining treatment-planning algorithms used in clinical IRE procedures. Specifically, studies correlating varying pulse parameters to ablation volume in a variety of cancer cell lines will help identify both protocol-specific and cell-specific parameters to enhance the reliability of predicted outcomes. In addition, there is the possibility of growing patient-specific in vitro tumors from biopsied tissue. Further development of this platform will facilitate the acceptance of IRE as a viable cancer therapy.

SUPPORTING MATERIAL

One figure, supporting references, and a detailed description of IRE pulse delivery and viability analysis for cell suspensions are available at [http://www.biophysj.org/biophysj/supplemental/S0006-3495\(12\)01032-6](http://www.biophysj.org/biophysj/supplemental/S0006-3495(12)01032-6).

The authors thank Dr. Dieter Saur of the Technische Universität München for generously providing access to the murine PDAC cells.

This work was supported by the National Science Foundation under Awards CAREER CBET-1055913 and CAREER CBET-0955072.

REFERENCES

- Davalos, R. V., I. L. Mir, and B. Rubinsky. 2005. Tissue ablation with irreversible electroporation. *Ann. Biomed. Eng.* 33:223–231.
- Garcia, P. A., T. Pancotto, ..., R. V. Davalos. 2011. Non-thermal irreversible electroporation (N-TIRE) and adjuvant fractionated radiotherapeutic multimodal therapy for intracranial malignant glioma in a canine patient. *Technol. Cancer Res. Treat.* 10:73–83.
- Neal, 2nd, R. E., J. H. Rossmeisl, Jr., ..., R. V. Davalos. 2011. Successful treatment of a large soft tissue sarcoma with irreversible electroporation. *J. Clin. Oncol.* 29:e372–e377.
- Thomson, K. R., W. Cheung, ..., A. Haydon. 2011. Investigation of the safety of irreversible electroporation in humans. *J. Vasc. Interv. Radiol.* 22:611–621.
- Bagla, S., and D. Papadouris. 2012. Percutaneous irreversible electroporation of surgically unresectable pancreatic cancer: a case report. *J. Vasc. Interv. Radiol.* 23:142–145.
- Ball, C., K. R. Thomson, and H. Kavnoudias. 2010. Irreversible electroporation: a new challenge in “out of operating theater” anesthesia. *Anesth. Analg.* 110:1305–1309.
- Kingham, T. P., A. M. Karkar, ..., Y. Fong. 2012. Ablation of perivascular hepatic malignant tumors with irreversible electroporation. *J. Am. Coll. Surg.* 215:379–387.
- Onik, G., P. Mikus, and B. Rubinsky. 2007. Irreversible electroporation: implications for prostate ablation. *Technol. Cancer Res. Treat.* 6:295–300.
- Edd, J. F., L. Horowitz, ..., B. Rubinsky. 2006. In vivo results of a new focal tissue ablation technique: irreversible electroporation. *IEEE Trans. Biomed. Eng.* 53:1409–1415.
- Onik, G., and B. Rubinsky. 2010. Irreversible electroporation: first patient experience focal therapy of prostate cancer. In *Irreversible Electroporation*. B. Rubinsky, editor. Springer, Berlin/Heidelberg. 235–247.
- Maor, E., A. Ivorra, and B. Rubinsky. 2009. Non thermal irreversible electroporation: novel technology for vascular smooth muscle cells ablation. *PLoS ONE.* 4:e4757.
- Li, W., Q. Y. Fan, ..., Z. Li. 2011. The effects of irreversible electroporation (IRE) on nerves. *PLoS ONE.* 6:e18831.
- Rubinsky, B., G. Onik, and P. Mikus. 2007. Irreversible electroporation: a new ablation modality—clinical implications. *Technol. Cancer Res. Treat.* 6:37–48.
- Zhang, Y., Y. Guo, ..., A. C. Larson. 2010. MR imaging to assess immediate response to irreversible electroporation for targeted ablation of liver tissues: preclinical feasibility studies in a rodent model. *Radiology.* 256:424–432.
- Lee, E. W., C. Chen, ..., S. T. Kee. 2010. Advanced hepatic ablation technique for creating complete cell death: irreversible electroporation. *Radiology.* 255:426–433.
- Deodhar, A., S. Monette, ..., S. B. Solomon. 2011. Percutaneous irreversible electroporation lung ablation: preliminary results in a porcine model. *Cardiovasc. Intervent. Radiol.* 34:1278–1287.
- Appelbaum, L., E. Ben-David, ..., S. N. Goldberg. 2012. US findings after irreversible electroporation ablation: radiologic-pathologic correlation. *Radiology.* 262:117–125.
- Ben-David, E., L. Appelbaum, ..., S. N. Goldberg. 2012. Characterization of irreversible electroporation ablation in in vivo porcine liver. *AJR Am. J. Roentgenol.* 198:W62–W68.
- Bower, M., L. Sherwood, ..., R. Martin. 2011. Irreversible electroporation of the pancreas: definitive local therapy without systemic effects. *J. Surg. Oncol.* 104:22–28.
- Charpentier, K. P., F. Wolf, ..., D. E. Dupuy. 2010. Irreversible electroporation of the pancreas in swine: a pilot study. *HPB (Oxford).* 12:348–351.
- Miklavcic, D., D. Semrov, ..., L. M. Mir. 2000. A validated model of in vivo electric field distribution in tissues for electrochemotherapy and for DNA electrotransfer for gene therapy. *Biochim. Biophys. Acta.* 1523:73–83.
- Sano, M. B., R. E. Neal, ..., R. V. Davalos. 2010. Towards the creation of decellularized organ constructs using irreversible electroporation and active mechanical perfusion. *Biomed. Eng. Online.* 9:83.
- Garcia, P. A., J. H. Rossmeisl, Jr., ..., R. V. Davalos. 2010. Intracranial nonthermal irreversible electroporation: in vivo analysis. *J. Membr. Biol.* 236:127–136.
- Neal, 2nd, R. E., R. Singh, ..., R. V. Davalos. 2010. Treatment of breast cancer through the application of irreversible electroporation using a novel minimally invasive single needle electrode. *Breast Cancer Res. Treat.* 123:295–301.
- Miklavcic, D., D. Sel, ..., L. Mir. 2004. Sequential finite element model of tissue electropermeabilisation. *Conf. Proc. IEEE Eng. Med. Biol. Soc.* 5:3551–3554.
- Ivorra, A., and B. Rubinsky. 2007. In vivo electrical impedance measurements during and after electroporation of rat liver. *Bioelectrochemistry.* 70:287–295.
- Pavselj, N., Z. Bregar, ..., D. Miklavcic. 2005. The course of tissue permeabilization studied on a mathematical model of a subcutaneous tumor in small animals. *IEEE Trans. Biomed. Eng.* 52:1373–1381.
- Garcia, P. A., J. H. Rossmeisl, Jr., ..., R. V. Davalos. 2011. A parametric study delineating irreversible electroporation from thermal damage based on a minimally invasive intracranial procedure. *Biomed. Eng. Online.* 10:34.

29. Neal, 2nd, R. E., P. A. Garcia, ..., R. V. Davalos. 2012. Experimental characterization and numerical modeling of tissue electrical conductivity during pulsed electric fields for irreversible electroporation treatment planning. *IEEE Trans. Biomed. Eng.* 59:1076–1085.
30. Ivorra, A., B. Al-Sakere, ..., L. M. Mir. 2009. In vivo electrical conductivity measurements during and after tumor electroporation: conductivity changes reflect the treatment outcome. *Phys. Med. Biol.* 54:5949–5963.
31. Neal, 2nd, R. E., and R. V. Davalos. 2009. The feasibility of irreversible electroporation for the treatment of breast cancer and other heterogeneous systems. *Ann. Biomed. Eng.* 37:2615–2625.
32. Miller, L., J. Leor, and B. Rubinsky. 2005. Cancer cells ablation with irreversible electroporation. *Technol. Cancer Res. Treat.* 4:699–705.
33. Shafiee, H., P. A. Garcia, and R. V. Davalos. 2009. A preliminary study to delineate irreversible electroporation from thermal damage using the Arrhenius equation. *J. Biomech. Eng.* 131:074509.
34. Ivorra, A., L. M. Mir, and B. Rubinsky. 2010. Electric field redistribution due to conductivity changes during tissue electroporation: experiments with a simple vegetal model. *IFMBE Proc.* 25:59–62.
35. Hjouj, M., and B. Rubinsky. 2010. Magnetic resonance imaging characteristics of nonthermal irreversible electroporation in vegetable tissue. *J. Membr. Biol.* 236:137–146.
36. Yamada, K. M., and E. Cukierman. 2007. Modeling tissue morphogenesis and cancer in 3D. *Cell.* 130:601–610.
37. Kim, J. B. 2005. Three-dimensional tissue culture models in cancer biology. *Semin. Cancer Biol.* 15:365–377.
38. Griffith, L. G., and M. A. Swartz. 2006. Capturing complex 3D tissue physiology in vitro. *Nat. Rev. Mol. Cell Biol.* 7:211–224.
39. Fischbach, C., R. Chen, ..., D. J. Mooney. 2007. Engineering tumors with 3D scaffolds. *Nat. Methods.* 4:855–860.
40. Szot, C. S., C. F. Buchanan, ..., M. N. Rylander. 2011. 3D in vitro bioengineered tumors based on collagen I hydrogels. *Biomaterials.* 32:7905–7912.
41. Verbridge, S. S., N. W. Choi, ..., C. Fischbach. 2010. Oxygen-controlled three-dimensional cultures to analyze tumor angiogenesis. *Tissue Eng. Part A.* 16:2133–2141.
42. von Burstin, J., S. Eser, ..., D. Saur. 2009. E-cadherin regulates metastasis of pancreatic cancer in vivo and is suppressed by a SNAIL/HDAC1/HDAC2 repressor complex. *Gastroenterology.* 137:361–371, e1–e5.
43. Seidler, B., A. Schmidt, ..., D. Saur. 2008. A Cre-loxP-based mouse model for conditional somatic gene expression and knockdown in vivo by using avian retroviral vectors. *Proc. Natl. Acad. Sci. USA.* 105:10137–10142.
44. Saur, D., B. Seidler, ..., R. M. Schmid. 2005. CXCR4 expression increases liver and lung metastasis in a mouse model of pancreatic cancer. *Gastroenterology.* 129:1237–1250.
45. Paszek, M. J., N. Zahir, ..., V. M. Weaver. 2005. Tensional homeostasis and the malignant phenotype. *Cancer Cell.* 8:241–254.
46. Al-Sakere, B., F. André, ..., L. M. Mir. 2007. Tumor ablation with irreversible electroporation. *PLoS ONE.* 2:e1135.
47. Pavselj, N., and D. Miklavcic. 2011. Resistive heating and electropermeabilization of skin tissue during in vivo electroporation: a coupled nonlinear finite element model. *Int. J. Heat Mass Transf.* 54:2294–2302.
48. Edd, J. F., and R. V. Davalos. 2007. Mathematical modeling of irreversible electroporation for treatment planning. *Technol. Cancer Res. Treat.* 6:275–286.
49. Pavlin, M., T. Slivnik, and D. Miklavcic. 2002. Effective conductivity of cell suspensions. *IEEE Trans. Biomed. Eng.* 49:77–80.
50. Polk, C., and E. Postow. 1996. Handbook of Biological Effects of Electromagnetic Fields. CRC Press, Boca Raton, FL.
51. Schwan, H. P., and K. R. Foster. 1980. Rf-field interactions with biological systems: electrical properties and biophysical mechanisms. *Proc. IEEE.* 68:104–113.
52. Arena, C. B., M. B. Sano, ..., R. V. Davalos. 2011. High-frequency irreversible electroporation (H-FIRE) for non-thermal ablation without muscle contraction. *Biomed. Eng. Online.* 10:102.
53. Kanthou, C., S. Kranjc, ..., M. Cemazar. 2006. The endothelial cytoskeleton as a target of electroporation-based therapies. *Mol. Cancer Ther.* 5:3145–3152.
54. Chapman, A. J. 1987. Fundamentals of Heat Transfer. Macmillan, London.
55. Bozec, L., and M. Odlyha. 2011. Thermal denaturation studies of collagen by microthermal analysis and atomic force microscopy. *Biophys. J.* 101:228–236.
56. Belehradek, Jr., J., S. Orlowski, ..., L. M. Mir. 1994. Electropermeabilization of cells in tissues assessed by the qualitative and quantitative electroloading of bleomycin. *Biochim. Biophys. Acta.* 1190:155–163.
57. Haberl, S., and M. Pavlin. 2010. Use of collagen gel as a three-dimensional in vitro model to study electropermeabilization and gene electrotransfer. *J. Membr. Biol.* 236:87–95.
58. Henshaw, J. W., and F. Yuan. 2008. Field distribution and DNA transport in solid tumors during electric field-mediated gene delivery. *J. Pharm. Sci.* 97:691–711.
59. dit Faute, M. A., L. Laurent, ..., H. Bobichon. 2002. Distinctive alterations of invasiveness, drug resistance and cell-cell organization in 3D-cultures of MCF-7, a human breast cancer cell line, and its multidrug resistant variant. *Clin. Exp. Metastasis.* 19:161–168.
60. St Croix, B., V. A. Flørenes, ..., R. S. Kerbel. 1996. Impact of the cyclin-dependent kinase inhibitor p27Kip1 on resistance of tumor cells to anticancer agents. *Nat. Med.* 2:1204–1210.
61. Lee, J., G. D. Lilly, ..., N. A. Kotov. 2009. In vitro toxicity testing of nanoparticles in 3D cell culture. *Small.* 5:1213–1221.
62. Kirson, E. D., V. Dbalý, ..., Y. Palti. 2007. Alternating electric fields arrest cell proliferation in animal tumor models and human brain tumors. *Proc. Natl. Acad. Sci. USA.* 104:10152–10157.
63. Schwan, H. P. 1957. Electrical properties of tissue and cell suspensions. *Adv. Biol. Med. Phys.* 5:147–209.
64. Davalos, R. V., D. M. Otten, ..., B. Rubinsky. 2004. Electrical impedance tomography for imaging tissue electroporation. *IEEE Trans. Biomed. Eng.* 51:761–767.
65. Mezeme, M. E., G. Pucihar, ..., D. Miklavcic. 2012. A numerical analysis of multicellular environment for modeling tissue electroporation. *Appl. Phys. Lett.* 100:143701–143705.
66. Reference deleted in proof.
67. Chiu, J., and P. G. Fair. 1979. Determination of thermal conductivity by differential scanning calorimetry. *Thermochim. Acta.* 34:267–273.

Supporting Materials

IRE Pulse Delivery and Viability Analysis for Cell Suspensions

PPT-8182 cells were suspended at a concentration of 5×10^6 cells/ml in electroporation buffer, which was created by mixing (3:1) complete culture media with dielectrophoresis buffer (8.5% sucrose, 0.3% glucose, and 0.725% basal media). This mixture was selected to obtain a solution with an electrical conductivity of 1 S/m, as determined by a conductivity meter (B-173, Horiba, Kyoto, Japan). A conductivity of 1 S/m resembled the baseline conductivity of the collagen I hydrogels and allowed for the delivery of electric fields up to 1500 V/cm without arcing or significant bubble formation due to electrolysis. A micro-osmometer (3MO Plus, Advanced Instruments Inc., Norwood, MA, USA) was used to confirm that the osmolality of the buffer (315 mOsm/kg) was near the value for complete culture media (320 mOsm/kg) and well within the physiological range (300 to 340 mOsm) (1).

For each treatment, 250 μ l of cell suspension was pipetted into an electroporation chamber (HT-P96-4, BTX-Harvard Apparatus, Holliston, MA, USA) with parallel plate electrodes. IRE pulses were applied as described above with a fixed pulse duration (100 μ s), number (80 pulses), and repetition rate (1 pulse/sec). The applied voltage was varied (0 V, 200 V, 400 V, 500 V, and 600 V) to generate electric fields ranging from 0 to 1500 V/cm across the 4 mm electrode gap (edge-to-edge). Each parameter combination was repeated five times ($n = 5$).

Following IRE pulse delivery, samples were removed from the electroporation chambers, pipetted into 1.5 ml microcentrifuge tubes, and kept on ice for 1 h to allow adequate time for the cells to recover from any reversible electroporation effects (2). A dye exclusion assay was performed by mixing samples 1:1 with a 0.4% Trypan Blue solution (T8154, Sigma-Aldrich, St. Louis, MO, USA). Samples were then pipetted into an Ultra-plane Neubauer's hemocytometer (Hausser Scientific, Horsham, PA, USA) and placed under an inverted light microscope (Olympus CKX41, Center Valley, PA, USA). Live and dead cell counts were obtained assuming that live cells exclude Trypan Blue and dead cells absorb it, providing a clear indicator of cell death. Percent viability was based on the ratio of the number of blue cells to the total number of cells and normalized to the 0 V sham group.

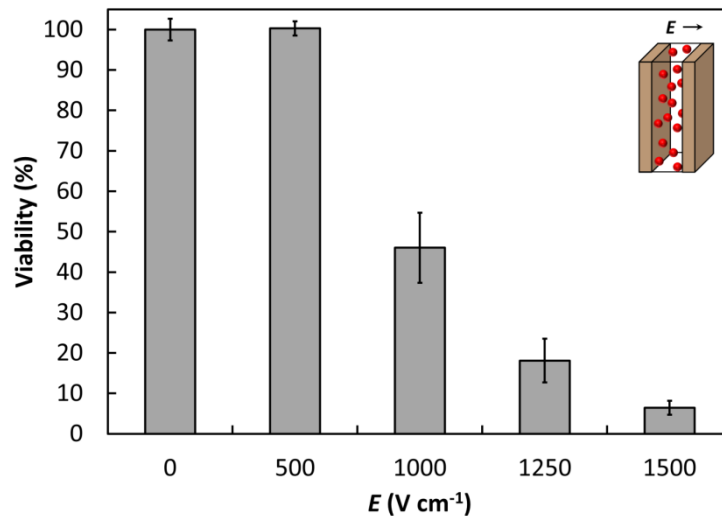


FIGURE S1 Percent viability (normalized to the sham group) following IRE of PPT-8182 cells in suspension at electric fields ranging from 0 V/cm to 1500 V/cm. At the field threshold for cell death determined from the *in vitro* tumors (500 V/cm), there was no significant reduction in cell viability determined from suspension experiments performed in cuvettes. The raw percent viability for the sham group was 95 %.

Supporting References

1. Puttaswamy, S. V., S. Sivashankar, R. J. Chen, C. K. Chin, H. Y. Chang, and C. H. Liu. 2010. Enhanced cell viability and cell adhesion using low conductivity medium for negative dielectrophoretic cell patterning. *Biotechnol J* 5:1005-1015.
2. Kanduser, M., M. Sentjerc, and D. Miklavcic. 2006. Cell membrane fluidity related to electroporation and resealing. *European biophysics journal* : EBJ 35:196-204.